E.O. Paton Electric Welding Institute of the National Academy of Science of Ukraine
International Association «Welding»

The Paton Welding Journal

10
2023

International Scientific-Technical and Production Journal ◊ Founded in January 2000 (12 Issues Per Year)

Address of Editorial Board
E.O. Paton Electric Welding Institute, 11 Kazymyr Malevych Str., 03150, Kyiv, Ukraine
Tel./Fax: (38044) 205 23 90, E-mail: journal@paton.kiev.ua, patonpublishinghouse@gmail.com
https://patonpublishinghouse.com/eng/journals/tpwj

State Registration Certificate 24933-14873 ПР from 13.08.2021
ISSN 0957-798X, DOI: http://dx.doi.org/10.37434/tpwj

Subscriptions, 12 issues per year:
$384 — annual subscription for the printed (hard copy) version, air postage and packaging included;
$312 — annual subscription for the electronic version (sending issues in pdf format or providing access to IP addresses).

Representative Office of «The Paton Welding Journal» in China:
China-Ukraine Institute of Welding, Guangdong Academy of Sciences
Address: Room 210, No. 363 Changxing Road, Tianhe, Guangzhou, 510650, China.
Zhang Yupeng, Tel: +86-20-61086791, E-mail: patonjournal@gwi.gd.cn

The content of the Journal includes articles received from authors from around the world in the field of welding, cutting, cladding, soldering, brazing, coating, 3D additive technologies, electrometallurgy, material science, NDT and selectively includes translations into English of articles from the following journals, published in Ukrainian:
- Automatic Welding (https://patonpublishinghouse.com/eng/journals/as);
- Electrometallurgy Today (https://patonpublishinghouse.com/eng/journals/sem);
- Technical Diagnostics & Nondestructive Testing (https://patonpublishinghouse.com/eng/journals/tdnk).

CONTENTS

ORIGINAL ARTICLES

*Translated Article(s) from “Automatic Welding”, No. 10, 2023.

**Translated Article(s) from “Electrometallurgy Today”, No. 3, 2023.

***Translated Article(s) from “Technical Diagnostics & Nondestructive Testing”, No. 3, 2023.

DOI: https://doi.org/10.37434/tpwj2023.10.01

STRUCTURE AND PROPERTIES OF WELDED JOINTS OF 13KhGMRB STEEL IN PULSED-ARC WELDING

O.A. Gaivoronskyi, V.D. Poznyakov, S.L. Zhdanov, A.V. Zavdoveyev, A.O. Maksymenko, A.M. Denysenko

E.O. Paton Electric Welding Institute of the NASU
11 Kazymyr Malevych Str., 03150, Kyiv, Ukraine

ABSTRACT

The results of studies on the structure formation in the welds and heat-affected-zone (HAZ) metal of low-alloy heat-strengthened 13KhGMRB steel in a pulsed-arc welding, changes in mechanical properties and stress intensity factor in brittle fracture and resistance to cold and fatigue cracks formation are given. It was found that compared to stationary arc welding, in a pulsed-arc welding in the structure of welds and HAZ metal of joints, a larger number of hardening structures of bainite and martensite is formed. It was determined that regardless of the welding method, the values of strength ($\sigma_{0.2}$ and σ_t) and ductility (δ_5 and ψ) of metals are approximately at the same level while their ability to resist impact loads, especially at a test temperature –40 °C, in the case of pulsed-arc welding grows. In particular, it was determined that the values of impact toughness of the HAZ metal of welded joints produced using pulsed-arc welding are by 30 % higher compared to arc welding and amount to 108 J/cm^2. I.e., the cold resistance of the weld metal is clearly increased. The resistance of weld and HAZ metals to brittle fracture is at a fairly high level ($Kq \geq 84$ MPa$\sqrt{m}$). It was also established that due to an increase in hardening structures in the HAZ metal of the welded joints produced using pulsed welding, the temperature of preliminary heating should be increased from 90 to 120 °C to avoid the cold cracks formation. Instead, such welded joints have a higher resistance to fatigue cracks formation at cyclic bending load.

KEYWORDS: low-alloy heat-strengthened steel, pulsed-arc welding, weld metal, HAZ, structure, mechanical properties, cold cracks, brittle fracture, fatigue resistance

INTRODUCTION

In the manufacture of critical metal structures in various industries, such as civil construction, mechanical engineering, bridge building, etc., low-alloy heat-strengthened C690 steels with $\sigma_{0.2}$ = = 580–750 MPa are increasingly used. This allows a significant increase in the load on construction facilities and extends their service life. The safe operation of such structures is largely determined by the quality of welded joints production, which should meet the requirements of equal strength, cold resistance and have a sufficiently high resistance to brittle and fatigue fracture. It should also be noted that difficulties in welding low-alloy high-strength steels with $\sigma_{0.2}$ = = 580–750 MPa are associated with the need in preventing the probability of cold cracks formation in the weld and HAZ metals, determined by the formation of hardening structures [1, 2]. The solution of these problems is complicated by the condition that welded joints should have the required values of service and technological properties after welding without additional heat treatment. This is especially important when welding heat-strengthened steels, the structure and properties of whose welded joints are significantly influenced by heating and cooling parameters typical for arc welding. A typical representative of this steel grades is a low-alloy heat-strengthened 13KhGMRB steel. Namely regarding the joints of this steel, which was welded using traditional arc processes, the technical literature provides a sufficient information on the influence of technological modes of welding on the structure, mechanical properties and ability of welded joints to resist the cold cracks formation.

It should be noted that recently, in the world practice, in the manufacture of welded structures, pulsed-arc welding processes are increasingly used. Pulsed-arc welding (PAW) is characterized by a periodically changed arc power [3, 4–8], which allows solving the complex technological problems in the manufacture of unique structures and improving the efficiency of welding processes. PAW provides expanded abilities to control the processes of melting and electrode metal transfer, stirring of molten metal, and also it becomes possible to regulate the properties and sizes of the weld and HAZ metal of welded joints. This improves the formation of joints when producing them in different spatial positions while providing smooth transitions from the weld to base metal [9–16]. At the same time, in the technical literature there is no sufficient information on the influence of the features of pulsed-arc welding process on the structure formation, mechanical properties of welded joints from high-strength steels prone to hardening and their ability to resist the cold cracks formation.

In view of this, the aim of the work was to obtain the comparative test results in determination of the effect of welding method, namely PAW, on the structure of welds and HAZ metals of welded joints of low-alloy heat-strengthened 13KhGMRB steel, change of mechanical properties, on the resistance of joints to cold and fatigue cracks formation, that has a certain scientific and practical importance.

RESEARCH PROCEDURE

The aim of research was welded joints of high-strength low-alloy 13hGMRB steel of the following chemical composition, %: 0.13 C; 0.31 Si; 1.71 Mn; 0.96 Cr; 0.45 Mo; 0.03 Ni; 0.046 Nb; 0.002 B, 0.01 S and 0.015 P, which were produced in mechanized welding using a stationary arc (base option), in welding on a pulsating mode by modulated current (for comparison) and in PAW (process under study).

As the power source, inverter rectifier EWM Phoenix Pulse 500 was used, which provides a different frequency of pulses in pulsed-arc welding. Mechanized welding in a mixture of shielding gases (82 % Ar + 18 % CO_2) of joints of 13KhGMRB steel of 20 mm thickness with a V-shaped edge preparation was performed using a solid cross-section wire Sv-10KhN2GSMFTYu with a diameter of 1.2 mm. Welding using a conventional process with a stationary arc was performed on such mode: I_w = 180–200 A, U_a = 26 V, V_w = 15–18 m/h. Welding mode by pulsating arc: pulse current I_A = 220 A, pause current I_B = 80 % from I_A, U_a = 26–27 V, duty cycle 0.5, frequency 1.33 Hz. In PAW, the mode was the following: I_{av} = 220–240 A, U_a = 26–28 V, V_w = 14–21 m/h (pulsed current I_{max} = 450 A, pause current I_{min} = 120–165 A, duty cycle 0.33–0.36, frequency 120–150 Hz) [17, 18].

Metallographic examinations were performed using a light microscope Neophot-32 and a scanning electron microscope Mira 3 LMU (Tescan). In the examination, the detector of secondary electrons (SE designation on the electron image) and the detector of back-scattered electrons (BSE designation) were used. The microhardness of individual structural components and the integral hardness of the metal were measured in the durometer M-400 of the LECO Company at a load of 100 g (*HV*). The specimens for metallographic examinations were prepared by standard procedures with the use of diamond pastes of different dispersion, the microstructure was revealed by chemical etching in a 4% alcohol nitric acid solution.

To test the mechanical properties of the weld and HAZ metals of welded joints, standard specimens were manufactured for the tests on static tension and impact bending (specimens respectively of type II and IX of GOST 6996–96)*. According to the results of the carried out tests, the influence of the welding method on the change in the values of strength (σ_y and σ_t), ductility (δ_5 and ψ) and impact toughness (*KCV*) were evaluated.

The ability of the metal to resist brittle fracture was determined using the fracture mechanics approaches, according to which the specimens of 10 mm thickness with an indicated fatigue crack at the apex of the notch were used, preliminary cut from the welded joints. Then, at a static bending load, the critical stress intensity factor *Kq* was determined. To determine the values of the critical stress intensity factor, the procedure was used according to [13]. At the same time, the dependence established earlier was taken into account, that when *Kq* values grow, the sensitivity to the stress concentration decreases and the resistance of the metal to brittle fracture rises, or vice versa, with a decrease in the factor, the resistance decreases.

The resistance to cold cracks formation was evaluated with the help of a butt technological Tekken specimen. As a test criterion, the preheating temperature was taken, in which cracks in the weld or HAZ metal of welded joints were not formed.

The fatigue tests were performed on the specimens of T-welded joints of 12 mm thickness at their cyclic bending load. The welded joints were loaded at 14 Hz frequency at symmetric cycle stresses with a level of 30, 35 and 35 MPa. The UMP-1 machine was used for the tests. During the tests, a number of cycles, at which the formation of a fatigue crack of a critical length (3 mm) and a stress, at which the specimen remained undamaged after $2.1 \cdot 10^6$ load cycles were registered.

RESULTS OF WORK AND THEIR DISCUSSION

According to the results of studying mechanical properties, it was determined that the values of static strength of welded joints, produced with the use of the abovementioned arc welding processes are almost comparable (Figure 1, *a*). Namely, the yield strength of welds metal of the welded joints is in the range of $\sigma_{0.2}$ = 713–740 MPa. The lower values are typical of the stationary process, and the higher values are inherent in PAW. The same tendency is observed for the values of ultimate rupture strength of the welds metal — σ_t = 786–800 MPa. For the abovementioned welding methods, the values of ductility (Figure 1, *b*) also does not differ significantly. Thus, the values of relative elongation of the welds metal of the welded joints are within δ_5 = 16–19 %, and those of reduction in area are ψ = 59–67 %. Unlike the values of strength and ductility, the effect of welding process on the value of impact toughness of both the welds and

HAZ metal of welded joints is more significant and ambiguous (Figure 2).

As for the values of impact toughness of the welds metal, at the test temperature of 20 °C, the highest values of KCV_{+20} = 133 J/cm^2 are typical for the stationary process. In welding using pulsating arc and in PAW, they are reduced relatively to 117 and 96 J/cm^2. The same tendency to reduce *KCV* values of the weld metal is maintained in the case of testing specimens at –20 °C. In this case, the values of impact toughness of the welds metal of welded joints made accordingly by an arc that burns stationary, using pulsating arc and using PAW are 79, 69 and 62 J/cm^2. Instead, in the case when the specimens were tested at a temperature of minus 40 °C, significant differences between *KCV* values of the welds metal of studied welded joints are not observed. They are almost identical and are in the range of 43–49 J/cm^2. It should be noted that despite the reduction in impact toughness typical of pulsed welding processes, they remain at a high level and meet the requirements of standard documents for impact toughness of 13KhGMRB steel ($KCV_{40} \geq 39$ J/cm^2).

Some other regularities for changing impact toughness are peculiar to the HAZ metal of welded joints (Figure 2). The same as in the study of the specimens with a notch over the weld metal, the highest values at a test temperature of 20 °C, which are equal to 150 J/cm^2, are typical of a stationary welding process. For the pulsating arc and for PAW these values are 97 and 113 J/cm^2. At a test temperature of –20 °C, the tendency of reduction in the values of cold resistance begins to change. The difference between *KCV* values is significantly reduced and they are respectively 113, 94 and 108 J/cm^2. At the test temperature of –40 °C, the difference between the values of impact toughness of the HAZ metal of welded joints made using a stationary welding process and welding using pulsating arc almost was not observed. These welding processes are characterized by the values of impact toughness in the range from 73 to 79 J/cm^2. They are much higher and, moreover, those at the level of values of impact toughness of the specimens that were tested at a temperature of –20 °C (KCV_{-40} = 108 J/cm^2), characteristic of the HAZ metal of the welded joints made using PAW. I.e., the cold resistance of the HAZ metal of the joints made using PAW clearly increases.

Concerning the results of studying the specimens, the test of which was performed using the force criterion of fracture mechanics, no significant differences in the values of *Kq* were detected. In all cases, the resistance of the welds and HAZ metals of welded joints to the brittle fracture is at a high level (Figure 3). It was determined that the metal of welds of

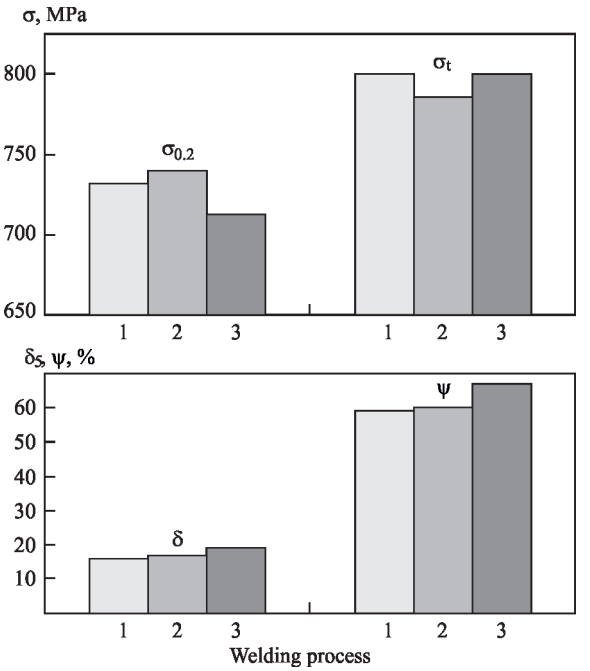

Figure 1. Mechanical properties of welds metal of welded joints of 13KhGMRB steel: *1* — pulsating arc; *2* — PAW; *3* — stationary arc

the welded joints of 13KhGMRB steel, made both by PAW as well as welding with a pulsating arc in the studied temperature range has approximately the same values of *Kq*. At a test temperature of 20 °C, it amounts to 94.6–95.6, at –20 °C –88–89.1, and at –40 °C 84.7–85.8 MPa√m (Figure 3, *a*, *c*). Also, a significantly high resistance to brittle fracture belongs to the HAZ metal, namely the stress intensity factor, depending on the test temperature changes in the range of 84.2–92.7 MPa√m. It should also be noted that compared to welding using stationary arc, the values of resistance almost did not change.

The mentioned differences, especially in the values of impact toughness at a low temperature, depending on the welding method are associated with changes in the phase-structural composition of the metal. The structure of 13KhGMRB steel represents a structure of tempered bainite, mostly lower, with the hardness of 253–264 *HV* (Figure 4). The structure of the upper

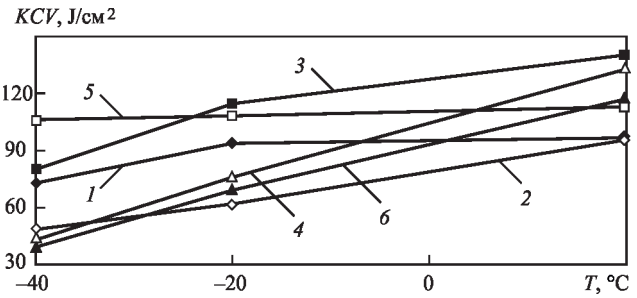

Figure 2. Impact toughness of welds and HAZ metal of welded joints of 13KhGMRB steel at different test temperatures *T*: ■ — HAZ, ▲ — weld; *1*, *2* — stationary arc; *3*, *4* — pulsating arc; *5*, *6* — PAW

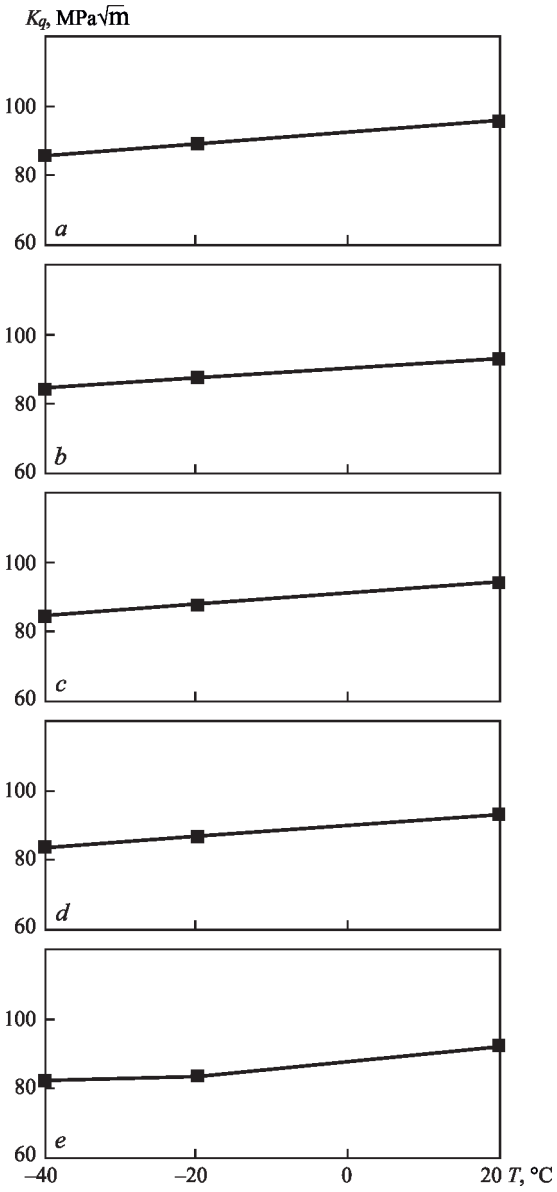

Figure 3. Resistance to brittle fracture of welds (*a*, *c*) and HAZ metal (*b*, *d*) of welded joints of 13KhGMRB steel in PAW (*a*, *b*) and pulsed-arc welding (*c*, *d*) and stationary arc (*e*)

weld layer in welding with a stationary arc consists mainly of fine-grained sorbite (Figure 5, *a*, *b*) with narrow thin precipitates of hypoeutectoid ferrite within cast crystals. The hardness of sorbite amounts to 274 *HV*. In the region of the coarse HAZ grain, a mixture of the upper and lower bainite with a hardness of 383 *HV* is observed. In the region of fine grain and in the region of partial recrystallization, a refinement of grain and a drop in hardness from 309 to 236–253 *HV* are observed.

In PAW, the structure of the upper weld layer consists of a mixture of upper and mostly lower bainite (Figure 5, *c*, *d*). The hardness of such a structure is within 317–336 *HV*. On the boundaries of cast crystallites, like in the stationary process, very thin precipitates of hypoeutectoid ferrite are observed. In the region of coarse HAZ grain, a martensitic structure with the hardness of 446–488 *HV* is observed. In the region of small grain and the region of partial recrystallization of HAZ, the sizes of grains become smaller and the hardness is reduced to 285 *HV*.

The structure of the upper layer of the specimen weld, produced by the pulsating arc, consists of a mixture of upper and lower bainite with a hardness from 262 to 314 *HV* (Figure 5, *e*, *f*). In the regions of cast crystallites, as in the previous cases, fine precipitates of hypoeutectoid ferrite are visible. In the region of coarse grain in HAZ, mainly a mixture of the upper and lower bainite with a hardness of up to 383 *HV* and small regions of martensite (401 *HV*) are observed. In the regions of small grain and partial recrystallization in HAZ, a refinement of grain and a drop in hardness to 366 *HV* is observed.

Thus, it was established, that despite the change in the welding process from stationary to pulsating and PAW, some changes occur in the formation of structures in the welds and HAZ metal of welded joints. Unlike the welds metal of welded joints made using an arc, which burns stationary and in which mostly the structure of sorbite is formed, in the metal of welds, joints made by welding with a pulsating arc and PAW, the upper and lower bainite is formed. Also changes in the structure of the welded joints HAZ metal oc-

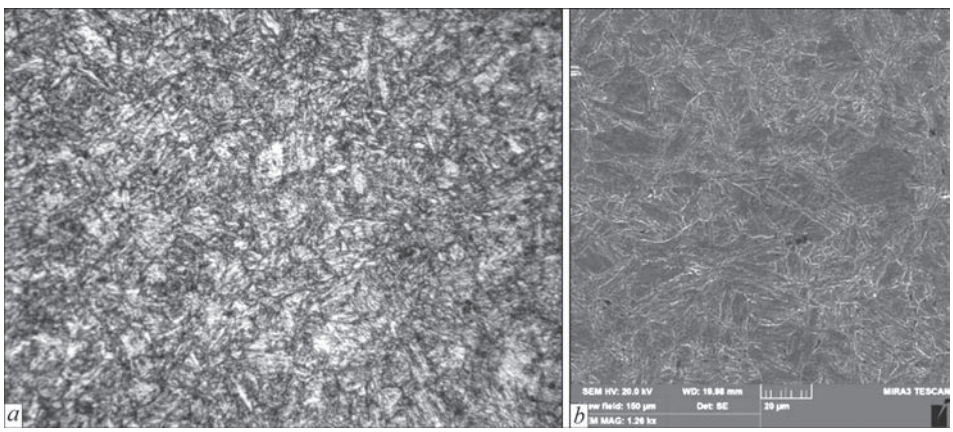

Figure 4. Structure of 13KhGMRB steel: *a* — optic microscopy at ×500 (2 times decreased); *b* — CEM

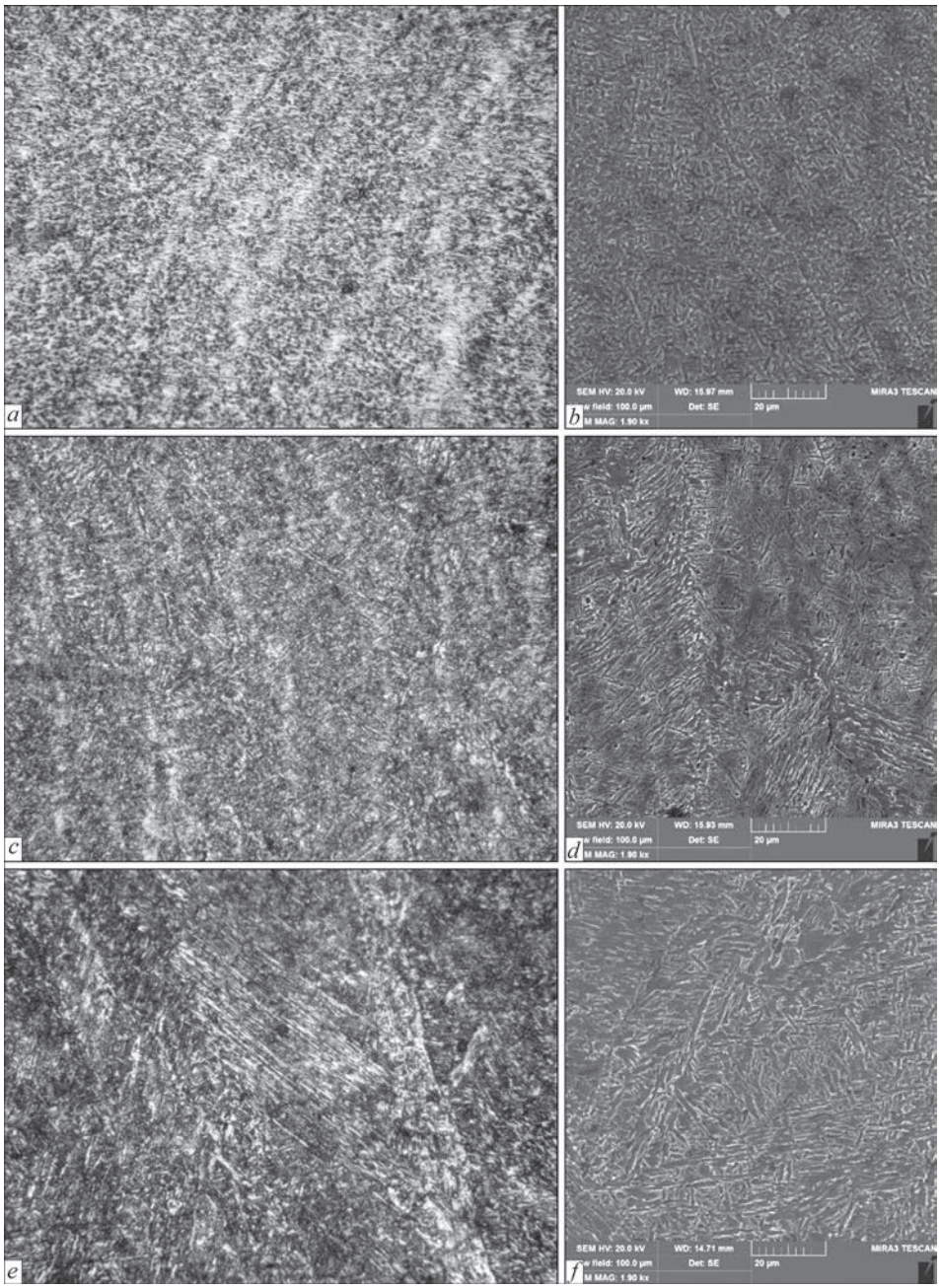

Figure 5. Structure of the upper weld layer in welding using stationary arc (*a*, *b*), in PAW (*c*, *d*) and pulsating arc (*e*, *f*): *a, c, e* — optic microscopy at ×500 (2 times decreased); *b*, *d*, *f* — CEM

cured. It was determined that unlike the HAZ metal of welded joints made using an arc that burns stationary and in which a bainite structure was formed, in a pulsed process of welding in the HAZ metal, small regions containing martensite are observed, in PAW in the region of HAZ overheating, only a martensitic structure of increased hardness is formed. Obviously, namely this predetermined the fact that in order to prevent the cold cracks formation in welded joints of 13KhGRMS steel, it is necessary to increase the temperature of their preheating. This is evidenced by the results of the abovementioned studies, the generalized

Table 1. Presence of cold cracks (CC) and depth of their propagation in the cross-section of joints (%) in PAW of low-alloy heat-strengthened steels

Steel grade	Welding method	Preliminary heating temperature T_p, °C			
		20	60	90	120
13KhGMRB	Stationary	CC (100 %)	CC (50 %)	Absent	–
	PAW	CC (100 %)	–	CC (up to 30 %)	Absent

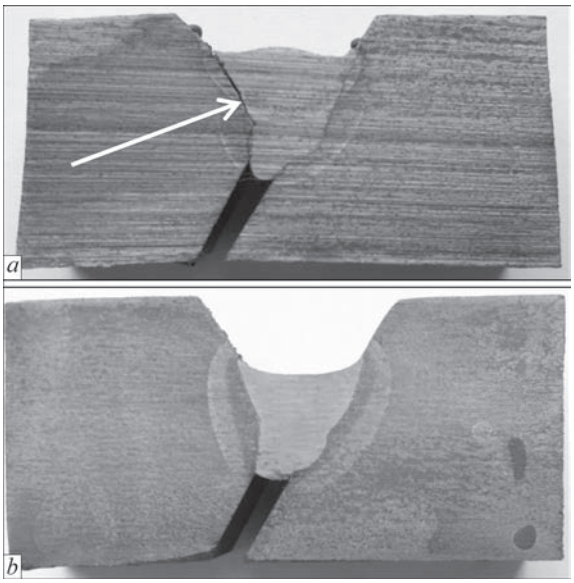

Figure 6. Macrosections of Tekken specimens of welded joints of 13KhGMRB steel, produced by PAW: *a* — without preliminary preheating; *b* — T_p = 120 °C

results of which are presented in Table 1 and typical macrosections from the Tekken specimens are given in Figure 6.

As is seen from the abovementioned material, in conventional welding using an arc that burns station-ary, the temperature of the preliminary heating (TP) of the Tekken specimens, which allows preventing the cold cracks formation in them, should be not lower than 90 °C. Regarding the Tekken specimens, the welding of which was performed by PAW, such a result can be achieved by increasing the temperature of the preliminary heating of the specimens to 120 °C (Figure 6, *b*, *c*).

Taking into account the results of the abovementioned studies, further in welding of T-joint specimens of 13KhGMRB steel, from which the specimens for testing on cyclic life were manufactured, preliminary heating of welded joints to a temperature of 120 °C was used, which was maintained at the expense of self preheating. The welding-on of the stiffeners to the steel plates was performed with a complete penetration and a leg of 12 mm. The generalized test results are shown in Figure 7.

It was determined that under the test conditions at a cycle stress of 30 MPa in both methods of welding, fatigue cracks in welded joints are not formed even after $2 \cdot 10^6$ load cycles. Instead, at a load of 35 MPa, fatigue cracks of a critical length (3 mm) were detected in places of transition from the weld to base metal, both in a stationary welding process, as well as in PAW, approximately at the same load cycles (respectively 1.8 and $1.86 \cdot 10^6$ cycles). With an increase in stresses to 40 MPa, a number of cycles, at which a fatigue crack was formed, significantly decreased. But

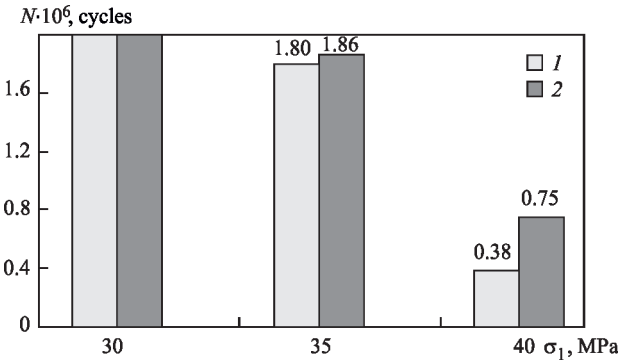

Figure 7. Resistance of T-welded joints of 13KhGMRB steel to fatigue cracks formation at cyclic bending load: *1* — stationary process; *2* — PAW

still, in PAW, they were approximately 2 times higher than in the stationary process (respectively, 0.38 and $0.75 \cdot 10^6$ cycles). In our opinion, such a difference can be explained by the formation of smoother transitions from the weld to base metal in PAW and a corresponding decrease in the level of stress concentration in this welded joint zone.

CONCLUSIONS

1. In pulsed-arc welding, compared to the stationary process, some changes occur in the formation of structures in the weld and HAZ metal of welded joints of low-alloy heat-strengthened 13KhGMRB steel. The structure of metals becomes more hardened. In the weld metal, an upper and mainly lower bainite (sorbite, 274 *HV*) with the hardness of 317–336 *HV* is formed. In the region of coarse HAZ grain, a martensitic structure with a hardness of 446–488 *HV* (bainite, 383 *HV*) is observed.

2. At the change in the welding process, the values of static strength and ductility of the welds metal of welded joints are comparable and are within $\sigma_{0.2}$ = = 713–740 MPa, σ_t = 786–800 MPa, δ_5 = 16–19 %, ψ = 59–67 %.

3. The influence of the arc welding process on the values of impact toughness of the welds and HAZ metal is ambiguous. Higher values of impact toughness are typical of the welds metal of welded joints made using the traditional arc welding process, namely using an arc that burns stationary. Traditionally, as the test temperature is reduced, the values of *KCV* decrease and at the test temperature of minus 40 °C, they are 43–49 J/cm^2, regardless of the welding process. The similar regularities concerning changes in impact toughness depending on the welding method are also observed for HAZ metal of welded joints. The exception is the results of testing specimens at a test temperature of minus 40 °C. At this test temperature, the specimens made from the welded joints produced using pulsed-arc welding, have the highest values of KCV_{-40} (108 J/cm^2).

4. The resistance of the welds and HAZ metal of welded joints, regardless of the welding method is at a high level ($Kq \geq 84$ MPa$\sqrt{m}$).

5. Due to the formation of a tempered martensitic structure in a pulsed-arc welding in the HAZ metal of welded joints of heat-strengthened 13KhGMRB steel, their resistance to cold cracks formation deteriorates. In order to avoid the formation of such cracks in welded joints, the heating of such joints should be increased from 90 to 120 °C.

6. The results of testing welded T-joint specimens of heat-strengthened 13KhGMRB steel on cyclic bending load showed that welded joints in pulsed-arc welding due to the formation of smoother transitions from the weld to base metal and a corre-sponding decrease in the level of stress concentration have an increased resistance to fatigue cracks formation.

REFERENCES

1. Lobanov, L.M., Poznyakov, V.D., Pivtorak, V.I. et al. (2009) Residual stresses in welded joints of high-strength steels. *Fiz.-Khimich. Mekhanika Materialiv*, **6**, 13–22 [in Ukrainian]
2. Berdnikova, O.M. (2021) Structural criteria of strength and crack resistance of high-strength steels and their welded joints. *Suchasna Elektrometal.,* **2**, 47–53 [in Ukrainian]. DOI: https://doi.org/10.37434/sem2021.02.07
3. Palani, P.K., Murugan, N. (2006) Selection of parameters of pulsed current gas metal arc welding. *J. Materials Proc. Technology*, **172**, 1–10.
4. Ghosh, P.K. (2017) *Pulse current gas metal arc welding*. New York, Springer.
5. Rimsky, S.T., Svetsinsky, V.G., Shejko, P.P. et al. (1993) Pulsed arc consumable electrode welding in argon-CO_2 mixture of low-alloy steels. *Avtomatich. Svarka,* **2**, 38–41 [in Russian].
6. Zhernosekov, A.M., Andreev, V.V. (2007) Pulsed metal arc welding (Review). *The Paton Welding J.,* **10**, 40–43.
7. Zhernosekov, A.M. (2012) Tendencies in development of control of metal transfer processes in shielding gases (Review). *The Paton Welding J.,* **1**, 29–33.
8. Zhernosekov, A.M., Fedorchuk, V.Ye., Kysla, H.P. et. al. (2022) Influence of the shape of pulses of welding currents on the properties of joints of aluminum alloys. *Mater. Sci.*, 58(**2**), 157–164. DOI: https://doi.org/10.1007/s11003-022-00644-4
9. Potapievsky, A.G. (2007) *Shielded-gas metal arc welding.* Pt 1. Welding in active gases. 2nd Ed. Kyiv, Ekotekhnologiya [in Russian].
10. Essers, W.G., Van Gompel, M.R.M. (1984) Arc control with pulsed GMA welding. *Weld. J.*, **63**, 26–32.
11. Lashchenko, G.I. (2006) *Methods of metal arc welding*. Kyiv, Ekotekhnologiya [in Russian].
12. Voropaj, N.M., Ilyushenko, V.M., Lankin, Yu.N. (1999) Features of pulsed arc welding with synergetic control of mode parameters. *Avtomatich. Svarka,* **6**, 26–32 [in Russian].
13. Pal, K., Pal, S.K. (2011) Effect of pulse parameters on weld quality in pulsed gas metal arc welding: A review. *J. Mater. Eng. and Performance*, 20(**6**), 918–931.
14. Yousefieh, M., Shamanian, M., Saatchi, A. (2011) Optimization of the pulsed current gas tungsten arc welding (PC-GTAW) parameters for corrosion resistance of super duplex stainless steel (UNS S32760) welds using the Taguchi method. *J. Alloys Compd.*, **509**, 782–788. DOI: https://doi.org/https://doi.org/10.1016/j.jallcom.2010.09.087
15. Goyal, V.K., Ghosh, P.K., Saini, J.S. (2009) Analytical studies on thermal behaviour and geometry of weld pool in pulsed current gas metal arc welding. *J. Materials Proc. Technology*, 209(**3**), 1318.
16. Palani, P.K., Murugan, N. (2006) Selection of parameters of pulsed current gas metal arc welding. *J. Mater. Proc. Technology*, 172(**1**), 10.
17. Zavdoveev, A.V., Poznyakov, V.D. Rogante, M. et al. (2020) Features of structure formation and properties of joints of S460M steel made by pulsed-arc welding. *The Paton Welding J.*, **6**, 9–13. DOI: https://doi.org/10.37434/tpwj2020.06.02
18. Zavdoveev, A., Poznyakov, V., Kim, H.S. (2020) PC-GMAW effect on the welding thermal cycle and weld metal geometry for high strength steels. *Int. J. of Engineering and Safety Sci.*, **1**, 5–16. DOI: https://doi.org/10.16926/ijess.2020.01.01

ORCID

O.A. Gaivoronskyi:0000-0002-5922-5541,
V.D. Poznyakov: 0000-0001-8581-3526,
S.L. Zhdanov: 0003-3570-895X,
A.V. Zavdoveyev: 0000-0003-2811-0765

CONFLICT OF INTEREST

The Authors declare no conflict of interest

CORRESPONDING AUTHOR

V.D. Poznyakov
E.O. Paton Electric Welding Institute of the NASU
11 Kazymyr Malevych Str., 03150, Kyiv, Ukraine.
E-mail: paton39@ukr.net

SUGGESTED CITATION

O.A. Gaivoronskyi, V.D. Poznyakov, S.L. Zhdanov, A.V. Zavdoveyev, A.O. Maksymenko, A.M. Denysenko (2023) Structure and properties of welded joints of 13KhGMRB steel in pulsed-arc welding. *The Paton Welding J.*, **10**, 3–9.

JOURNAL HOME PAGE

https://patonpublishinghouse.com/eng/journals/tpwj

Received: 13.07.2023
Accepted: 14.11.2023

DOI: https://doi.org/10.37434/tpwj2023.10.02

FEATURES OF WELDING DUPLEX STAINLESS STEELS IN WET UNDERWATER WELDING IN COMPARISON WITH WELDING IN AIR (REVIEW)

S.Yu. Maksymov, G.V. Fadeeva, A.A. Radzievska, D.V. Vasyliev

E.O. Paton Electric Welding Institute of the NASU
11 Kazymyr Malevych Str., 03150, Kyiv, Ukraine

ABSTRACT

The presented review shows that the main task in welding duplex stainless steels (DSS) is ensuring the conditions which should promote reduction of the negative impact of the welding thermal cycle on the microstructure and change of the initial balance of the phase components, particularly in the high-temperature region of the HAZ. In welding duplex stainless steels the required ratio of ferrite and austenite in the weld metal is provided by changing the chemical composition, and in the HAZ it is achieved due to lowering of the cooling rate. Depending on cooling rate $w_{13/8}$ or time of staying predominantly in the temperature range of phase transformations, the respective microstructure of metal of the weld and HAZ is formed with the specified ratio of phase components of austenite and ferrite, which, in its turn, affects the mechanical properties and corrosion resistance of duplex steel welded joints. A clear correlation of the mechanical properties is observed, depending on austenite and ferrite content in the weld metal. With increase of the cooling rate, the quantity of precipitates of excess phases, Cr_2N chromium nitrides, becomes greater. It was found that in view of intensive cooling impact of the water environment, the volume fraction of austenitic phase is lower in the metal of the weld and in the HAZ high-temperature region in wet underwater welding, compared with volume fraction of the austenitic component in welding in air at the same heat input values. With increase of the energy input, a significant increase of volume fraction of austenitic phase is observed, particularly in wet underwater welding. Considering the features, characteristic for wet underwater welding, the energy input levels and chemical composition of weld metal require correction as regards the recommendations, which were developed for welding in air.

KEYWORDS: duplex steels, wet underwater welding, energy input, cooling rate, phase composition, austenite, ferrite, microstructure, welding thermal cycle

INTRODUCTION

The idea of creation of duplex stainless steels arose in 1920s, and the first melt was done in 1930 in Avesta, Sweden. Duplex stainless steels were introduced and have been actively developed by European companies since 1935 [1]. New generation ferritic-austenitic steels feature a lower carbon content, usually, not higher than 0.02–0.03 %, and additional alloying by nitrogen in the amount of 0.10–0.27 % for standard duplex stainless steel (DSS). Nitrogen content in super duplex stainless steels (SDSS) is in the range of 0.24–0.32 [2, 3]. A noticeable increase in the share of duplex steel application has occurred only in the last 30 years due to improvement of the production technology, particularly of the processes of controlling nitrogen content in steels [4].

The main fields of application of duplex stainless steels are oil and gas, petrochemical, pulp and paper industries. At present the areas of their application have extended to metal structures, operated in water environment, in particular, at construction of marine and nuclear power plants, pipelines for transportation of sulphurous gas, oil and sea water, due to a favourable combination of high mechanical strength and general and local corrosion resistance, as well as resistance to cracking caused by interaction of stresses and hydrogen, the source of which is an acidic medium of liquid carbohydrates [5]. In the presence of hydrogen sulphide and chlorides the risk of stress corrosion cracking becomes greater. Such media can be present, for instance, in oil and gas producing wells, including in sea water [6].

An optimal combination of high characteristics of strength and resistance against, in particular, pitting corrosion, as well as stress corrosion cracking is ensured at 1:1 ratio of the ferritic and austenitic phases in the metal structure, i.e. at 50 % content of each of the components. Such characteristics are achieved by annealing at the temperature of 1020–1100 °C for 5 min with subsequent quenching in water for DSS 2205 standard steel [2], and for SDSS 2507 super duplex steel the hardening annealing temperature is equal to 1040–1120 °C [2, 6]. The higher the annealing temperature, the higher is the ferritic component content [6]. Thus, solid solution annealing is the as-delivered condition of duplex steels. Annealing temperature depends on the alloy chemical composition, as well as on the steel making technology accepted in production.

Duplex steels usually have good weldability, and they can be welded by most of the welding methods, applied for austenitic stainless steel. Under the influence of the welding thermal cycle (WTC) the

austenitic-ferritic phase balance is disturbed, as a result of the impact of high heating and cooling rates, characteristic for different welding methods. One of the main tasks in welding duplex stainless steels is ensuring the conditions, which would promote reduction of the negative influence of the high heating and cooling rates and preservation of the initial balance of the microstructure to varying degrees, which ensures the main technological characteristics of the welded joints, such as mechanical and corrosion properties.

CONTROLLING THE STRUCTURE OF THE WELDED JOINT METAL

Preservation of the required austenite-ferrite balance can be achieved in two ways: change of the chemical composition and lowering of the cooling rate in welding. The first variant is usually realized at selection of filler material for weld metal of the welded joint. The type of weld metal alloying is chosen with a greater austeniticity margin due to increase of nickel content, as well as with additional alloying by nitrogen. Thus, the Cr_{eq}/Ni_{eq} ratio is reduced, which corresponds to an increase towards austeniticity. If Cr_{eq}/Ni_{eq} ratio, for instance for 2205 steel is in the range of 2.25–3.50 within the admissible values by EN 1.4462 standard (Figure 1) [4, 7], then for filler metal Cr_{eq}/Ni_{eq} ratio will be much smaller. For manual arc welding of 2205 steel in keeping with DSTU EN ISO 3581:2021, it is recommended to use electrodes with 2209 alloying type, which correspond to nominal composition of 22 9 3 NL [8].

Application of filler material with the composition, equivalent to that of the base metal, would shift the balance towards ferrite, because of a high cooling rate.

A measure of the cooling rate is the welding energy input, which is inversely proportional to it. Recommendations and standards on duplex steel welding were developed, which specify application of energy input in the range of 0.5–2.5 kJ/mm for welding standard duplex steel of 2205 type with 22–23 % chromium and 0.5–1.5 kJ/mm for super duplex stainless steel of 2507 type with 25 % chromium [9–13]. Moreover, reference publications give different values of energy input, which is a measure of general heat input per a unit of weld length. IIW recommends keeping the energy input in the range of 1.2–2.0 kJ/mm for welding 2205 steel, BOHLER and Sandvik manufacturers of consumables recommend 1.0–3.0 kJ/mm [14–16]. There are no universal recommendations, because of a large number of welding parameters, so that selection and optimization of the welding parameters, including energy input values, are done in each concrete case.

It is generally accepted that the lower limit of energy input of 0.5 kJ/mm to some extent promotes preservation of microstructure balance within the admissible limits, namely formation of a sufficient quantity of austenite to ensure the required mechanical properties of the metal of the weld and welded joint. The upper value of energy input is limited to reduce the volume of precipitation of the secondary phases, which lower the corrosion resistance.

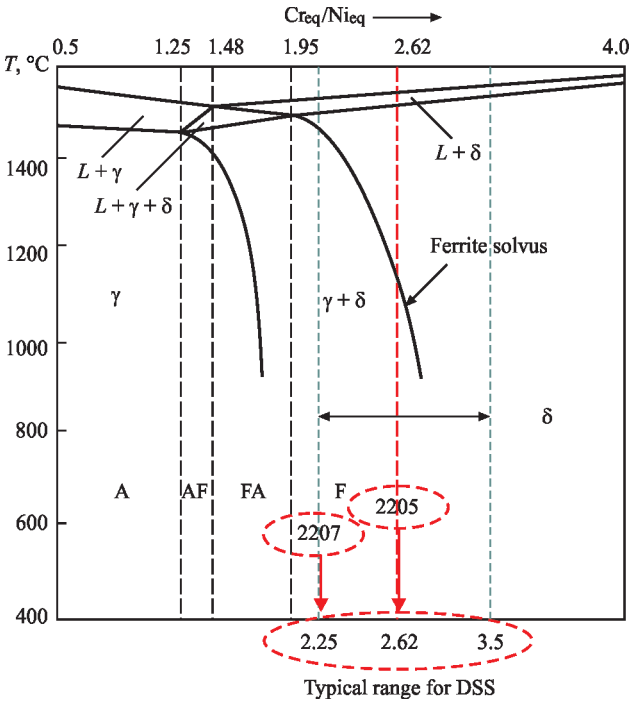

Figure 1. Pseudobinary (Fe–Cr–Ni) diagram plotted using Cr_{eq}/Ni_{eq} equivalent ratio

Increase of energy input from 0.7 to 1.2–1.3 kJ/mm in welding SDSS 2507 super duplex stainless steel promoted an increase of weld metal impact toughness. Impact energy at Charpy V-notch was equal to 45 J at testing at –40 °C temperature, which is much higher than the required value of 27 J [17]. Studies have also appeared, which show that the energy input limitation to 1.5 kJ/mm is not justified in welding SDSS 2507 super duplex stainless steel, particularly when joining large thicknesses (20 mm and greater), and which recommend widening the range of admissible energy input. Good properties of the weld metal were achieved in welding with energy input of 2.1–2.2 kJ/mm [18]. In work [19] the influence of the removed heat on the microstructure, mechanical properties and corrosion resistance of welded joints of SDSS UNS S32750 super duplex steel was studied. Welding was conducted with different energy inputs of 0.54 and 1.1 kJ/mm. Investigations led to the conclusion, that application of a low heat input may be better, as there is no great difference in the weld properties, depending on the used heat input.

The influence of the heat input level in the range from 0.45 to 0.60 kJ/mm was studied in welding dis-

similar joints of DSS 2205 duplex stainless steel with ASS 316 L austenitic stainless steel. Low heat input demonstrated a higher hardness and tensile strength, as a result of a higher content of ferrite and higher cooling rate. The higher energy input improved the corrosion resistance [20].

The given data demonstrate that there is no common approach to determination of the heat input level and that the energy input is not the only factor responsible for formation of the microstructure in the weld metal and in the HAZ to ensure the required balance of phase components of austenite and ferrite.

The energy input levels recommended in instructions and standards, should promote formation of a microstructure with the required content of the austenitic and ferritic components in different regions of the welded joint. Ferrite content in the weld metal and in the HAZ should be in the range of 25–70 %, in order to ensure the optimal mechanical properties and corrosion resistance [21]. The following ferrite levels are believed to the generally accepted:

- base metal (BM) — 35–55 %;
- weld metal (WM) — below 60 %;
- HAZ — below 65 %. Sometimes, up to 70 % are allowed in the HAZ.

Some industry standards limit the ferrite component content even more. The requirements pertaining to oil and gas industry are given in Table 1.

The rate of cooling of metal of the weld and HAZ depends on a totality of such factors, as welded metal thickness, welding technology (welding process efficiency), energy input, welding mode, welding environment, and many others.

Welding energy input is just a guiding parameter, which to a certain extent can determine the cooling rate, and, thus, the time of metal staying in the region, where the polymorphous transformation of ferrite (δ) into austenite (γ) takes place. In keeping with the pseudobinary Fe–Cr–Ni state diagram the start of δ→γ transformation depends on the alloy chemical composition, and the transformation completeness depends on the time of staying in this two-phase region (Figure 1) [4, 7]. Therefore, the cooling rate, alongside the alloy chemical composition, determines the time of staying in the two-phase region. Austenite transformation from ferrite takes place in the solid state, as this is a diffusion process. The transformation completeness depends on the time of staying in this range of the two-phase state.

Table 1. Ferrite content in the welded joint according to standards

Standard name	Ferrite content, %		
	BM	HAZ	WM
API RP 582 (API A 938C) [22]	30–65	30–65	30–65
NORSOK M630 D45 [23]	35–55	30–70	–
Specification for oil and gas industry	35–55	<60–65	<60

The model of metal crystallization can be determined by Cr_{eq}/Ni_{eq} ratio. For 2205 duplex steel of certain chemical composition it corresponds to the value of 2.62 (Figure 1). The range of Cr_{eq}/Ni_{eq} ratio within the tolerances by chemical composition for 2205 steel (EN 1.4462) is equal from 2.25 to 3.5, i.e. it is quite wide.

With such a ratio the crystallization model is as follows:

$$L \rightarrow L+\delta \rightarrow \delta+\gamma.$$

The temperature range of δ→γ phase transformations is 1200 °C (1300)–800 °C, and it depends on the metal chemical composition. This is a diffusion process, it involves temperature and time. That is, the completeness of δ→γ phase transformations depends on the metal chemical composition, cooling rate and time of staying in the temperature range of 1200 (1300)–800 °C, which also depends on the cooling rate. In the opinion of authors of [24], the metal chemical composition has a greater influence on the final ferrite/austenite ratio than does the cooling rate. It is shown that the change of chemical composition of 2205 duplex steel in the range of tolerances for steel, towards increase of austenite-forming element content, namely nickel, up to 6.0 % on the upper level, as well as nitrogen up to 0.18–0.19 %, ensured producing less than 70 % ferrite in the HAZ metal at all the cooling rates from 20 to 100 °C/s at the temperature of 700 °C. In a similar way, much higher values were obtained at impact testing at a low temperature (–46 °C). This steel was called Arctic 2205 [25].

In work [18] the weld metal cooling rate was calculated in welding 20 mm SDSS 2507 super duplex steel by experimental data with recording of the welding thermal cycles. Two welding technologies were used: mechanized gas-shielded welding with 1.2 mm solid wire (GR experiment) and with 1.2 mm flux-cored wire (FR experiment). Different cooling rates were obtained at the same energy input in GR (1.2–1.3 kJ/mm) and FR (1.1–1.3 kJ/mm) (Figure 2). In flux-cored wire welding the cooling rate is much lower than in solid wire welding: by almost 10 °C/s and more in the temperature range of 1200–800 °C. So, in the fifth layer the cooling rate in FR is 50 °C/s, and in GR it is 60 °C/s.

It was also noted that the cooling rate increased with the number of layers. The lowest cooling rate was recorded in solid wire welding at greater energy input (GH) = 2.2 kJ/mm. In this study also a conclusion was made that it is exactly the cooling rate,

and not the time of staying in the critical temperature range of 1200–800 °C, which is the key factor of nitride formation.

Conducted analysis of the influence of welding technology on phase composition and internal stresses of welded joints of austenitic and duplex steels showed that such highly-productive and promising types of welding, as electron beam (EBW) and laser (LW) have a negative influence on phase composition of two-phase (duplex) steels and single-phase steels, because of high cooling rates of the welded joints [26]. At EBW of 2205 duplex steel variation of the electron beam power and focal distance allowed lowering the cooling rates and ensuring satisfactory ferrite content (~70 %). In this case, the time scheme was used, i.e. the time of staying in the critical temperature range of 1200–800 °C. At cooling rate, which ensured cooling during 4.5 s, 84–87 % ferrite formed, at cooling rate resulting in cooling within 7.4 s it was 79–84 % ferrite, and at cooling rate ensuring the time of 17.7 s the amount of ferrite was 69–70 % [27].

The data given in [18, 25–27] demonstrate how the different factors, namely welding process, energy input, metal chemical composition, and cooling rate can be responsible for the impact on formation of the microstructure, phase composition and amount of excess phase precipitates, including nitrides.

In addition to recommendations on the specific heat input, there is also the concept, in which $\tau_{12/8}$ time scheme is used (time required for cooling from 1200 to 800 °C), which describes the cooling conditions. Such a procedure for determination of the cooling conditions, involves certain difficulties, as it requires placing the thermocouples in the weld pool [2]. In keeping with this concept, it is recommended to conduct cooling of the welded joint in this temperature range for 10 s. In such a case, optimal microstructure and properties of the metal being welded are achieved [28].

Microstructure (HAZ) of duplex stainless steel undergoes more complex transformations and is the result of two mutually opposite processes. First, the process of transformation of the initial austenite fraction into ferrite γ→δ takes place under the influence of welding thermal cycle at heating and at achievement of temperature above the ferrite solvus region (T = 1250–1300 °C), which depends on the metal chemical composition, and then, at further cooling, the reverse transformation δ→γ occurs when the ferrite solvus temperature has been reached.

HAZ microstructure evolution depends on certain factors, namely base metal initial microstructure, maximal temperature in a specific region of the HAZ, time of staying at the maximal temperature and heating and cooling rate, i.e. on the actual WTC.

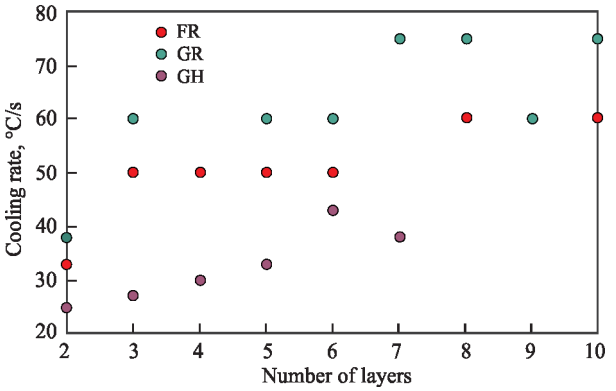

Figure 2. Average rate of cooling from 1200 to 800 °C, depending on the number of welding passes and welding procedure, where FR and GR is flux-cored wire and solid wire welding in the recommended energy input modes, respectively, GH — at higher energy input

The majority of studies currently presented in publications, mostly confirm the influence of the cooling rate on the microstructure and phase composition of HAZ and weld metal, which, in its turn affects the mechanical properties and corrosion resistance of the welded joints. Somewhat contradictory are the data on the temperature range and time parameter, which should be selected as the criteria, which are determinant for formation of the microstructure and phase composition of the metal of the weld and HAZ.

In study [29] the author emphasizes that as the temperature range of ferrite transformation into austenite, which usually is from 1200 to 800 °C, depends on the steel chemical composition, the parameter of cooling time between 1200 and 800 °C ($\tau_{12/8}$) should be used for characterization of temperature cycles of duplex steel welding. That is, this is exactly the range, which is the criterion of duplex steel weldability, and not the one between 800 and 500 °C, i.e. ($\tau_{8/5}$), as it is usually accepted for structural steels. The cooling rate in this range will determine the quantity of ferrite produced in the final microstructure. If the cooling time ($\tau_{12/8}$) is the criterion for determination of the HAZ final microstructure and phase composition, then the cooling rate in the temperature range from 1200 to 800 °C also is the determinant value, i.e. $w_{12/8}$, and not $w_{8/5}$.

When developing the model characterizing the content of ferrite, depending on the cooling rate, the authors of work [25] used the rate of cooling at 700 °C as the criterion. Other criteria were tested in a similar way, such as the rate of cooling at 1000 °C, or time of cooling from 800 to 500 °C, or from 1100 to 900 °C. Even if the ferrite-austenite transformation takes place at a high temperature of 1200 °C, the rate of cooling at 700 °C turned out to be the most accurate for prediction of duplex steel HAZ microstructure, compared to other criteria [30].

INFLUENCE OF WATER ENVIRONMENT ON WELDED JOINT STRUCTURE AND PROPERTIES

Despite the wide application of duplex steels, the influence of water environment on welded joint structure and properties has been little studied. Results of extensive research or reports on the behaviour of duplex steels in underwater welding and properties of the produced joints are found in publications. The majority of available results of the conducted experiments were derived at application of manual welding by commercial electrode materials, developed for application in air, as specialized electrode materials for wet underwater welding still have not been developed [31, 32].

At present there exist several technologies: wet underwater welding and dry underwater welding. Wet underwater welding is performed directly in the water environment. Dry underwater welding, in its turn, is subdivided into local dry welding, when only the arc burning zone is protected from the water environment, and welding in the chamber, completely protected from the water environment. The latter is, as a rule used in welding critical structures.

An example of application of electrodes developed for welding in air, in wet underwater welding of duplex steels is given in work [32]. It is noted that the arc was unstable, and internal welding defects such as pores, gas cavities and cracks in the weld root were also found. Welding stability improved at voltage increase up to 62.3 V. Ferrite content in the metal of the welds and HAZ increased slightly in wet underwater welding, compared to welding in air, although it is difficult to make any conclusions, as welding in air and under the water was conducted at application of different technologies and with different energy inputs. Welding in air was conducted with 1.2 mm solid wire for gas-shielded welding (Casto MAG 45505 S), and in wet underwater welding 4 mm diameter electrodes of BOHLER FOXCN 22/9N/EN 1600 – EN 22 9 3 N LR 32 brand were used.

In dry hyperbaric flux-cored wire welding of sparsely-alloyed UNS S 32101 duplex steel [33–36] in the hydrostatic pressure range from 0 to 0.75 MPa the most well-balanced microstructure is demonstrated by weld metal produced at the pressure of 0.45 MPa with average austenite content of 53.3 %. The balanced ferrite-austenite microstructure of the weld metal prevented precipitation of excess phases, namely Cr_2N chromium nitrides, while in the HAZ precipitation of Cr_2N chromium nitrides was observed at austenite content of 36 %. Weld metal met the requirements of ASTM A923 (2014), which allows limit value of absorbed energy of 34 J [34]. A higher total energy input q = 3.16 kJ/ mm at the same depth provided more time for austenite transformation in the weld metal, which is one of the causes for its higher content in the weld metal. In welding at the pressure of 0.75 MPa, the total energy input was equal to 2.97 kJ/mm, and in welding without pressure and at the pressure of 0.15 MPa it was 2.38 kJ/mm (Table 2). Thus, a clear correlation between austenite content in the weld metal and energy input in welding is observed [33].

Weld metal, produced in welding at the pressure of 0.45 MPa, also had higher resistance against pitting corrosion and mechanical properties [35, 36].

Analysis of the conducted research [33–36] led to the conclusion that the largest quantity of austenite in the weld metal is achieved in welding with the highest total energy input q = 3.16 kJ/mm, which ensures better integrated characteristics of resistance to pitting corrosion and mechanical properties of welded joints.

Work [37] is a study of water environment influence in welding S32101 duplex steel by 1.6 mm self-shielded E 2209-T-0-4 flux-cored wire, developed for welding in air. Unstable arc burning and unsatisfactory formation of weld metal were observed in

Table 2. Parameters of dry hyperbaric flux-cored wire multilayer welding

Ambient pressure, MPa	Number of layers	Current, A	Voltage, V	Welding speed, mm/s	Heat input, J/mm
0 — normal	1 — root	170	28	4	1190
	2 — finish	180	29	4.4	1186
0.15	1 — root	170	28	4	1190
	2 — finish	180	29	4.4	1186
0.45	1 — root	160	27	4	1080
	2 — fillingя	170	28	4.8	992
	3 – finish	180	29	4.8	1088
0.75	1 — root	150	26	4.4	886
	2 — fillingя	170	28	4.8	992
	3 — finish	180	29	4.8	1088

Table 3. Values of welding parameters and heat input

Sample number	Welding speed, V_w, mm/s	Welding depth, m	Welding current I_w, A	Voltage U_a, V	Heat input q, J/mm
UDW 1	8	20	220	26.4	726
UWW 1	8	20	220	26.4	726
UDW 2	7.2	20	260	30	1083.3
UWW 2	7.2	20	260	30	1083.3
UDW 3	7.2	20	300	33.2	1383.3
UWW 3	7.2	20	300	33.2	1383.3

Note. UDW — dry underwater welding; UWW — wet underwater welding.

welding. With welding depth increase from 0.1 to 40 and 80 m metal porosity becomes greater and is equal to 1.51, 9.08 and 11.17 %, respectively. The same is observed with increase of depth: weld metal microstructure is refined, and HAZ width is reduced, contrarily, and it is equal to 0.15 mm (150 μm) at 0.1 m depth; 0.1 mm (100 μm) at 40 m depth, and 0.08 mm (80 μm) at 80 m depth. Lowering of ferrite content

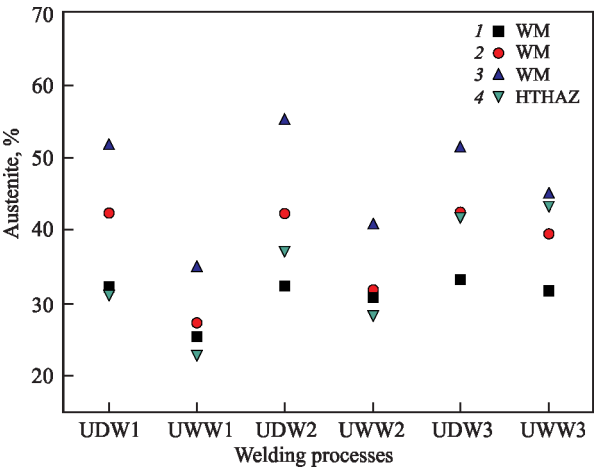

Figure 3. Volume fraction of γ-phase austenite at different welding methods and modes in different welded joint regions: *1* — weld surface; *2* — weld center; *3* — weld region, adjacent to the fusion line; *4* — HTHAZ — high temperature heat-affected zone

in the weld center was also found: 21.1, 24.3 and 15.5 %, respectively. Austenite content in the weld metal is higher in welding at 80 m than at 40 m.

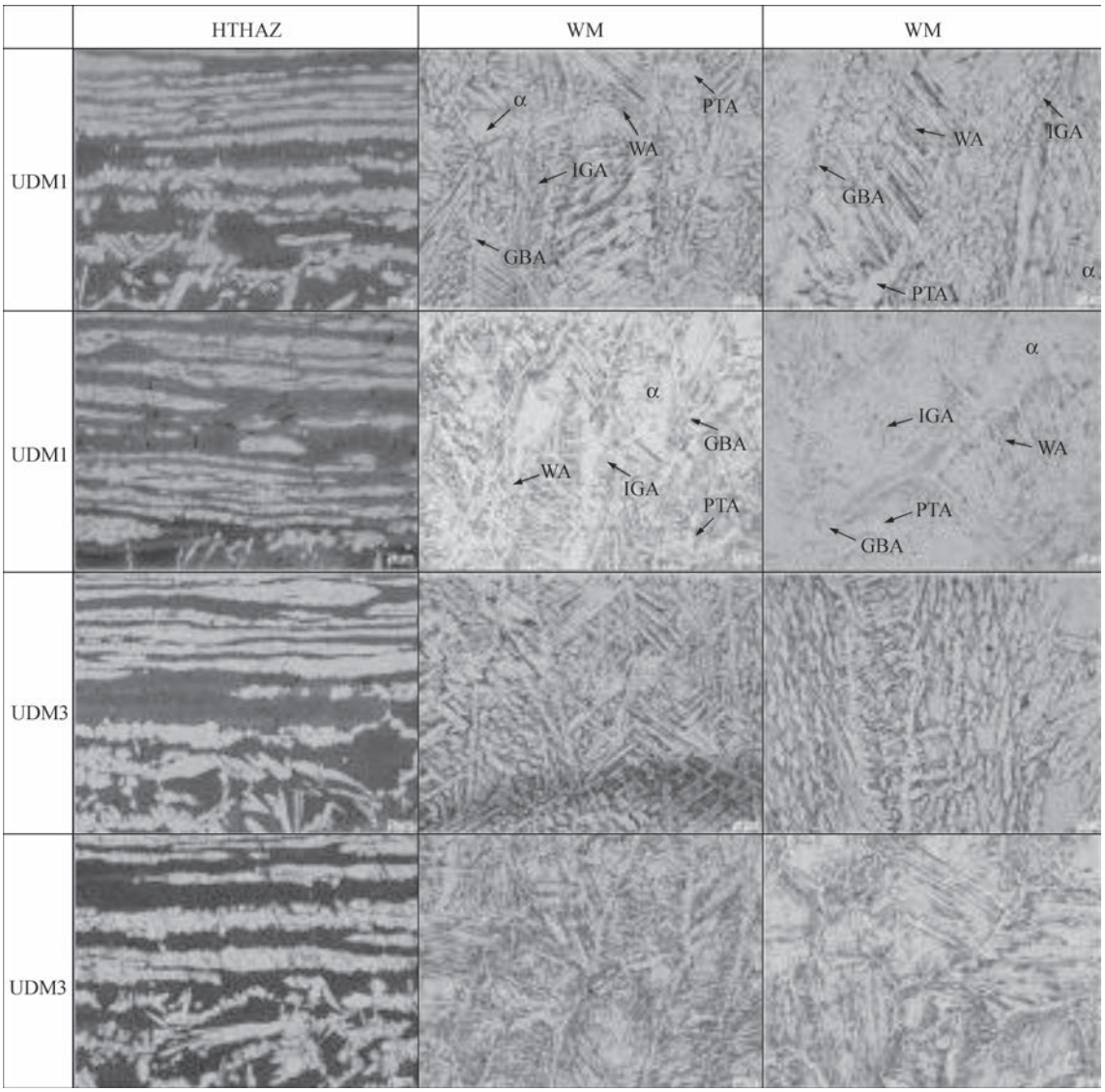

Figure 4. Microstructure of different regions of welded samples made by welding in air and by wet underwater welding

Comparative studies of the microstructure of the metal of the weld and HAZ in dry welding of UNS S32101 duplex steel with 1.2 mm flux-cored wire in CO_2 shielding gas in the pressure chamber and directly in the water environment were conducted in [38]. Table 3 gives welding and heat input parameters.

Figure 3 shows the volume fraction of γ-phase austenite at different welding methods and modes in different regions of the welded joint.

Analysis of the data given in Figure 3, leads to the following conclusions:

- volume fraction of γ-phase in wet underwater welding is much lower in all the weld metal regions and in the high-temperature subzone of the HAZ (HTHAZ), compared to γ-phase volume fraction in dry welding at the same heat input values;
- with increase of energy input value from 0.726 to 1.383 kJ/mm the γ-phase volume fraction increases in wet underwater welding from 27.3 % — UWW 1 to 39.4 % — UWW 3, i.e. 1.5 times, while in dry underwater welding it changes only slightly, remaining almost constant (~42 %) — weld center;
- at all the energy input levels the same regularity of γ-phase content in different welded joint regions is found in the case of wet and dry underwater welding. The largest volume fraction of γ-phase is observed in the weld metal adjacent to the fusion line, and the smallest γ-phase fraction is in HTHAZ;
- γ/α values increased greatly in wet underwater welding for weld metal, adjacent to the fusion line: from 35.01 % for UWW 1 up to 44.9 % for UWW 3.

Increase of γ-phase content in wet underwater welding is less intensive in weld regions adjacent to the fusion line: UWW 1 — 35.01 %; UWW 3 — 44.9 %, i.e. almost 1.3 times increase.

The most intensive increase of γ -phase content in wet underwater welding occurs in HTHAZ from UWW 1 — 23 % to UWW 3 — 43.55 %, by almost 1.9 times. In dry welding increase of γ-phase content in HTHAZ is less pronounced — from UDW 1 — 31.34 % to UDW 3 — 41.55 %, i.e. by more than 1.3 times.

Figure 4 gives the microstructure in different regions of welded joints.

Authors of [38] note that the volume fraction of nitrides is decreased with increase of energy input. It is also noted that HTHAZ cooling rate in wet underwater welding is higher than in dry welding.

HTHAZ for UDW 3 showed optimal local corrosion resistance, and the lowest local corrosion resistance was found in UWW 1.

Data given in Table 3 and in Figure 3 demonstrate that the cooling rate decreases with increase of energy input, and the austenitic component fraction is increased. The probability of chromium nitride formation in wet underwater welding rises, compared to dry welding, as a result of increase of the cooling rate and lowering of austenitic component volume fraction.

It is shown in the presented review that the cooling rate is one of the main factors, having the strongest influence on the HAZ microstructure and phase composition in all the welding processes at the same chemical composition. The appropriate HAZ microstructure with the respective ratio of austenitic and ferritic phase components is formed depending on the cooling rate.

CONCLUSIONS

1. It is desirable to adjust the energy input ranges, which are recommended for welding duplex steels by different technologies, during technology optimization, depending on chemical composition of the metal being welded.

2. Investigations confirm the influence of the cooling rate on the microstructure and phase composition of the metal of the weld and HAZ, which, in its turn, influences the mechanical properties and corrosion resistance of the welded joints.

3. Completeness of δ→γ phase transformations depends on the metal chemical composition, cooling rate and time of staying in the temperature range of 1200 (1300)–800 °C, which also depends on the cooling rate.

4. Due to the cooling impact of water environment, the cooling rate in wet underwater welding, particularly in HTHAZ, is higher than in welding in air.

5. Austenite content in the metal of the weld and in the HAZ is directly proportional to the energy input and inversely proportional to the cooling rate.

6. Increase of energy input promotes an increase of the austenitic component in wet underwater welding to a greater degree, particularly in HTHAZ, than in welding in air.

7. With increase of energy input, the volume fraction of precipitation of excess phases, Cr_2N chromium nitrides, becomes smaller.

8. Considering the peculiarities inherent to wet underwater welding, the levels of energy input and weld metal chemical composition require correction, as regards the recommendations developed for welding in air.

REFERENCES

1. Charles, J., Ehemelle, P. (2010). The history of duplex developments, nowadays DSS properties and duplex market future trends. In: *Proc. of the 8th Duplex Stainless Steels Conf.* Beaune, EDP Sciences.
2. Amman, T. (2007) Shielded-gas arc welding of duplex steels. *Svetsaren*, 62(**1**), 41–45.
3. *Austenitic-ferritic steels*. http://www.weldzone.info: 795 — austenito-ferritnye stali.
4. Verma, J., Taiwade, R.V (2017) Effect of welding processes and conditions on the microstructure, mechanical properties and corrosion resistance of duplex stainless steel weldments: A review. *J. of Manufacturing Processes*, **25**, 134–152.

5. Labanowski, J., Eydrych, D., Rogaldki, C., Samson, K. (2011) Underwater welding of duplex stainless steel. *Solid State Phenomena*, **183**, 101–106.
6. *Duplex stainless steel.* http://www.outokumpu.com.
7. Lippold, J.C., Kotecki, D. (2005) *Welding metallurgy and weldability of stainless steel*. Joh Wiley and Sons, Inc.
8. DSTU EN ISO 3581:2021: *Welding materials. Covered electrodes for manual arc welding of stainless and heat-resistant steels*. Classification.
9. (2006) *How to weld duplex stainless steels*. Document 10601 EN – CB. Avesta welding AB, Avesta, Sweden.
10. (2006) *Welding guidelines for duplex & superduplex stainless steels*. Metrode Products Ltd., Chertsey, UK.
11. Pettersson, C.-O., Fager, S.-Å. (1995) *Welding practice for the sandvik duplex stainless steels SAF 2304, SAF 2205 and SAF 2507.* Technical Document S-91-57. AB Sandvik steel, Stockholm, Sweden.
12. DIN EN 1011-3:2019: *Schweißen – Empfehlungen zum Schweißen Metallischer Wekstoffe — Teil 3*. Lichtbogen Schweißen von Nichtrostenden Stahlen.
13. DSTU EN ISO 1011-3: 2021: *Welding. Recommendations for welding metal materials.* Pt 3. Arc welding of stainless steels.
14. *Welding of duplex stainless steels.* http://www.avestawelding.com/4976.epibrw.
15. *Welding of duplex stainless steels.* BÖHLER Welding. http://www.bohlernn.ru.
16. Sandvik SAF 2205*: Sandvik Materials Technology*. http://www.smt.sandvik.com/en/materials-center/material-data-sheets/tube-and-pipe-seamless/sandvik-saf-2205
17. Kotecki, D.J. (2010) Some pitfalls in welding of duplex stainless steels. *Soldagem & Inspecao*, 15(**4**), 336–343.
18. Bermejo, M.A.V., Daniel, E., Hurtig, K., Karlsson, L. (2019) A new approach to the study of multi-pass welds-microstructure and properties of welded 20-mm-thick superduplex stainless steel. *Applied Sci.*, **9**, 18. DOI: https://doi.org/10.3390/app9061050.
19. Gupta, A., Baskaran, A.K.T., Arya, S.B., Khatirkar, R.K. (2018) Effect of heat input on microstructure and corrosoin behavior of duplex stainless steel shielded metal arc welds. *Transact. Indian Inst. Met.*, **71**, 1595–1606. DOI: https://doi.org/10.1007/s12666-018-1294-z
20. Verma, J., Taiwade, R.V., Khatirkar, R.K. et al. (2016) Microstructure, mechanical and intergranular corrosion behavior of dissimilar DSS 2205 and ASS 316L shielded metal arc welds. *Transact. Indian. Inst. Met.*, **70**. DOI: https://doi.org/10.1007/s12666-016-0878-8
21. Labanowski, J. (1997) Duplex steels — new material for chemical processing industry. *Engineering and Chemical Equipment*, **2**, 3–10.
22. API 582–09: *Welding guidelines for the chemical, oil, and gas industries.*
23. Norsok M-630: *Material data sheets and element data sheets for piping.* Ed. 6. Oktober 2013.
24. Muthupandi, V., Bala Srinivasan, P., Seshadri, S.K., Sundaresan, S. (2003) Effect of weld metal chemistry and heat input on the structure and properties of duplex stainless steel welds. *Mater. Sci. and Engin. A*, **358**, 9–16.
25. Higelin, A., Manchet, S., Passot, G. et al. (2022) Heat-affected zone ferrite content control of a duplex stainless steel grade to enhance weldability. *Welding in the World*, **66**, 1503–1519. DOI: https://doi.org/10.1007/s40194-022-01326-0
26. Kurintsev, S.V. (2020) Analysis of influence of welding method on phase composition and internal stresses of welded joints of austenitic and duplex steels. *Science Intensive Technologies in Mechanical Engineering*, **3**, 3–11.
27. Krasnorutskyi, S., Keil. D., Shmigalla, S. et al. (2012) Metallurgical investigations on electron beam welded duplex stainless steel. *Welding in the World*, **56**, 34–40.
28. Geipl, H. (1989) MAGM-Schweissen von Korrosions bestaendigen Duplex-Stahlen 22Cr5(9)Ni3Mo. Entfluss von schutzgas-und werfahrenvarianten. *Linde – Sonderdruck*, **146**.
29. Hrivňák, I. (2002) Duplex stainless steels and their welding. *SVÁRANIE-SVAROVANÍ*, **3–4**, 49–54.
30. Bonnefois, B. *Comportement des assemblages soudés en aciers inoxydables avec addition d´azote.* EUR 159961.
31. Maksymov, S.Yu., Radzievska, A.A., Vasyliev, D.V., Fadeeva, G.V. (2021) Problems of wet underwater welding of duplex steels. *The Paton Welding J.,* **9**, 9–14. DOI: https://doi.org/10.37434/tpwj2021.09.02
32. Prokop-Strzelczynska, K., Rogalski, G. (2016) Cold cracking susceptibility of joints made of ferritic austenitic duplex steel 2205 during underwater welding. *Biuletyn Instytutu Spawalnictwa w Gliwicach,* 16(**2**), 35–42. DOI: https://doi.org/10.17729/ebis.2016.2/4
33. Hu, Y., Shi, Y., Shen, X., Wang, Zh. (2018) Microstructure evolution and selective corrosion resistance in underwater multi-pass 2101 duplex stainless steel welding joints. *Metallurgical and Materials Transact. A*., **5**.
34. Hu, Y., Shi, Y., Sun, K. et al. (2018) Microstructure and mechanical properties of underwater hyperbaric FCA-welded duplex stainless steel joints. *J. Materials Proc. Technology*, **261**, 31–38.
35. Hu, Y., Shi, Y., Shen, X., Wang, Z. (2017) Microstructure, pitting corrosion resistance and impact toughness of duplex stainless steel underwater dry hyperbaric flux-cored arc welds. *Materials*, **10**, 1–18. DOI: https://doi.org/10.3390/ma10121443
36. Hu,Y., Shi, Y., Sun, K., Shen, X. (2019) Microstructure evolution and mechanical performance of underwater local dry welded DSS metals at various simulated water depths. *J. Materials Proc. Technology*, **264**, 366–376.
37. Yi, Y., Shi, Y., Lin, S. et al. (2017) Research on the weld forming and microstructure of underwater wet flux-cored arc welding (FCAW) duplex stainless steel. *J. of Harbin Engineering University*, 38(**6**), 956–969.
38. Kun, Sun, Min, Zeng, Yonghua, SHI et al. (2018) Microstructure and corrosion behavior of S32101 stainless steel underwater dry and wet welded joints. *J. Materials Proc. Technology*, **256**, 190–201.

ORCID

S.Yu. Maksymov: 0000-0002-5788-0753

CONFLICT OF INTEREST

The Authors declare no conflict of interest

CORRESPONDING AUTHOR

S.Yu. Maksymov
E.O. Paton Electric Welding Institute of the NASU
11 Kazymyr Malevych Str., 03150, Kyiv, Ukraine.
E-mail: maksimov@paton.kiev.ua

SUGGESTED CITATION

S.Yu. Maksymov, G.V. Fadeeva, A.A. Radzievska, D.V. Vasyliev (2023) Features of welding duplex stainless steels in wet underwater welding in comparison with welding in air (Review). *The Paton Welding J.*, **10**, 10–17.

JOURNAL HOME PAGE

https://patonpublishinghouse.com/eng/journals/tpwj

Received: 12.07.2023
Accepted: 14.11.2023

DOI: https://doi.org/10.37434/tpwj2023.10.03

INFLUENCE OF THERMAL CONTACTS ON HEATING ALUMINIUM PLATES UNDER NON-STATIONARY HEATING CONDITIONS, USING THE SHS-PROCESS

A.I. Ustinov, M.V. Kulinich, S.G. Kosintsev

E.O. Paton Electric Welding Institute of the NASU
11 Kazymyr Malevych Str., 03150, Kyiv, Ukraine

ABSTRACT

The temperature of the heater, which can be used to join a plate of limited dimensions, to a shell of unlimited dimensions by brazing, in the general case is determined by melting temperature of the filler metal and characteristics of heat transfer in the plate contact zone. In the case of a low heat transfer in the contact zone, its heating to the temperature required for brazing is complicated, as a result of spreading of the heat coming into the shell. The work is an experimental study of the impact of imperfect thermal contacts between the aluminium plates on their heating, using a flat heater, which is in contact with one of the plates. It turned out that the force of pressing the contacting plates to each other has a greater effect on heat transfer in the contact zone than the surface roughness. Here, the value of the coefficient of effective heat transfer changes jumplike during heating of the plates, which is associated with microplastic deformation of their surface layers under the impact of a compressive load. A computational-experimental method of self-consistent determination of the values of the coefficient of effective heat transfer for different temperatures was proposed, which is based on comparison of experimentally measured and calculated thermograms of plate heating.

KEYWORDS: temperature fields, non-stationary heating process, thermal contacts, brazing, multilayer foils

INTRODUCTION

Repair of large-sized shell structures can be performed by applying a patch which is joined during brazing using local heating of the joint zone by a flat heater which is in contact with the coverplate (Figure 1). It is assumed that the heater parameters (temperature, weight, etc.) should ensure filler metal melting in the plate joining zone without surface melting of the coverplate which is in contact with it [1].

The respective brazing scheme under the conditions of stationary heating of the joining zone by a heater with constant temperature was analyzed in works [2, 3] for piping repair in space. When solving this problem, it was assumed that thermal contacts between elements of the system, consisting of a pipe, coverplate, filler metal and heater, are ideal. It is shown that such a brazing scheme can ensure local heating of the joining zone up to the temperature of filler metal melting, provided that the heater temperature exceeds a certain limit quantity, the actual value of which depends on the weight and dimensional parameters of the assembly. Application of such a brazing scheme, however, envisages use of high-capacity power sources to prevent heat spreading through the pipe during heating.

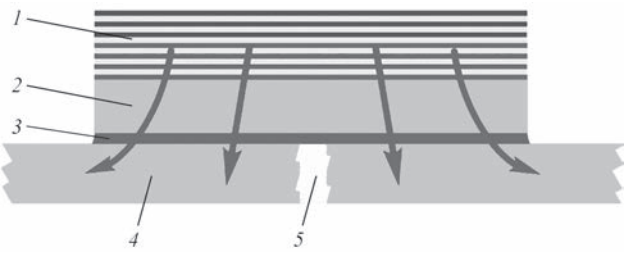

Figure 1. Scheme of shell repair by brazing at local heating of the joining zone by a flat heater (under non-stationary conditions): *1* — heater; *2* — coverplate; *3* — filler metal; *4* — shell; *5* — hole (arrows show thermal energy propagation (conditionally))

High-capacity heat sources used for brazing can be replaced by a chemical heat source based on multilayer foil (MF), which consists of highly-reactive elements, such as nickel and aluminium. At initiation of the reaction of self-propagating high-temperature synthesis (SHS) in such a foil, formation of the intermetallic compound is accompanied by intensive heat evolution, which ensures the heater heating to adiabatic temperature of SHS reaction in a short period of time. In case of application of multilayer Ni/Al foils the heater can reach the temperature of ~1800 K in fractions of a second [4].

The heater power is obviously proportional to the weight of the reaction material in multilayer foil, as well as its thickness. Changing MF weight (or thickness) in the heater allows ensuring the required temperature conditions for brazing on the surface of a shell of unlimited dimensions. It was found [1] that in the approximation of ideal thermal contacts there is the optimal MF thickness for realization of the brazing process. In our case, when it is necessary to ensure high power, and the heater is assembled not from one, but from several foils, thickness control becomes a problem, and it is better to proceed exactly from the total

weight of the reaction material. At heater weight below the optimal one, the filler metal melting temperature is not achieved in the joining zone. If the heater weight is greater than the optimal one, surface melting of the coverplate, which is in contact with it, can occur.

As the temperature in the joining zone is determined by the balance of heat fluxes from the heater into the coverplate and from it into the shell through the filler metal, the filler metal temperature and its melting time, in their turn, will be determined not only by thermophysical characteristics of the materials of system elements (heater, plates and filler metal), but also by the characteristics of thermal contacts between them. Unlike the material thermophysical characteristics, those of the thermal contacts are unknown a priori, and they can change in a broad range, depending on a number of factors. It is known that the resistance to propagation of the heat flux in the contact between the two flat plates, pressed to each other, is due mainly to imperfect fit of their surfaces [5, 6]. Heat exchange between the plates in vacuum at a relatively low temperature in the contact zone (below 1000 K), when heat transfer through radiation and convection can be ignored, will be chiefly determined by the area of the surface of physical contact of the plates, which depends on their surface relief.

At pressing of the plates in the points of contact, in which the load is higher than the material yield limit, a local plastic deformation of the protrusions will take place, leading to increase of the area of the plate physical contact, and, hence, to reduction of the resistance to heat flux propagation.

Thus, heat conductivity in the contact zone depends not only on contacting surfaces roughness, but also on the force of their pressing together and mechanical properties of the contacting materials. Moreover, as the material yield limit in the general case depends on temperature, a change in the thermal contact characteristics at heating is to be anticipated, even at a constant compressive force.

In the work, the change of temperature in the plates during their non-stationary heating, depending on surface roughness and the force of their pressing together, was studied, in the case of a model system, which consists of a flat heater, contacting AMg6 plates.

EXPERIMENTAL PROCEDURE

The scheme of temperature measurement in AMg6 plates during heating is shown in Figure 2.

Plates from AMg6 aluminium alloy of 50×50×5 mm size were cut out of a sheet. After that their contact surfaces were ground to ensure thermal contact over the entire plane. They were placed into a clamping device one above the other. Installed above the upper plate was a heater — a Ni/Al MF packet, which is in contact with it over the entire plane. In order to study

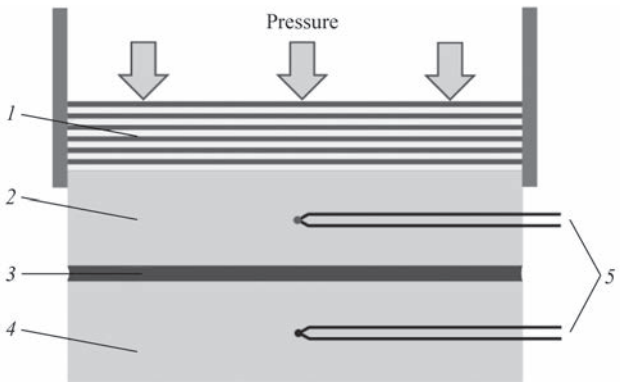

Figure 2. Scheme of the assembly used for experimental study of temperature fields during brazing of AMg6 aluminium plates (*2*, *4*) separated by filler metal interlayer (*3*), at heating with a heater from multilayer foils (*1*), which is in contact with the coverplate (*2*); *5* — thermocouples inserted into plates

the influence of roughness on heat transfer in the contact zone, plates were prepared, the contact surfaces of which were pre-treated with sand paper to achieve roughness indices of 0.3 and 2.5 μm, which were determined by the used paper grit. Pressing down of this assembly was provided by a spring, which was placed above the heater, and was compressed to the specified loading value, proceeding from the readings of the strain gauge, mounted under the lower plate.

To model the plate joining by brazing, a layer of Al–Si filler metal 100 μm thick was deposited by EB PVD method on the surface of the upper coverplate, which is in contact with the lower shell-plate. SHS reaction in Al/Ni MF was initiated by feeding a current pulse from a pre-charged capacitor to the nichrome spiral, which locally heated the MF in the contact area. The high velocity of SHS reaction propagation in MF (1–2 m/s) ensured fast heating of the heater to adiabatic temperature of the reaction of NiAl intermetallic synthesis. Change in the plate temperature with time was measured using KhA thermocouples with 0.15 mm wire diameter. Thermocouples in ceramic insulation were inserted into 2.5 mm diameter channels drilled in the plates so that their junctions were in the center of the plates, pressed against them. It was assumed that thermocouple inertia can be neglected for these processes. Thermocouple readings were recorded on the computer by a controller with recording frequency of 1 kHz. To reduce heat losses and convective heat exchange between the system elements, the assembly was placed into a vacuum chamber (residual pressure of ~ 0.1 Pa).

PROCEDURE OF NUMERICAL MODELING OF TEMPERATURE FIELDS

Numerical modeling of temperature fields was performed in the assumption that all the system elements (heater, AMg6 plates) have unlimited dimensions in the plate joining plane and limited dimension in the normal direction. In this case, the problem is reduced

to analysis of heat redistribution in one direction, normal to the contact plane. Accordingly, all the elements were divided into layers of final thickness Δx. It was assumed that there is no thermal energy radiation outside the system, and, thus, boundary conditions of the second kind will be satisfied for extreme layers (0-th and N_{max}): $T_0 = T_1$, $T_{N_{max}} = T_{N_{max}-1}$, where N_{max} is the maximal layer number: $N_{max} = \frac{L_0}{\Delta x} + \frac{L_1}{\Delta x} + \frac{L_2}{\Delta x} + 2$, where L_0 is the heater thickness; L_1 is the coverplate thickness; L_2 is the shell thickness. The interlayer based on the filler metal was considered as one layer.

In order to determine the temperature in each layer, it is necessary to solve the equation of heat conductivity, allowing for the thermophysical properties of the layer materials:

$$\frac{\partial T}{\partial t} = a \frac{\partial^2 T}{\partial x^2}, \quad (1)$$

where a is the thermal diffusivity coefficient (m^2/s) for the layer material.

Equation (1) has a solution for all the system layers of width Δx:

$$T_i = T_i^{old} + a_i \frac{T_{i+1}^{old} - 2T_i^{old} + T_{i-1}^{old}}{\Delta x^2} dt, \quad (2)$$

where T_i^{old} is the initial temperature of the i-th layer, and T_i is its temperature after time of dt seconds.

This relationship is valid for all the layers, except those, which belong to different system elements. In order to calculate the boundary layer temperature, it was taken that the heat flux is proportional to temperature difference in boundary layers i and i+1, heat transfer between which is characterized by "effective heat transfer coefficient" $\mu_{i,\,i+1}$ in keeping with the following relationship

$$J_{i,i+1} = \mu_{i,i+1}\left(T_{i+1} - T_i\right), \quad (3)$$

where $J_{i,\,i+1}$ is the heat flux between i and i+1 layers, the temperatures of which are T_i and T_{i+1}, respectively.

In the case of an ideal thermal contact between i and i+1 layers, belonging to different system elements with heat conductivity coefficients of their materials k_i, k_{i+1} and thicknesses h_i and h_{i+1}, respectively, the effective heat transfer coefficient was determined as

$$\mu_{i,i+1} = \frac{2k_i k_{i+1}}{k_i h_{i+1} + k_{i+1} h_i}. \quad (4)$$

Therefore, the temperatures of the adjacent layers were determined using systems of equations, including equations of types (2) and (3) for heat fluxes between the boundary and adjacent to them layers [7], and heat transfer coefficients were assigned a priori for imperfect contacts, or they were calculated by formula (4) in the case of ideal contacts. Numerical realization of this algorithm allows calculation of temperature distribution by system thickness for any moment of time t or temperature change in the set point, depending on time. The start of timing was taken to be the moment of completion of SHS reaction in MF, when the heater temperature reaches the adiabatic temperature of high-temperature synthesis of NiAl intermetallic. Considering that the speed of SHS reaction front propagation is equal to ~1–2 m/s, the heat exchange between the heater and the plate was ignored. It was also considered that the thermophysical characteristics of system elements (thermal diffusivity and heat capacity of heater and plate materials) are independent of temperature. In the presence of filler metal between the plates, it was taken into account as a separate interlayer with its own thermophysical properties, which were determined according to its chemical composition. The peculiarities of taking into account the layer of filler metal between the plates are described in detail in [8].

INVESTIGATIONS RESULTS AND THEIR DISCUSSION

Figure 3, *a* shows the thermograms of temperature change in plates with different roughness. Compression in the joining zone was equal to 60 kPa. One can see that the coverplate temperature abruptly and non-monotonically rises after initiation of SHS reaction in MF. Although the heater quickly reaches the temperature of 1700 K and higher, no surface melting of the plates which are in contact with it was observed. This is the result of high heat conductivity of aluminium alloys, due to which the thermal energy is removed so quickly from the contact zone that no local overheating above the melting temperature occurs in it. Such melting can be observed only at considerable overheating of the assembly, when the melting temperature is reached for the plate as a whole, and not only in the contact zone. Heating of the other plate ("shell") occurs with a certain delay, the "lag" in temperature rise in it becoming greater with greater roughness of the plate contact surfaces. It is obvious that such a lag is due to poorer heat exchange in the plate contact zone as a result of reduction of the effective thermal contact area.

Pressure increase at unchanged roughness of plate contact surfaces (Figure 3, *b*) leads to lowering of coverplate heating rate and increase of shell heating rate, i.e. to reduction of temperature difference between the coverplate and the shell at each moment of time, which is indicative of higher heat exchange in the contact between them. Note that the nature of the coverplate temperature change becomes qualitatively different with increase of pressing force: at smaller pressing force its temperature first increases abrupt-

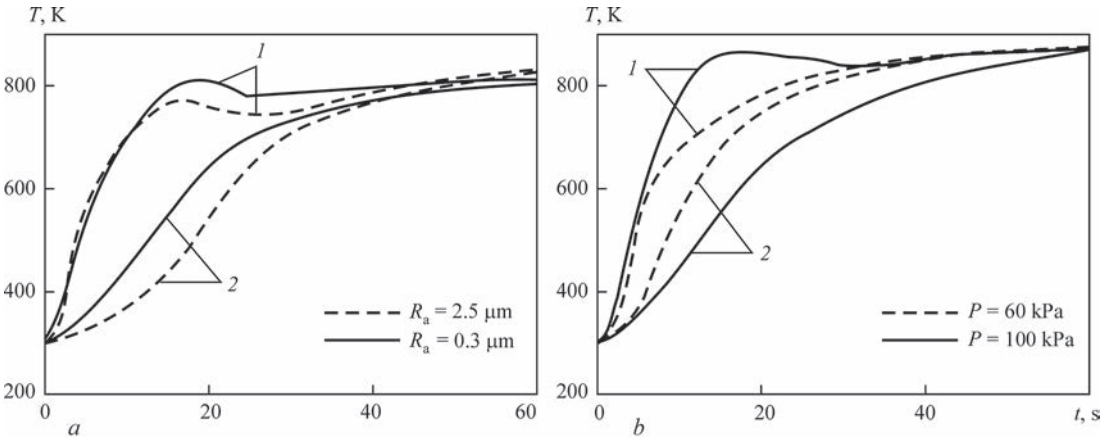

Figure 3. Influence of plate surface roughness at constant pressure of 60 kPa (*a*) and at constant roughness R_a = 0.3 μm (*b*) on temperature change during their heating: *1* — coverplate; *2* — "shell"-plate

ly and then somewhat decreases; at greater force the change in its temperature is of a more monotonic nature. Some, relatively minor differences in the shape of the curves for P = 60 kPa, R_a = 0.3 μm are related to errors of heater dosing and deviations of the foil chemical composition from the average value.

As the non-monotonic shape of the thermogram of upper plate heating is observed under the condition of weaker heat transfer in the contact between the plates, we assumed that at the initial moment of heating the applied pressure is insufficient to achieve the best contact between the plates. When the plate temperature rises, at the same pressure, microplastic deformation of their surface layers is achieved, which improves the contact surfaces fit, and, hence, also the heat exchange.

Comparing the time dependencies of system element temperature one can see (Figure 3, *b*) that the bends on the coverplate and shell thermograms, which point to a decrease of the heating rate of the first and increase of the heating rate of the second, coincide in time, which is an indication of improvement of thermal contact between the plates at this moment. Proceeding from the obtained experimental results, we came to the conclusion that at heating of AMg6 plates by MF, which is in contact with the coverplate, with superposition of constant pressing in the range of 60–100 kPa, conditions are in place, which are necessary for material plastic deformation in the contact zone.

In order to test this assumption, experiments were conducted on heating AMg6 plates, separated by tungsten threads 0.3 mm thick to simulate "poor thermal contact" in the butt at the start of heating (Figure 4, *a*). Obtained experimental thermograms are given in Figure 4, *b*. One can see that first the coverplate is heated at a high rate up to a certain moment of time. After that its temperature rise slows down and even its slight lowering occurs. At the same moment of time, a bend is observed on the shell-plate thermogram, which indicates an increase of its heating rate.

Examination of plate surfaces after completion of the thermal cycle showed (Figure 5) the presence on them of imprints from thin tungsten threads, which separated these surfaces before the start of heating. These imprints were not observed under the conditions of compression of a similar assembly with the same force, but without heating.

Appearance of imprints indicates that at plate heating at a constant load the conditions of plate material plastic deformation are achieved due to lowering of its yield limit with temperature rise. Indeed, investi-

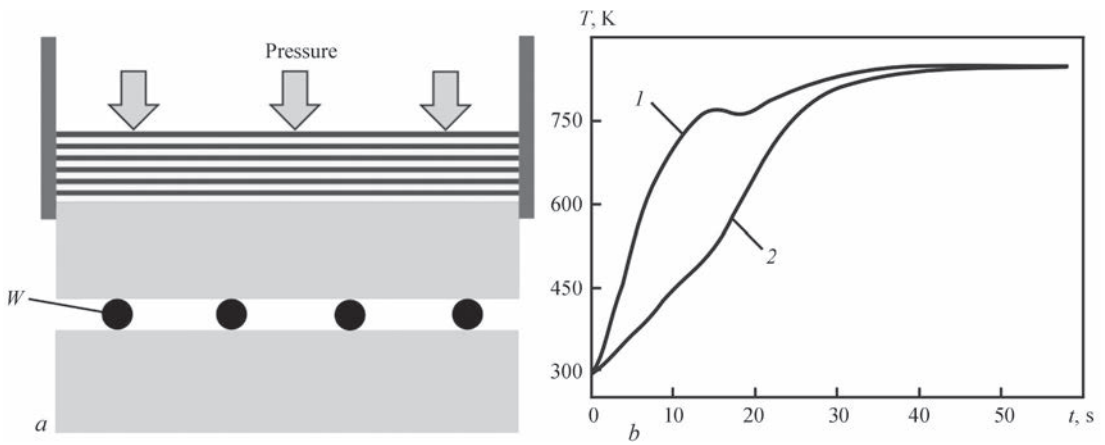

Figure 4. Scheme of heating of plates (*a*), separated by tungsten threads (W) and experimental thermogram of heating of coverplate (*1*) and "shell" (*2*) plates separated by thin tungsten threads at constant pressure of 100 kPa (*b*)

Figure 5. Surfaces of AMg6 alloy plates after thermal cycle of heating under the conditions of their compression with 100 kPa force

gations of the dependence of yield limit on temperature in aluminium alloys in works [9, 10] showed that the yield limit can decrease several times at heating, compared to this value at room temperature.

Thus, the heat transfer parameters in the zone of plate contact at their heating under constant loading can change, as a result of achievement of the conditions of plastic deformation of plate material at their heating. It leads to an essential decrease of the heating rate of the coverplate, which is in contact with the heater, and increase of the shell heating rate. In some cases, increase of the heat transfer coefficient on the boundary of the two plates during their heating may lead to appearance of a "shelf" on the coverplate thermogram, similar to the one observed at material melting. This effect is, probably, due to transition from elastic deformation of material of the plate surface layers to their plastic yield under the impact of the applied pressure at the temperature, at which the plate material yield limit decreases to the level corresponding to the pressing force.

It is clear that if the contacting surface material has a lower yield limit, than does the AMg6 alloy, the temperature of such a transition will be even lower. To test this assumption, investigation of AMg6 plate heating was conducted, when one of the contact surfaces of the coverplate was coated by multilayer filler metal based on AlSi. It turned out (Figure 6) that the temperature of the change in the slope of the curves in the thermograms is lower than at heating of the plates without the filler metal. Peak values of temperature turned out to be lower than in the previous experiments (Figure 3, *a*, *b*), which is related to errors in heater mass dosing. Considering that melting temperature of AlSi filler metal is equal to ~850 K, when the temperature of multilayer foil of a eutectic composition becomes close to this temperature, it undergoes structural changes, affecting mainly, the filler metal mechanical behaviour, namely its deformational behaviour under the pressing force. It results in the yield limit of multilayer filler metal decreasing at heating, which may have an essential influence on the characteristics of thermal contact between the plates [11].

MATHEMATICAL MODELING OF TEMPERATURE FIELDS

Mathematical modeling of the temperature fields was performed with variation of the coefficients of effective heat transfer in the contacts between the heater and coverplate ($\mu_{h,pl}$) and between the plates ($\mu_{pl,pl}$). Dependence (Figure 6, *a*, theor. 1) was obtained in the assumption that during heating the coefficients of heat transfer in the contacts remain constant ($\mu_{pl,pl}$ = $= 1 \cdot 10^5$ W/(m^2·K); $\mu_{h,pl} = 1 \cdot 10^4$ W/(m^2·K)), and dependence (Figure 6, *b*, theor. 2) — in the assumption that the coefficient of heat transfer in the plate contact zone at the temperature of 700 K rises from $\mu_{pl,pl} = 5 \cdot 10^4$ to $6.6 \cdot 10^5$ W/(m^2·K) at a constant value of the coefficient of effective heat transfer in the zone of contact of the heater and coverplate ($\mu_{pl,pl} = 9 \cdot 10^3$ W/(m^2·K).

It turned out that the calculated temperature changes at plate heating, provided that the heat transfer coefficients remain constant (Figure 6, *a*, curve theor. 1), are in good agreement at the initial stages only with experimental thermograms, obtained for a plate, which is in contact with the heater. At later stages of this process, a significant discrepancy between calculation and experiment is observed.

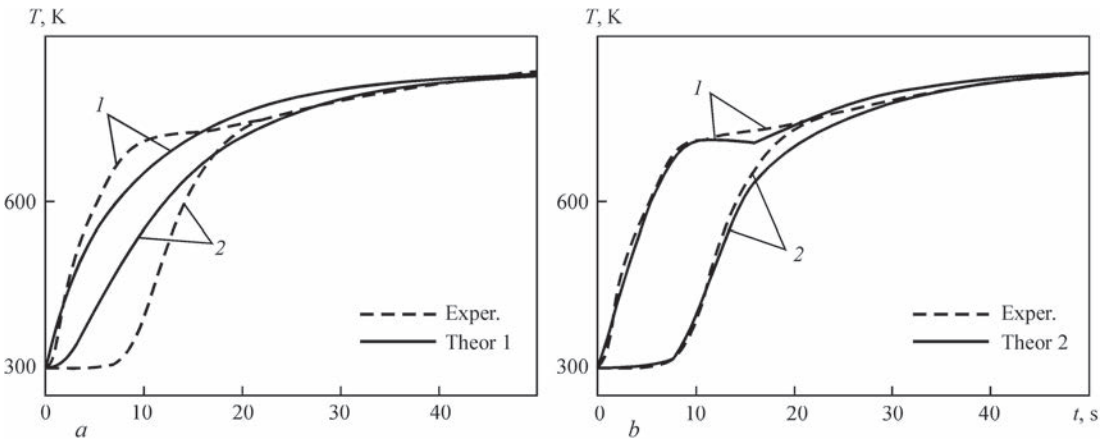

Figure 6. Temperature dependence in an assembly of AMg6 plates, separated by a filler metal interlayer, beginning from the time from the moment of SHS reaction passing in the heater under the conditions of 100 kPa constant pressure for coverplate (*1*) and "shell"-plate (*2*). Dashed lines are the results of experimental measurements; solid lines are the results of modeling at constant (*a*) and variable (*b*) coefficients of effective heat transfer

Modeling of the assembly heating process under the condition that a change in the coefficient of heat transfer in the contact between the plates occurs at achievement of a certain temperature of the coverplate (700 K), provided a much better agreement of the calculated and experimental thermograms (Figure 6, *b*, curve theor. 2).

Therefore, in order to predict the conditions of filler metal melting in an "open" system (joining a coverplate to a large-sized shell) using a heater with a set amount of heat, it is necessary to know not only the thermophysical parameters of materials (heat capacity, thermal conductivity, etc.) and thicknesses of system elements, but also heat transfer coefficients in the contacts between them. Obtained results show that these coefficients are not constant at temperature change, which essentially complicates assessment of heater parameters. Application of experimental thermograms and capabilities of numerical modeling of heating of plates of limited dimensions ("laboratory conditions"), allow determination of heat transfer coefficients in the contacts and the temperature of their change (which corresponds to the yield limit of plate material or filler metal at a certain load) by variation of these parameters to ensure the best agreement of the experimental and calculated values of plate temperature during their heating. Parameters of thermal contact derived during such a self-consistent calculation, can be used in further modeling of the process of heating of the joining zone on the surface of a shell of "unlimited" dimensions (under the conditions of the same roughness of the contacting surfaces and their pressing force), in order to determine the heating parameters ensuring the temperature conditions required for brazing.

CONCLUSIONS

It was found that the effectiveness of heat transfer in the zone of contact of AMg6 plates during their heating by a flat heater, which is in contact with one of them, depends both on the roughness of contacting surfaces, and on the pressing force. The heat exchange effectiveness becomes higher at reduction of the contacting surface roughness in the range from 2.5 to 0.3 μm and at pressure increase from 60 to 100 kPa. Improvement of heat exchange parameters at pressure increase during plate heating is associated with microplastic deformation of the plate surface layers, leading to increase of the area of their physical contact.

It is shown that comparison of plate heating thermograms obtained experimentally and calculated by numerical modeling allows determination of the coefficients of effective heat transfer in the zones of contact of the heater and coverplate and of the plates, as well as the temperature (temperature range) of transition from imperfect contact between AMg6 plates to their ideal contact under the conditions of non-stationary heating of the system at constantly applied pressure.

REFERENCES

1. Kulinich, M.V., Zaporozhets, T.V., Gusak, A.M., Ustinov, A.I. (2019) Calculation of thermal fields during joining aluminium plates through interlayers at local heating of the joint zone. *The Paton Welding J.,* **4**, 11–18. DOI: http://dx.doi.org/10.15407/tpwj2019.04.03
2. Vasenin, Yu.L., Zagrebelny, A.A., Zelnichenko, A.Y. et al. (2001) Modelling of thermal process in piping repair in space. *The Paton Welding J.,* **4**, 18–23.
3. Krivtsun, I.V., Kvasnytskyi, V.V., Maksymov, S.Yu., Iermolaev, G.V. (2017) *Special methods of welding*: Manual. Ed. by B.E. Paton. Mykolaiv, NUK [in Ukrainian].
4. Weihs, T., Barmak, K., Coffey, K. (2014) Fabrication and characterization of reactive multilayer films and foils. Metallic films for electronic, optical and magnetic applications: Structure. *Processing and Properties*, **40**, 160–243.
5. Popov, V.M. (1971) *Heat exchange in the zone of detachable and permanent joints.* Moscow, Energiya [in Russian].
6. Lykov, A.V. (1978) *Reference book on heat-, mass exchange*. Moscow, Energiya [in Russian].
7. Bezpalchuk, V.M., Zaporozhets, T.V., Kravchuk,, M.V. et al. (2015) Calculation of thermal fields in multiphase 3D system under nonstationary conditions of its heating. *Visnyk Cherkaskogo Un-tu,* 349(**16**), 38–49 [in Ukrainian].
8. Kulinich, M.V., Bezpalchuk, V.N., Kosintsev, S.G. et al. (2018) Calculation-experimental investigation of thermal fields in the process of nonstationary soldering. *The Paton Welding J.,* **1**, 14–19. DOI: http://doi.org/10.15407/tpwj2018.01.03
9. Summers, P.T., Chen, Y., Rippe, C.M. et al. (2015) Overview of aluminum alloy mechanical properties during and after fires. *Fire Science Reviews*, 4(**1**), 1–36.
10. Su, M.-N., Young, B. (2017) Mechanical properties of high strength aluminium alloy at elevated temperatures. *Ce/papers*, 1(**2–3**), 2831–2839.
11. Ustinov, A.I., Melnychenko, T.V., Demchenkov, S.A. (2021) Structural mechanism of plastic deformation of Al/a–Si multilayer foils at heating under load. *Mater. Sci. & Engin. AA,* **810**, 141030.

ORCID

A.I. Ustinov: 0000-0002-8855-3499,
M.V. Kulinich: 0000-0002-3023-6677,
S.G. Kosintsev: 0000-0003-4752-076X

CONFLICT OF INTEREST

The Authors declare no conflict of interest

CORRESPONDING AUTHOR

A.I. Ustinov
E.O. Paton Electric Welding Institute of the NASU
11 Kazymyr Malevych Str., 03150, Kyiv, Ukraine.
E-mail: ustinov3g@gmail.com

SUGGESTED CITATION

A.I. Ustinov, M.V. Kulinich, S.G. Kosintsev (2023) Influence of thermal contacts on heating aluminium plates under non-stationary heating conditions, using the SHS-process. *The Paton Welding J*., **10**, 18–23.

JOURNAL HOME PAGE

https://patonpublishinghouse.com/eng/journals/tpwj

Received: 25.07.2023
Accepted: 14.11.2023

DOI: https://doi.org/10.37434/tpwj2023.10.04

STUDYING THE IMPACT OF DURATION OF TECHNOCHEMICAL SYNTHESIS OF NANOSTRUCTURE (Fe, Ti)$_3$Al POWDER ON CHARACTERISTICS OF PLASMA COATINGS

O.P. Gryshchenko[1], N.V. Vihilianska[1], O.M. Burlachenko[1], C. Senderowski[2], V.F. Gorban[3]

[1]E.O. Paton Electric Welding Institute of the NASU
11 Kazymyr Malevych Str., 03150, Kyiv, Ukraine
[2]Warsaw University of Technology
plac Politechniki 1, 00-661 Warszawa, Poland
[3]Institute of Problems of Materials Science I.M. Fransevich of the NASU
3 Academician Krzhizhanovsky, 03142, Kyiv Ukraine

ABSTRACT

The impact of duration of high-energy processing of the mixture of 60.8Fe + 39.2TiAl powders (wt.%) on structure, phase composition and mechanical characteristics of plasma intermetallic (Fe,Ti)$_3$Al coatings was studied. As powders, for plasma spraying powders of (Fe,Ti)$_3$Al intermetallic were used, which were produced by the method of mechanochemical synthesis (MChS) in a high-energy mill during 3 and 5 h. As a result of plasma spraying, coatings with a nanocrystalline structure with the size of crystallites of 60 and 45 nm are formed, respectively. It was shown that during spraying of MChS-powder, produced during 5 h, thin-lamellar coatings with a maximum thickness of lamellae of 23 μm are formed, whereas in the case of spraying MChS-powder produced during 3 h, the thickness of lamellae reaches 42 μm. At the same time, in the case of spraying MChS powder, produced during 5 h, more dense coatings are formed, the porosity of which is reduced by 2.3 % compared to the coating from MChS-powder, produced during 3 h. It was established that mechanical characteristics (hardness and modulus of elasticity) of a plasma coating were increased when using a powder produced by processing during 5 h. This allows predicting higher wear resistance of these coatings, operating in the conditions of wear unlike the case of spraying MChS-powder, produced during 3 h.

KEYWORDS: iron aluminides, mechanochemical synthesis, plasma spraying, nanostructural coatings, size of crystallites, mechanical characteristics

INTRODUCTION

One of the tasks of surface engineering at the present stage of the technology development is the development of protective coatings that provide protection of parts and units of equipment in the conditions of elevated operating temperatures and mechanical stresses and influence of aggressive and abrasive environments. Intermetallic based coatings can be attributed to perspective ones, in particular, those on the base of iron (Fe_3A1, FeAl) aluminides. These intemetallics are characterized by relatively low specific mass (5.51–6.65 g/cm^3), wear resistance, resistance to oxidative and sulfidating media at 1000 °C and higher. The areas of their potential application include heating elements, furnace reinforcement, heat exchanger pipes, sintered porous "gas–metal" filters, parts of valve systems of cars, components of installations operating with salt melts [1]. However, the practical use of iron aluminides is limited due to their tendency to hydrogen brittleness and low creep at temperatures of > 500 °C [2]. An improvement in mechanical characteristics of iron aluminides is achieved by their alloying (B, Si, Cr, Ti etc.), as well as by reduction in the grain size [3–5]. An increase in ductility during alloying can be achieved as a result of a decrease in the covalent bond component, creation of a favourable dislocation structure with a higher dislocation mobility, providing the action of more favourable sliding systems, change in crystalline or phase composition and structural state. The use of titanium as an alloying element helps to raise the temperature of phase transitions, increase the yield strength and improves tribotechnical properties of FeAl intermetallic [6].

To spray coatings based on iron aluminides, thermal spraying methods, namely high-velocity oxygen fuel (HVOF), plasma, electric arc and detonation spraying [7–10] are used. The use of powders produced by the method of mechanochemical synthesis (MChS) as sprayed materials allows forming coatings, which are homogeneous as to their chemical composition and have a nanocrystalline structure.

The aim of this work is studying the structure, phase composition and mechanical properties of plasma coatings when spraying MChS-powders of (Fe, Ti)$_3$A1 produced during different time of processing.

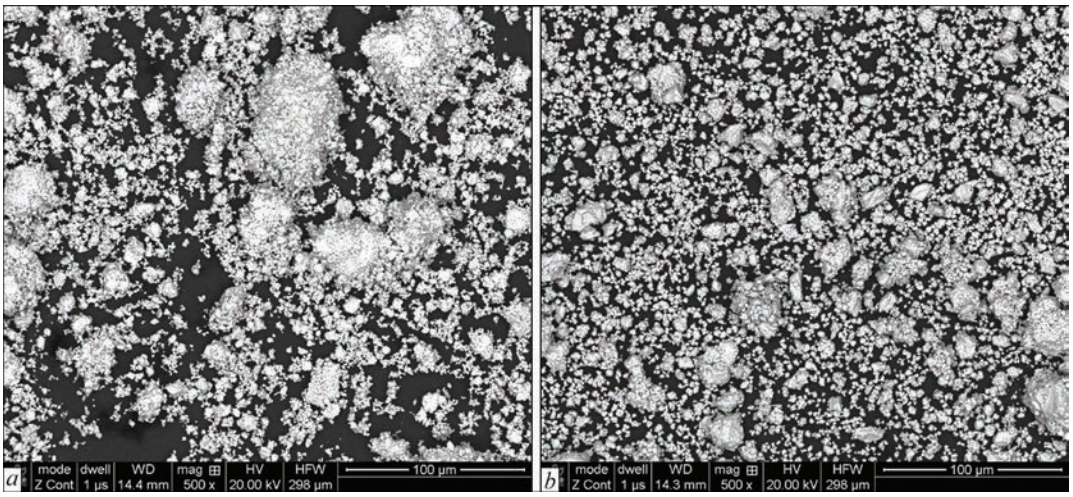

Figure 1. Appearance of powders produced by the MChS method of a mixture of iron and TiAl alloy powders during: *a* — 3; *b* — 5 h

Table 1. Characteristics of MChS (Fe, Ti)$_3$A1 powders for plasma spraying

Mixture components, wt.%	Processing time τ, h	Phase composition	Size of crystallites, nm	Particle size, μm		
				D_{10}	D_{50}	D_{90}
60.8Fe–39.2TiAl	3	(Fe, Ti)$_3$Al	25	6	17	41
	5		10	3	9	30

MATERIALS AND RESEARCH PROCEDURES

As materials for spraying, intermetallic nanostructure (Fe, Ti)$_3$A1 powders were used, produced by the method of mechanochemical synthesis of mixtures of iron and Ti37.5Al alloy powders. The MChS process was carried out in the planetary mill Activator 2SL during the processing time of 3 and 5 h. As was established in previous studies [11], after 3 h of processing, in the MChS product, an intermetallic (Fe, Ti)$_3$Al phase with crystallites of 25 nm is formed, and with an increase in the processing time to 5 h, the size of crystallites decreases to 10 nm and the size of powder particles is somewhat reduced. The appearance of powder particles after MChS is shown in Figure 1, the characteristics of powders is given in Table 1.

For the use of these powders, in the technology of plasma spraying, their conglomeration by mixing the resulting MChS products with a 5 % polyvinyl alcohol solution in water was carried out until producing a homogeneous suspension. The resulting suspension was dried with the subsequent wiping through a sieve and selecting particles of 40–80 μm.

Plasma spraying of coatings was carried out in the UPU-8M installation using the following parameters: $I = 500$ A, $U = 40$ V, $Q_{Ar+N_2} = 25$ l/min, spraying distance — 120 mm. Preliminary investigations [9] showed the feasibility of using the mentioned plasma spraying parameters to form a fine-lamellar dense structure of coatings based on FeAl intermetallics.

Determination of element composition of coatings by the method of scanning electron microscopy (SEM) was carried out on the basis of an analytical complex consisting of a scanning electron microscope JSM-35 CF of JEOL Company (Japan) and energy dispersion spectrometer (model INCA Energy-350 of Oxford Instruments Company, Great Britain). X-ray diffraction phase analysis (XRD) of coatings was performed using DRON-3 diffractometer in CuK_α-radiation with a graphite monochromator at a step movement of 0.1° and a time of exposure at each point of 4 s with the subsequent computer processing of the obtained digital data. The phase identification was performed using the international database ICDD PDF-2 or PDF-4. The size of crystallites in the coatings was evaluated using the Debye–Scherrer formula:

$$d = \frac{K\lambda}{\beta\cos\theta},$$

where d is the average size of coherent scattering regions (domains, crystallites), which may be smaller or equal to the grain size; K is the dimensionless particle shape factor (Scherrer constant); λ is the wavelength of X-ray radiation; β is the reflex width at half maximum (in radians and in units 2θ); θ is the diffraction angle (Bragg's angle).

Mechanical characteristics (hardness H, modulus of elasticity E) of the coatings were determined by the microidentation method with the use of the Micron-Gamma device [12]. The value of characteristics was calculated automatically according to ISO 14577-1:2002 standard.

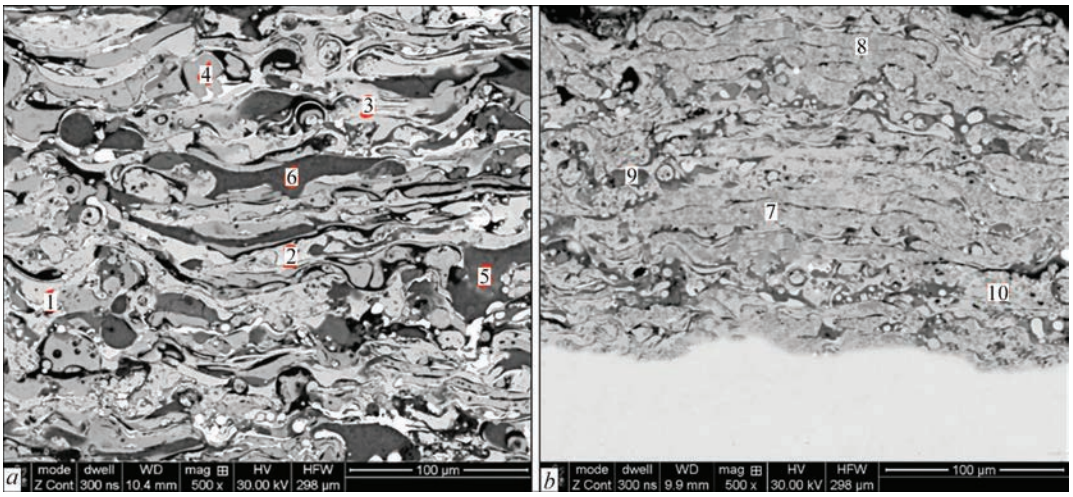

Figure 2. Microstructure of plasma coatings from nanostructural intermetallic (Fe, Ti)$_3$A1 powder, produced by the MChS method during 3 h (*a*) and 5 h (*b*)

RESEARCH RESULTS AND THEIR DISCUSSION

Metallographic analysis found that as a result of plasma spraying nanostructural powders of (Fe, Ti)$_3$Al intermetallic, the coatings with a characteristic layered structure (Figure 2, *a*, *b*) are formed. An increase in duration of mechanosynthesis of powders from 3 to 5 h leads to the formation of a structure with a smaller thickness of lamellae. In spraying MChS-powder (τ = 3 h), in the coating, lamellae of ~42 μm thick are present, whereas in spraying MChS-powder (τ = 5 h), the maximum thickness of lamellae is ~23 μm. This is associated with the presence of composite particles of up to 70 μm (Figure 1, *a*) in MChS-powder after 3 h of processing, as far as at the initial stages of the MChS-process, the process of "cold" welding of particles of initial powders with each other prevails. As the processing time increases to 5 h, between grinding and welding of particles, the equilibrium is achieved and the size of MChS-powder particles decreases.

It is noted that both types of coating are characterized by the presence of particles in the layer structure, unmolten in the plasma jet. A number of such particles in the coating of MChS-powder (τ = 3 h) is somewhat larger, which is also associated with the presence of particles of > 40 μm in the powder. This, in turn, leads to the formation of a coating with a slightly greater porosity. Thus, the porosity of the coating from MChS-powder (τ = 3 h) amounts to 6.8 ± 0.8 %, the coating from MChS-powder (τ = 5 h) is –4.5 ± 1.0 %.

Table 2. Chemical composition of plasma coatings produced by spraying intermetallic (FeTi)$_3$A1 powder

Spectra	Chemical composition, wt.%			
	Fe	Ti	Al	O
1	59.93	28.79	10.31	0.97
2	54.99	30.87	12.61	1.53
3	54.48	31.05	13.24	1.23
4	49.33	36.36	12.39	1.92
5	71.66	8.35	1.17	18.82
6	69.98	7.71	2.23	20.08
7	62.4	24.97	11.69	0.94
8	62.63	22.22	13.8	1.35
9	56.06	19.57	6.98	17.4
10	78.01	5.54	8.05	8.4

According to the analysis of the chemical composition, bright lamellae of the coatings consist of the initial components containing oxygen ~2 wt.% (Table 2). In this case, in terms of chemical composition, the regions 1–4, 7, 8 (Figure 2) are close to (Fe, Ti)$_3$Al compound. A high content of oxygen (up to 20 wt.%) in individual microvolumes is caused by the presence of oxides formed by spraying coatings as a result of interaction of powder components with a plasma jet. Such lamellae in terms of their chemical composition correspond to the iron (FeO) oxide with a small amount of titanium and aluminium (spectra 5, 6, 9, 10 — Figure 2).

By means of energy dispersive analysis it was established that the time of the MChS process of powders affects the uniformity of elements distribution over the thickness of the coating (Figures 3, 4). In the coating sprayed from MChS-powder (τ = 3 h), the distribution of initial components is non-uniform. Here, oxygen is distributed in the form of interlayers between the metal lamellae (Figure 3). An increase in the time of MChS to 5 h allowed producing a coating with a more uniform distribution of both initial elements as well as oxygen over the thickness of the coating (Figure 4). This difference in the distribution of elements over the thickness of the coating is obviously associated with the distribution of elements in MChS-powders. When conducting the MChS process during 5 h, smaller particles are formed and the distribution of elements in the powder particles is averaged.

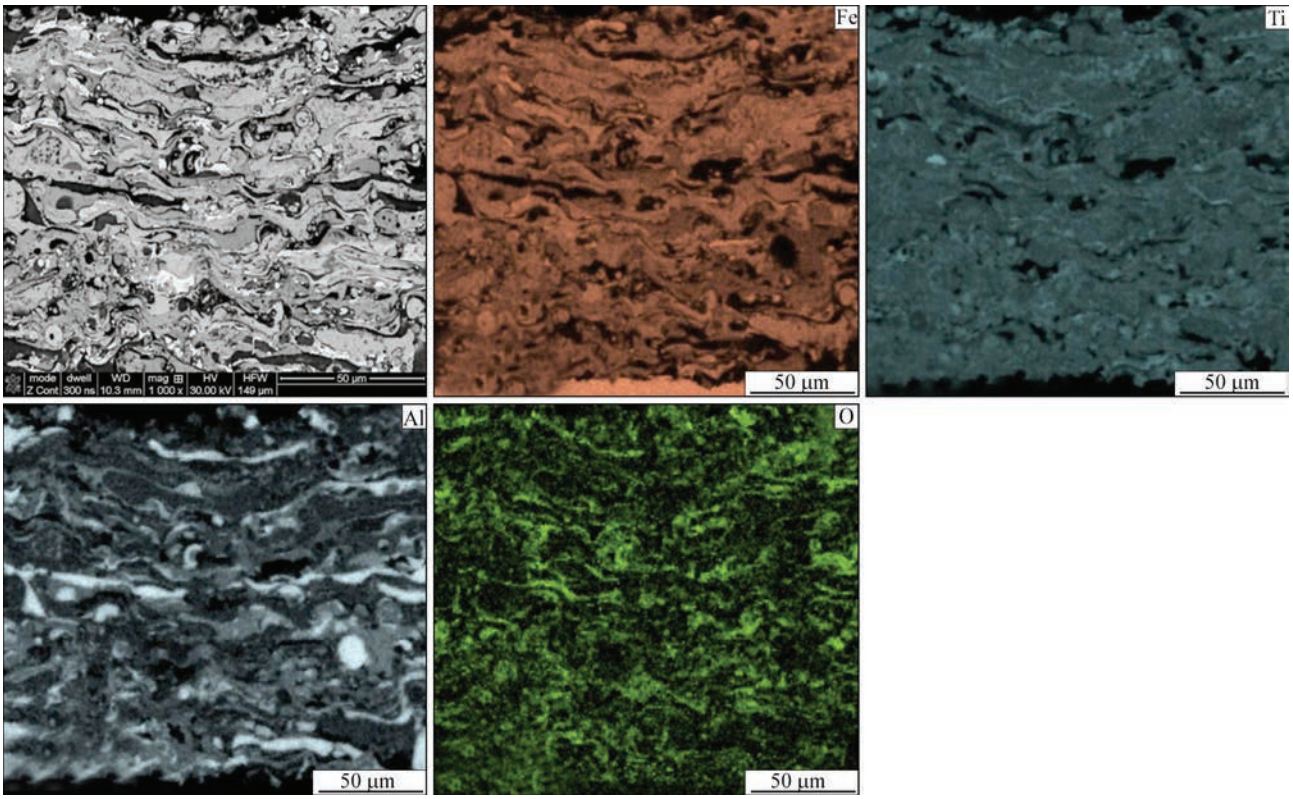

Figure 3. Distribution of elements in the plasma coating from intermetallic $(Fe, Ti)_3A1$ powder, produced by the MChS method during 3 h

As to their phase composition, the coatings do not differ significantly and in both cases the main phase in the coatings is $(Fe, Ti)_3Al$ intermetallic (Figure 5). Except of the main intermetallic phase, in the coatings also the lower FeO oxide is identified, the appearance of which is associated with the interaction of iron in the plasma jet with oxygen of the environment. This is consistent with the results of chemical analysis of the

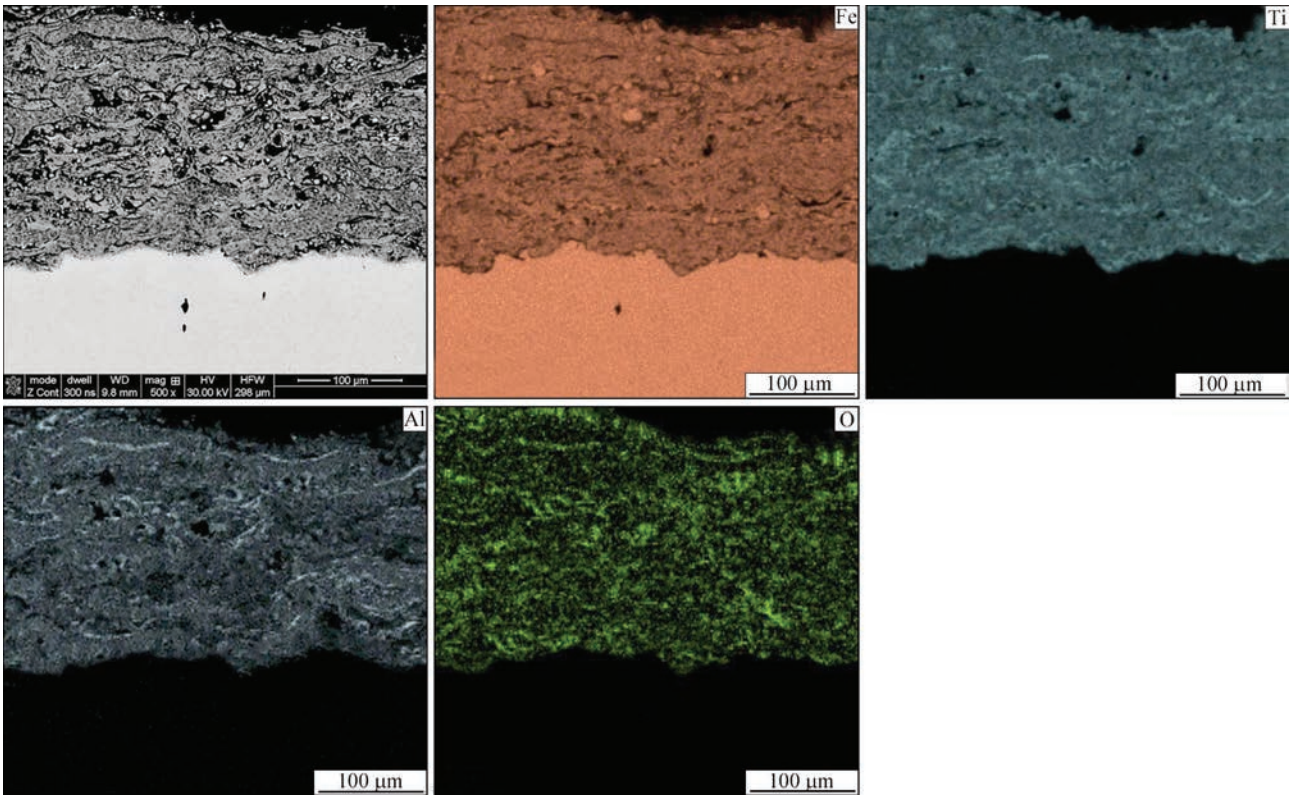

Figure 4. Distribution of elements in the plasma coating from intermetallic $(Fe, Ti)_3Al$ powder, produced by the MChS method during 5 h

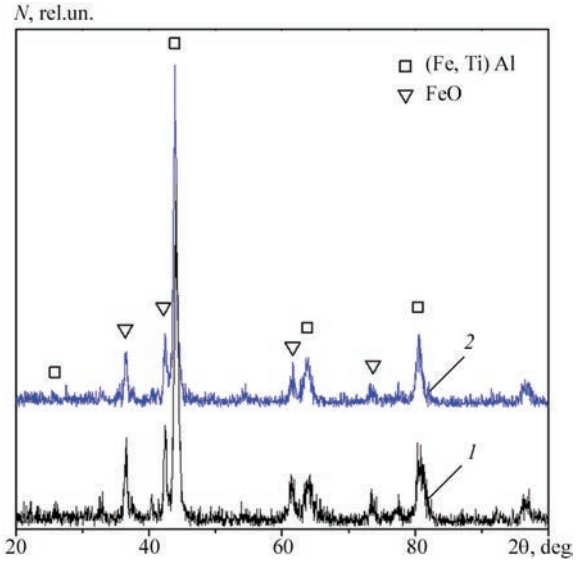

Figure 5. X-ray patterns of plasma coatings from intermetallic (Te, Ti)$_3$A1 powder, produced by the MChS method during 3 h (*a*) and 5 h (*b*)

coatings (Table 2). In the X-ray patterns, a decrease in the intensity of iron oxide peaks is observed when using MChS-powder produced during 5 h, which may indicate a lower amount of iron oxide in this coating.

Evaluation of CSR of the produced coatings from a nanostructural powder of (Fe,Ti)$_3$A1 intermetallic showed that as a result of powder melting in the plasma jet, followed by hardening on the base, the size of the crystallites of the coatings increased from 25 to 60 nm compared to initial powders in case of spraying powder produced by MChS during 3 h and from 10 to 45 nm during spraying powder produced by MChS during 5 h.

The results of determination of such mechanical characteristics of coatings as hardness (H) and modulus of elasticity (E) by the method of microidentation, are given in Table 3. Table also shows the ratio of H/E and H^3/E^2, which are indices of transition from elastic deformations to fracture (normalized hardness) and resistance to plastic deformation, accordingly.

The comparison of values of mechanical characteristics shows that values of hardness and modulus of elasticity of the coating produced from MChS-powder (τ = 5 h) exceed the coating from MChS-powder (τ = 3 h) by 1.8 and 1.7 times, respectively. The difference between the values of mechanical characteristics of the two coatings is predetermined, apparently, by their microstructure. Thus, the coating from MChS-powder (τ = 5 h) is characterized by a thin lamellar structure, a more uniform chemical composition and has a smaller size of crystallites, which contributes to an increase in mechanical characteristics compared to the coating from MChS-powder (τ = 3 h).

Table 3. Mechanical characteristics of plasma coatings from intermetallic (FeTi)$_3$A1 powder, produced by the MChS method during 3 and 5 h

MChS-powder	H, GPa	E, GPa	H/E	H^3/E^2
τ = 3 h	3	47	0.064	0.012
τ =5 h	5.4	80	0.068	0.025

According to the method of evaluation of the structural state of the material using H/E index, proposed by the authors of [12], produced coatings belong to nanostructural materials, since H/E index in both cases is within 0.05–0.09.

Such indices as H/E and H^3/E^2 are indicators of a coating resistance to fracture, which are often used as a criterion for evaluation of wear resistance of protective coatings [13–15]. As is seen from Table 3, as to H/E index, the coating from MChS-powder (τ = 3 h) is somewhat inferior to the coating from MChS-powder (τ = 5 h). Whereas the coating from MChS-powder (τ = 5 h) 2.1 times exceeds the coating from MChS-powder (τ = 3 h). The obtained data indicate that the coating sprayed using the powder produced by MChS during 5 h, has a higher wear resistance.

CONCLUSIONS

As a result of spraying nanostructural powders of (Fe, Ti)$_3$Al intermetallic produced by the MChS method during 3 and 5 h, nanostructural coatings are formed, the size of crystallites in which is 60 and 45 nm, respectively. The phase composition of powders is inherited by plasma coatings, the main phase in which is the intermetallic (Fe, Ti)$_3$Al phase with the presence of FeO iron oxide.

It is shown that an increase in time of MChS of (Fe, Ti)$_3$Al intermetallic powder from 3 to 5 h allows forming a coating in the conditions of plasma spraying with a thin lamellar structure and a uniform distribution of initial elements in the volume of the coating. In this case, the porosity of the coating decreases from 6.8 to 4.5 %.

Using the method of micro-indentation, it was found that according to such main indices of mechanical characteristics of a coating as hardness and modulus of elasticity, the coating from MChS-powder, produced during 5 h, exceeds the coating from MChS-powder, produced during 3 h by 1.8 and 1.7 times, respectively. The values of normalized hardness (H/E) and resistance to plastic deformation (H^3/E^2), which are the criteria of wear resistance, are also greater in the coating during spraying MChS-powder produced by processing during 5 h.

The carried out studies indicate the prospects of using mechanically synthesized powder of (Fe, Ti)$_3$Al intermetallic, produced at the time of processing ini-

tial mixtures during 5 h, for plasma spraying of coatings operating under wear conditions.

REFERENCES

1. Cinca, N., Lima, C. R. C., Guilemany, J. M. (2013) An overview of intermetallics research and application: Status of thermal spray coatings. *J. of Materials Research and Technology*, 2(**1**), 75–86. DOI: https://doi.org/10.1016/j.jmrt.2013.03.013
2. Palm, M., Stein, F., Dehm, G. (2019) Iron aluminides. *Annual Review of Materials Research*, **49**, 297–326. DOI: https://doi.org/10.1146/annurev-matsci-070218-125911
3. Zamanzade, M., Barnoush, A., Motz, C. (2016) A review on the properties of iron aluminide intermetallics. *Crystals*, 6(**1**), 10. DOI: https://doi.org/10.3390/cryst6010010
4. Moszner, Peng, Suutala, Jasnau, Damani, Palm (2019) Application of iron aluminides in the combustion chamber of large bore 2-stroke marine engines. *Metals*, 9(**8**), 847. DOI: https://doi.org/10.3390/met9080847
5. Bahadur, A. (2003) Enhancement of high temperature strength and room temperature ductility of iron aluminides by alloying. *Materials Science and Technology*, 19(**12**), 1627–1634. DOI: https://doi.org/10.1179/026708303225008266
6. Rafiei, M., Enayati, M.H., Karimzadeh, F. (2009) Characterization and formation mechanism of nanocrystalline (Fe, Ti)$_3$Al intermetallic compound prepared by mechanical alloying. *J. of Alloys and Compounds*, 480(**2**), 392–396. DOI: https://doi.org/10.1016/j.jallcom.2009.02.072
7. Senderowski, C., Cinca, N., Dosta, S. et. al. (2019) The effect of hot treatment on composition and microstructure of HVOF iron aluminide coatings in Na_2SO_4 molten salts. *J. of Thermal Spray Technology*, 28(**7**), 1492–1510. DOI: https://doi.org/10.1007/s11666-019-00886-w
8. Fikus, B., Senderowski, C. Panas, A.J. (2019) Modeling of dynamics and thermal history of $Fe_{40}Al$ intermetallic powder particles under gas detonation spraying using propane-air mixture. *J. of Thermal Spray Technology*, **28**, 346–358. DOI: https://doi.org/10.1007/s11666-019-00836-6
9. Senderowski, C., Vigilianska, N., Burlachenko, O. et. al. (2023) Effect of APS spraying parameters on the microstructure formation of Fe_3Al intermetallics coatings using mechanochemically synthesized nanocrystalline Fe–Al powders. *Materials*, **16**, 1669. DOI: https://doi.org/10.3390/ma16041669
10. Borisov, Yu.S., Borisova, A.L., Vihilyanska, N.V. et. al. (2021) Electric arc spraying of intermetallic Fe–Al coatings using different solid and powder wires. *The Paton Welding J.*, **3**, 16–21. DOI: https://doi.org/10.37434/tpwj2021.03.03
11. Borisov, Yu.S., Borisova, A.L., Burlachenko, A.N. et. al. (2017) Structure and properties of alloyed powders based on Fe3Al intermetallic for thermal spraying produced using mechanochemical synthesis method. *The Paton Welding J.*, **9**, 33–39. DOI: https://doi.org/10.15407/tpwj2017.09.06
12. Firstov, S.A., Gorban, V.F., Pechkovskiy, E.P. (2009) *New procedure of treatment and analysis of results of automatic indentation of materials*. Kyiv, Logos [in Russian].
13. Chen, X., Du, Y., Chung, Y.-W. (2019) Commentary on using H/E and H/E as proxies for fracture toughness of hard coatings. *Thin Solid Films*, **688**, 137265. DOI: https://doi.org/10.1016/j.tsf.2019.04.040
14. Cui, C, Yang, C. (2023) Mechanical properties and wear resistance of CrSiN coating fabricated by magnetron sputtering on W18Cr4V steel. *Coatings*, 13(**5**), 889. DOI: https://doi.org/10.3390/coatings13050889
15. Beake, B. (2022) The influence of the H/E ratio on wear resistance of coating systems — Insights from small-scale testing. *Surface and Coatings Technology*, **442**, 128272. DOI: https://doi.org/10.1016/j.surfcoat.2022.128272

ORCID

O.P. Gryshchenko: 0000-0003-2640-8656,
N.V. Vihilianska: 0000-0001-8576-2095,
O.M. Burlachenko: 0000-0001-8576-2095,
C. Senderowski: 0000-0002-0331-3702

CONFLICT OF INTEREST

The Authors declare no conflict of interest

CORRESPONDING AUTHOR

O.P. Gryshchenko
E.O. Paton Electric Welding Institute of the NASU
11 Kazymyr Malevych Str., 03150, Kyiv, Ukraine.
E-mail: grinya3679@gmail.com

SUGGESTED CITATION

O.P. Gryshchenko, N.V. Vihilianska, O.M. Burlachenko, C. Senderowski, V.F. Gorban (2023) Studying the impact of duration of technochemical synthesis of nanostructure (Fe, Ti)$_3$Al powder on characteristics of plasma coatings. *The Paton Welding J.*, **10**, 24–29.

JOURNAL HOME PAGE

https://patonpublishinghouse.com/eng/journals/tpwj

Received: 28.06.2023
Accepted: 14.11.2023

DOI: https://doi.org/10.37434/tpwj2023.10.05

MULTIPURPOSE ELECTRON BEAM UNIT UE-5810

S.V. Akhonin[1], V.O. Berezos[1], A.Yu. Severyn[1], V.D. Kornijchuk[2], Iu.T. Ishchuk[2], O.G. Erokhin[2]

[1]E.O. Paton Electric Welding Institute of the NASU
11 Kazymyr Malevych Str., 03150, Kyiv, Ukraine
[2]SE "SPC "Titan" of the E.O. Paton Electric Welding Institute of the NAS of Ukraine»
26 Raketna Str., Kyiv, Ukraine

ABSTRACT

In order to implement the electron beam melting technologies the E.O.Paton Electric Welding Institute of NASU developed a multifunctional electron beam unit UE-5810 of megawatt class, designed for producing ingots of titanium and its alloys of up to 20 tons weight. Description of a multipurpose universal electron beam unit UE-5810 and its specification are given. Functional features of the components of the unit, technological fixtures and electron guns are described. Electron beam unit UE-5810 is a reliable highly efficient installation of industrial type for melting highly reactive metals and alloys, as well as treatment of the produced ingots by glazing.

KEYWORDS: electron beam unit, electron beam gun, technological fixtures, melting, glazing, ingot

INTRODUCTION

High requirements to metal product quality, as well as significant achievements in improvement of operational reliability of electron beam equipment and its automation, lead to ever wider application of the technology of electron beam melting (EBM) in metallurgical processing of titanium [1–3]. The predicted total annual industrial capacity of production of ingots of titanium and its alloys exactly by EBM method can exceed 50 thou t per year in the near future [4]. Such a tendency is first of all due to the fact that based on electron beam application as an independent powerful heat source the EBM technology has received a reliable technological implementation in the recent years in the form of modern highly productive and efficient electron beam units designed by such companies as TIMET (USA), TyssenKrupp (Germany), TOHO Titanium (Japan), Panzhihua Steel Titanium Industry Company (China), SC "SPC "Titan" of the E.O. Paton Electric Welding Institute of the NAS of Ukraine", which ensure production of high-quality titanium ingots and lowering of the cost of metallurgical processing of titanium [5, 6].

Therefore, the main tendency in development of equipment for EBM technology realization is creation of large multifunctional electron beam units of megawatt class, designed for melting ingots of more than 10 ton weight.

In Ukraine extensive experience of development of such units has been accumulated [5–8]. Electron beam units of the latest generation allow, due to a rather simple operation of technological fixture replacement, implementing practically all the EBM technological schemes. In 2004 PWI designed, built and put into operation a universal multipurpose industrial electron beam unit UE-5810 with the annual capacity of 1.5 thou t, which has no analogs in the world (Figure 1).

UE-5810 design differs from that of the units earlier developed and operating in the industry of Ukraine by a higher level of technical and economic characteristics [9]. In UE-5810 the mechanisms for raw materials feeding into the melting zone and ingot drawing are made as chain ones. It allows doubling the overall dimensions of the load and ingot chambers, compared to the rod design of the feed mechanisms,

Figure 1. Appearance of electron beam unit UE-5810

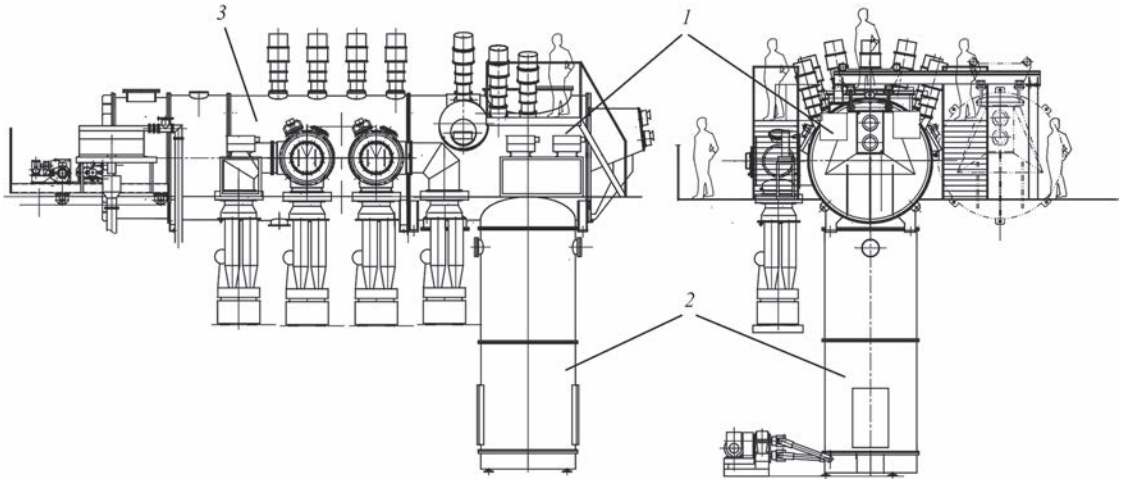

Figure 2. Design of electron beam unit UE-5810: *1* — melting chamber; *2* — drawing chamber; *3* — billet/glazing chamber

significantly reducing the mounting space, and increasing the length of the produced ingots. Moreover, the unit features a high adaptability-to-manufacture, when conducting some melting processes, which is achieved by a simple replacement of one fixture by another one. In particular, it allows melting ingots of a round cross-section from 400 to 1200 mm, rectangular cross-section of the dimensions from 155×950 to 410×1310 mm and up to 4 m length.

The unit traditionally consists of the chambers for melting, ingot drawing and its loading. The load chamber, if required, is transformed into the ingot glazing chamber (Figure 2). All the chambers have forced water cooling.

Main technical characteristics of electron beam unit UE-5810 are as follows:

Installed power, kV·A	5100
Technological power, kW	3700
Accelerating voltage, kV	30
Number of guns, pcs	11
Largest dimensions of the billet, m:	
length	6
cross-section	0.9
Largest dimensions of the ingots, m:	
length	4.0
diameter	1.2
For rectangular cross-section, m	1.3×0.4
Unit overall dimensions, m	27×10×6

Here, considering all the advantages of cold-hearth electron beam melting, in addition to regular titanium scrap, it is possible to use uncrushed titanium sponge blocks (as initial charge), which allows an essential cost reduction for production of titanium ingots of up to 1200 mm diameter. Moreover, UE-5810 design allows combining the processes of melting of the block side surface already at the stage of preheating and melting in one vacuum chamber. Melting of uncrushed sponge titanium blocks of 0.7–5.0 t weight in electron beam unit UE-5810 (Figure 3) allows eliminating from the technological cycle of ingot production not only the stage of consumable electrode compacting for further remelting, but also the operation of block crushing and sponge titanium sorting into lumps of up to 70 mm size; and using low-grade titanium sponge in remelting [10]. This, in its turn, ensures improvement of technical and economic indices by 20 %, compared with EBM of sponge titanium

Figure 3. EBM of sponge titanium blocks; *a* — 4 t sponge titanium block, compared to 0.7 ton block; *b* — EBM of 1100 mm dia. ingot from uncrushed sponge titanium blocks

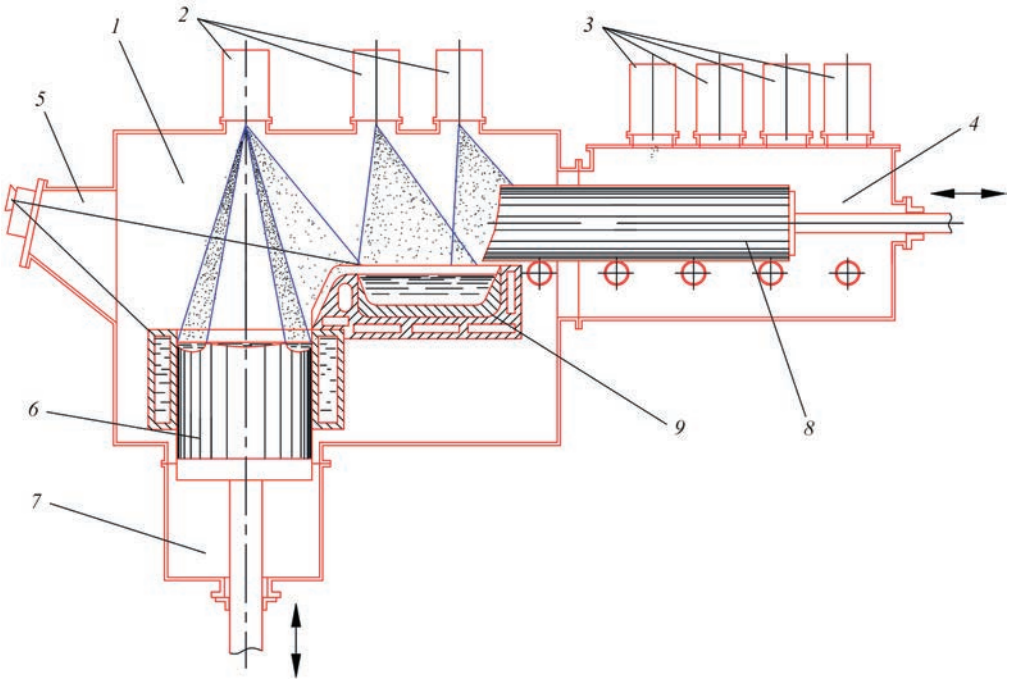

Figure 4. Scheme of UE-5810 unit: *1* — melting chamber; *2* — melting electron beam guns; *3* — glazing electron beam guns; *4* — billet/glazing chamber; *5* — viewing system; *6* — ingot; *7* — ingot chamber; *8* — charge billet; *9* — cold hearth

with 12–70 mm particle size and significantly reduces the costs for production of titanium ingots of up to 1200 mm diameter and up to 4000 mm length from initial raw materials.

Six electron beam guns are installed in the melting chamber to directly conduct the process of producing the ingot, and five electron beam guns are mounted on the billet/glazing chamber for preheating the charge during ingot production or conducting the process of treatment of the ingot surface by its glazing by the electron beams (Figure 4).

Vacuum system consists of three pairs of roughing mechanical pumps of NVZ-300 and 2DVN-1500 type and four booster oil-vapour pumps 2NVBM-630 (Figure 5). Each gun is reinforced by an individual diffusion pump N-160. Vacuum system of UE-5810 unit allows creating rarefaction in the melting chamber space (10^{-2} Pa) and in the guns (10^{-3} Pa), which

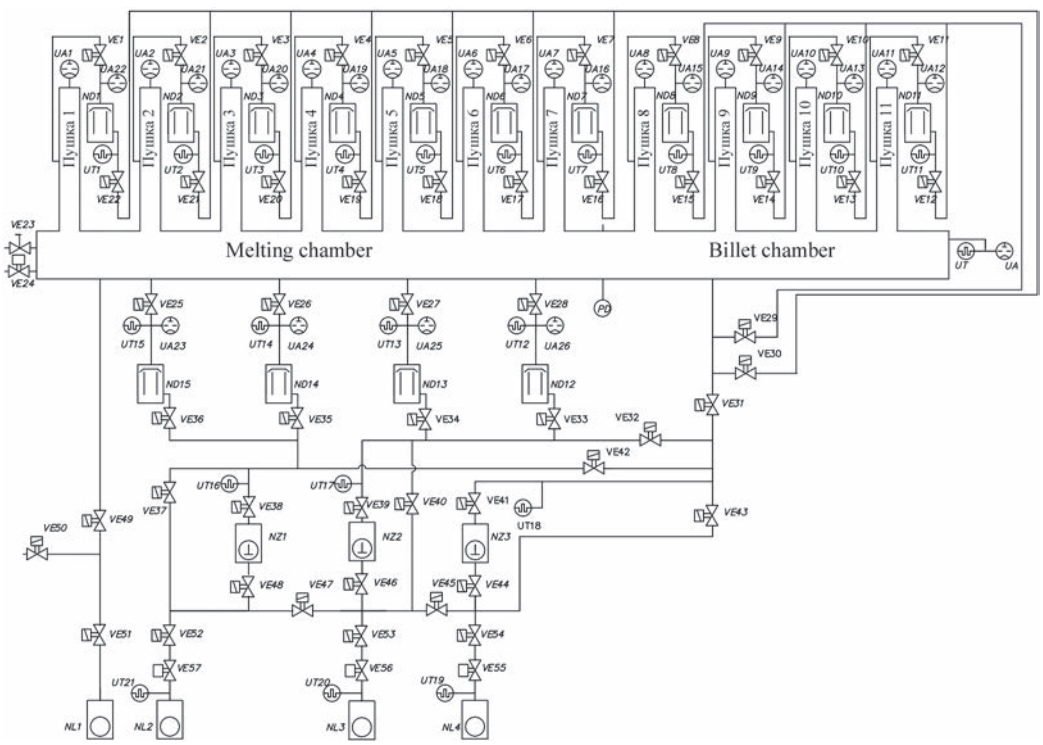

Figure 5. Scheme of vacuum system of electron beam unit UE-5810

ensures trouble-free operation of the guns and the required degree of refining of the metal being remelted during the entire technological process.

UE-5810 unit is fitted with Paton-300 electron beam guns of axial type [1], the total number of which in the unit is 11 pcs (Figure 6).

Specification of Paton-300 gun

Rated power, kW	300
Accelerating voltage, kV	30
Maximum scanning frequency, Hz	1000
Maximal current, A	10
Angle of beam deflection from the gun axis, deg	0–35

Owing to the capability of program scanning with the electron beam over the metal pool surface, the cross-sectional shape of the crucible, and, hence, of the forming ingot, can be different (round, rectangular, square or of some other more complex shape, if required).

During EBM ingot production, their surface can have defects of different casting origin. Traditionally, ingots with such defects are treated by machining, here the amount of wastes in the form of shavings, can be up to 15 %, depending on ingot range. At present the technology of electron beam glazing of the side surface of ingots of a round and rectangular cross-section has been developed and introduced into production [11]. Here, the ingot surface after electron beam glazing is even, defect-free and does not require any further machining [12].

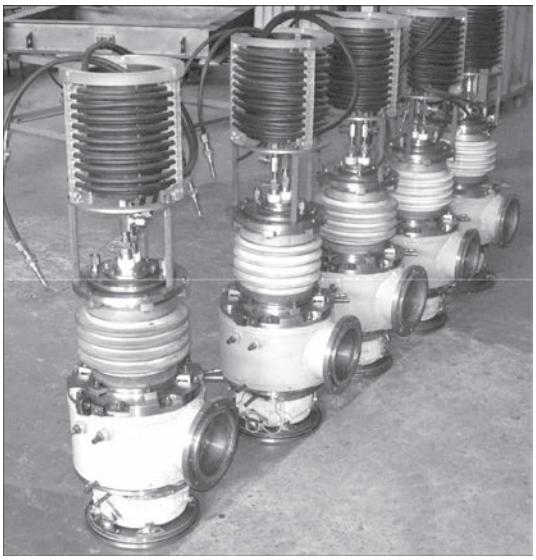

Figure 6. Paton-300 electron beam guns

Therefore, with the purpose of unification of electron beam unit UE-5810 it was designed so as to combine the processes of melting and glazing of the ingot side surface. Here, rotary rolls were mounted in the load chamber, on which the non-consumable box with the charge is directly installed in the ingot production process, or the box is removed and the ingot is loaded onto the rotary rolls for conducting the process of its glazing (Figure 7).

UE-5810 design envisages the possibility of glazing round ingots of up to 1200 mm diameter (Figure 8)

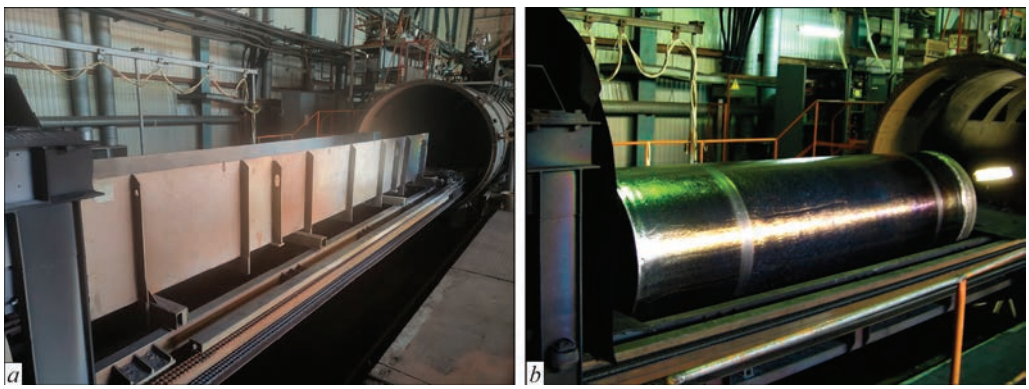

Figure 7. Billet/glazing chamber: *a* — with loaded box with charge for producing the ingot; *b* — with loaded ingot after glazing

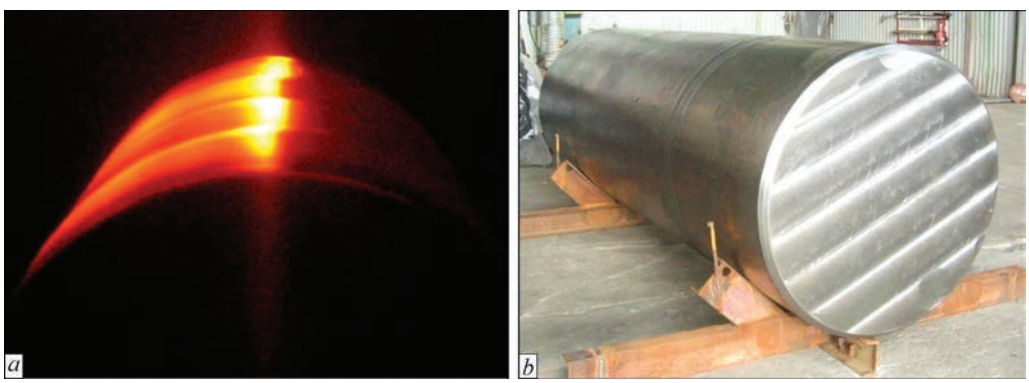

Figure 8. Glazing process (*a*) and glazed ingot of 1100 mm diameter (*b*)

or slab ingots of 410×1310 mm cross-section and up to 4 m length. For realization of this feature, five axial-type electron beam guns are mounted in the upper part of the load chamber. The load chamber proper accommodates the mechanism of ingot rotation for its glazing, which consists of two rotary rolls located in parallel. Four viewing systems are mounted on the load chamber side wall to the right of the operator to allow the technologist to control the glazing process.

During the entire operation period, electron beam unit UE-5810 proved to be a reliable high-efficient installation of industrial type for producing highly reactive metals and alloys, as well as treatment of the produced ingot surface by glazing.

REFERENCES

1. Paton, B.E., Trigub, N.P., Akhonin, S.V., Zhuk, G.V. (2006) *Electron beam melting of titanium*. Kyiv, Naukova Dumka [in Russian].
2. Ladokhin, S.V. (2010) Prospects of creation of electron beam melting installations of new generation in Ukraine. *Visnyk DDMA,* **3**, 170–173 [in Russian].
3. *Xiaojun* Wang, Zhanqian Chen, Feng Chen et al. (2007) The electron beam cold hearth melting technology. In: *Proc. of 11th World Conf. on Titanium (Ti-2007): Science and Technology (3–7 June 2007, Kyoto, Japan)*. Ed. by M. Niinomi, Vol. 2, 185–188.
4. http://www.antares.com.ua/upload/file/3Titanium_Production_Presentation_rus.pdf
5. Trigub, N.P., Zhuk, G.V., Kornejchuk, V.D. et al. (2007) Commercial electron beam installation UE-5812. *Advances in Elektrometallurgy,* **1**, 9–11.
6. Sobko-Nesteruk, O.E., Tretyak, N.G., Chaika, N.V. et al. (2012) New VT02 furnace for electron beam melting of titanium alloys constructed at the Antares company. *Advances in Electrometallurgy,* **3**, 178–184.
7. Akhonin, S.V., Pikulin, A.N., Berezos, V.A. et al. (2019) Laboratory electron beam unit UE-208M. *Suchasna Elektrometal.,* **3**, 15–22 [in Russian].
8. Trigub, N.P., Zhuk, G.V., Pap, P.A. et al. (2003) Electron beam installation UE-121. *Advances in Electrometallurgy,* **2**, 17–20.
9. Paton, B.E., Trigub, N.P., Kozlitin, D.A. et al. (1997) *Electron beam melting.* Kyiv, Naukova Dumka [in Russian].
10. Paton, B.E., Trigub, N.P., Akhonin, S.V. (2005) Producing of titanium alloys from uncrushed blocks of spongy titanium by electron beam melting. *Titan,* **2**, 23–25 [in Russian].
11. Pikulin, A.N., Zhuk, G.V., Trigub, N.P., Akhonin, S.V. (2003) Electron beam fusion of titanium ingots. *Advances in Electrometallurgy,* **4**, 17–19.
12. Pikulin, A.N. (2016) Electron beam fusion of ingots of complexly-alloyed titanium alloys. *Sovrem. Elektrometall.,* **3**, 26–30.

ORCID

S.V. Akhonin: 0000-0002-7746-2946,
V.O. Berezos: 0000-0002-5026-7366,
A.Yu. Severyn: 0000-0003-4768-2363,
O.G. Erokhin: 0000-0003-2105-5783

CONFLICT OF INTEREST

The Authors declare no conflict of interest

CORRESPONDING AUTHOR

S.V. Akhonin
E.O. Paton Electric Welding Institute of the NASU
11 Kazymyr Malevych Str., 03150, Kyiv, Ukraine.
E-mail: akhonin.sv@gmail.com

SUGGESTED CITATION

S.V. Akhonin, V.O. Berezos, A.Yu. Severyn, V.D. Kornijchuk, Iu.T. Ishchuk, O.G. Erokhin (2023) Multipurpose electron beam unit UE-5810. *The Paton Welding J.*, **10**, 30–34.

JOURNAL HOME PAGE

https://patonpublishinghouse.com/eng/journals/tpwj

Received: 12.07.2023
Accepted: 14.11.2023

DOI: https://doi.org/10.37434/tpwj2023.10.06

NEW GENERATION UNIT FOR PLASMA-ARC DEPOSITION OF COATINGS AND ATOMISATION OF CURRENT-CARRYING WIRE MATERIALS

V.M. Korzhyk, D.V., Strogonov, O.M. Burlachenko, O.V. Ganushchak, O.M. Voitenko

E.O. Paton Electric Welding Institute of the NASU
11 Kazymyr Malevych Str., 03150, Kyiv, Ukraine

ABSTRACT

A plasma-arc unit of industrial type of up to 50 kW total power for deposition of functional coatings on critical parts and spheroidization of wire materials is presented. A feature of the unit is application of a system of water cooling of plasmatron internal components, modified design of the nozzle and cathode parts and reduction of plasmatron overall dimensions, ensuring a higher productivity of the process, widening of its application areas, improvement of mechanical and technological characteristics of the produced granules and coatings, etc. Presented is the microstructure and results of studying the granulometric composition of the dispersed phase, which are indicative of producing dense coatings with less than 1 % porosity, forming from granules of a spherical shape predominantly in a narrow particle size range of 20–100 μm.

KEYWORDS: plasma-arc atomization, current-carrying wire, coating deposition, spheroidization, granulometric composition, binding strength, density, sphericity

INTRODUCTION

The first studies of the process of plasma-arc spraying were performed in the 60s of the previous century. The impetus for this was the rapid development of aviation and missile technology, which required creation of new efficient methods of deposition of refractory coatings on heavy-duty parts of aviation and missile gas turbine engines (GTE) and liquid rocket engines (LRE). In 1961 the process of plasma-arc spraying using current-carrying wire-anode was patented in the USA [1]. Development of this process was due, primarily, to a number of problems, arising in spraying with powder materials by transferred-arc plasmatrons, in particular low erosion resistance of copper nozzles in the anode spot zone, low values of the efficiency factor (EF) of powder heating in the plasma jet, material utilization coefficient (MUC) on the level of 20–60 %, etc. [2, 3]. In the USSR this method has also become widely accepted. For instance in works [4–7] the authors used this technology to deposit coatings in IMET-108 unit (Baikov IMET of RAS) (Figure 1, *a*) and obtained spherical powers from refractory wire materials based on tungsten, molybdenum, niobium, etc. It should be noted that this process ensured a high productivity, which at the power of 20–25 kW was equal to 10–12 kg/h for tungsten wire. However, the above-mentioned process had the significant disadvantages of a wide granulometric composition of the sprayed particles in the range of 40–1000 μm, and a considerable degree of their oxidation as a result of a short length of the argon jet, which resulted in a low density of the applied coatings (porosity of 4–10 %), binding strength of 25–35 MPa, etc.

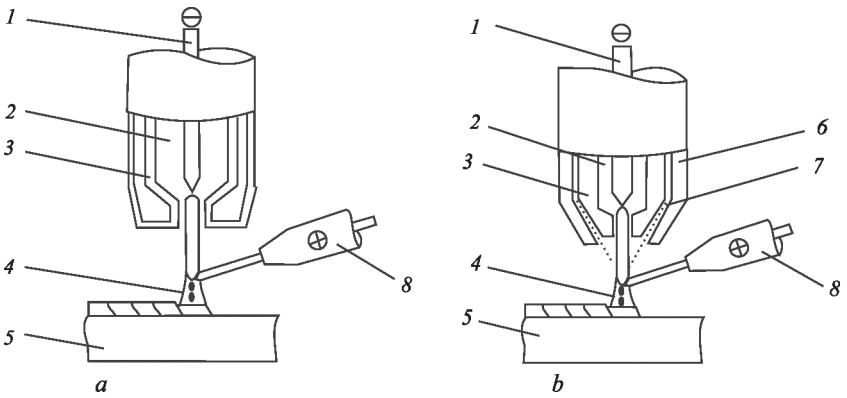

Figure 1. Main varieties of the process of plasma-arc spraying of current-carrying wire materials with (*a*) and without (*b*) use of accompanying gas flow, respectively: *1* — nonconsumable tungsten cathode; *2* — plasma forming gas injection; *3* — plasma forming nozzle; *4* — spaying particle plume; *5* — product; *6* — compressing nozzle; *7* — accompanying gas flow; *8* — consumable wire-anode

Further development of this method was design and manufacturing of serial units UN-126 and KT-088 (PWI, Ukraine) [8, 9] and PLAZER 30-PL-W (R&D PLAZER Center Ltd, Ukraine) [10], where the above-mentioned disadvantages were eliminated through application of an accompanying gas jet (Figure 1, *b*). The accompanying gas flow directed coaxially to the plasma one forms the configuration of the latter, promotes its compression, and, thus, reduces the opening angle of spraying particle plume, increases the outflow velocity and dynamic head of the plasma jet, which, in its turn, creates the conditions required for achieving the optimal granulometric and chemical compositions of the dispersed phase [11]. It leads to reduction of coating porosity to 1–4 %, increase of the coating binding strength to 40–60 MPa, etc. This technology has reached its maximum development abroad at the beginning of 2000s, and it became known as Plasma Transferred Wire Arc (PTWA) process. PTWA technology was patented in 2009, and it is used predominantly at reconditioning and improvement of wear resistance of inner surfaces (> 50 mm) of such engine elements, as cylinder blocks for Ford, Nissan, Volkswagen concerns, etc. The main scope of work on development of such equipment was performed in the USA (Flame Spray Industries), Germany (GTV), and Switzerland (Oerlikon). This method is characterized by high properties of the sprayed coating strength (up to 80 MPa), low porosity (1–2 %), productivity (on the level of 10 kg/h), etc. [12].

In addition to the coating sphere, this technology has received a boost with development of additive technologies of printing 3D products, and it is becoming widely accepted for manufacturing high-quality spherical granules, which are produced during the process of wire material atomization (Plasma Atomization Technology (PAT)) [13]. At present equipment is known [14, 15], which allows producing granules with the sphericity coefficient higher than 0.8 and more than 50 wt.% yield of 20–100 μm size fraction.

Note, however, that at present, the plasma-arc spraying and atomization method has several significant limitations on productivity, which in the general case is not more than 12 kg/h, and does not allow using compact wires of more than 2.0 mm diameter, and in the case of atomization of more than 1.6 mm flux-cored wires with refractory non-conductive components (WC, B_4C, etc.) it does not allow ensuring the processes of metallurgical interaction of the flux-cored wire sheath and core, resulting in formation of granules with a high degree of heterogeneity by chemical and phase composition. This is due to limited power of plasma-arc equipment, which is not higher than 30 kW (300 A and 100 V) for all the equipment models, as a result of application of gas cooling system.

Therefore, further advance of this plasma-arc spraying and atomization technology can consist in development of new plasmatron designs with water cooling and optimized geometry of the nozzle part and smaller overall dimensions, which will allow raising the current load from 300 to 500 A, improving the process productivity, increasing the plasma jet velocity characteristics, intensifying the processes of wire dispersion and of metallurgical interaction in melting of flux-cored wire components, etc.

DEVELOPMENT OF HIGHER POWER PLASMATRON FOR PLASMA-ARC ATOMIZATION AND DEPOSITION OF COATINGS FROM CURRENT-CARRYING WIRES

Proceeding from the results of earlier developments and gained experience of operation of serial versions of plasmatrons for plasma-arc spraying, a goal was set to develop a plasmatron of PLAZER 50-W model of a higher power (up to 50 kW) and with enhanced technological capabilities (both for producing spherical granules, and for coating deposition on the external and inner surfaces of ≥ 70 mm diameter).

Optimization of the plasmatron design consisted in the following:

- increase of the current load due to designing a system of water cooling of the nozzle part, cathode and anode assemblies. It allowed application of currents on the level of 400 to 500 A, compared to serial PLAZER 30-M plasmatron of PLASZER 30-PL-W unit [10], where this value cannot exceed 300 A, because of air cooling application. Moreover, a design with water cooling allows using helium or a mixture on its base as the plasma forming gas, which, in its turn intensifies the processes of heating, melting, dispersion and spheroidization of current-carrying compact and flux-cored wires;
- optimization of the gas-discharge chamber geometry due to a change in the ratios of the nozzle channel length (l_n) to its diameter (d_n) from 1.0 to 1.4, which provides a 15 % increase of the maximal velocity of the plasma jet outflow from 520 to 600 m/s, according to calculations using Computational Fluid Dynamics (CFD) software (Figure 2), and
- construction of a spherical section, which expands at the nozzle outlet (by the type of Laval nozzle [16]), and ensures a more homogeneous temperature and electric density of the plasma and length of the plasma jet, which, in its turn, intensifies the spheroidization processes and provides greater acceleration of the particles.

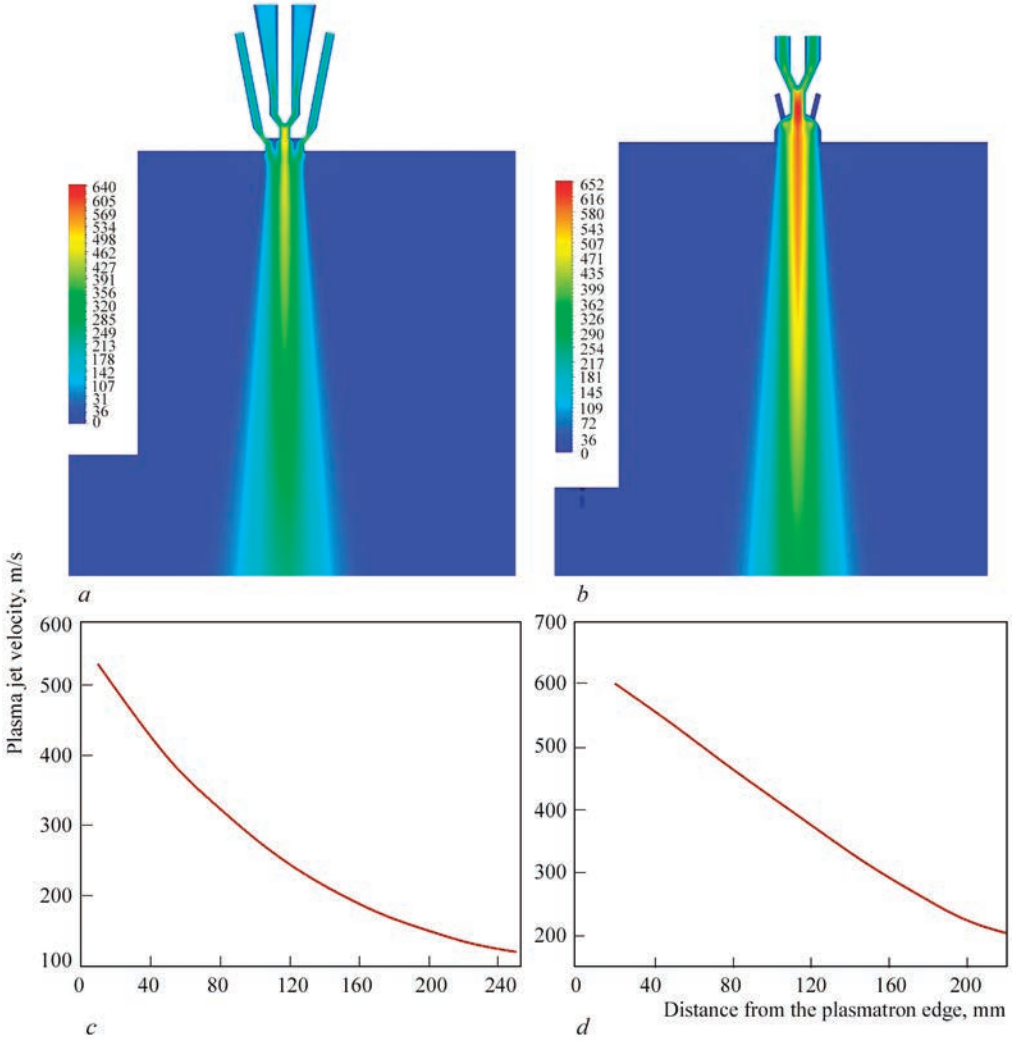

Figure 2. Visualization of the process of modeling velocity characteristics of the plasma jet (*a*, *b*) and dependencies of the plasma jet velocity on the distance from the plasmatron edge (*c*, *d*): *a*, *c* — serial PLAZER 30-W plasmatron; *b*, *d* — developed PLAZER 50-W plasmatron

An improved system of plasma jet blowing by an accompanying gas flow in the zone of atomization cone formation was also developed, which ensures laminar outflow of the accompanying gas flow (compared with the prototype, where the accompanying gas flow comes out through an annular gap with a predominantly turbulent nature of movement). It ensures greater extent of the high-velocity high-temperature zone of the plasma jet, reduction of the angle of opening of the atomization cone and achieving an optimal composition of the dispersed phase.

Appearance and design of the new PLAZER 50-W plasmatron (Figure 3) and its characteristics are given below.

Technical characteristics of serial PLAZER 30-W and developed PLAZER 50-W plasmatrons

	PLAZER 30-W	PLAZER 50-W
Maximal current, A	300	500
Maximal voltage, V	80	120
Accompanying gas flow rate, m^3/h	30–60	15–30
Plasma forming gas flow rate, m^3/h	13	13
Plasma forming gas type	Argon	Argon, helium and their mixtures
Nozzle diameter, mm	3	3
Overall dimensions L×W×H, mm	90×70×175	250×60×50
Weight, kg	1,5	1,5
Cooling type	Air	Water

As one can see from the technical characteristics, the developed PLAZER 50-W plasmatron has the following differences from plasmatron of the previous PLAZER 30-W modification: increase of the current load on the plasmatron internal parts from 300 to 500 A due to replacement of air cooling system by water cooling; more efficient cooling of the plasmatron cathode and nozzle assemblies, which allows application of helium and mixtures on its base as plasma forming gas, that greatly enhance the plasma arc power (due to voltage increase from 80 to 120 V) and

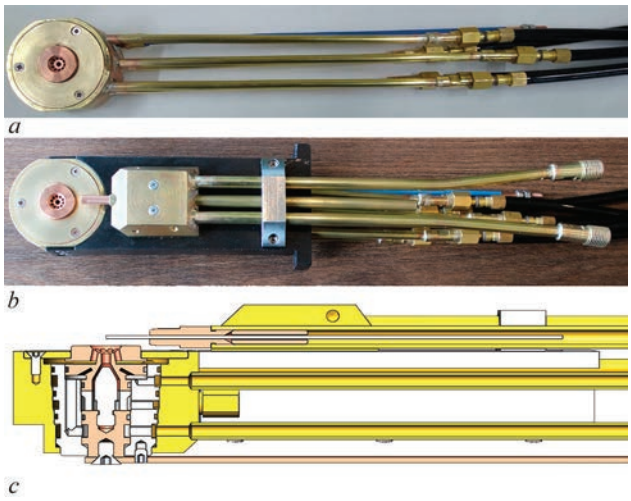

Figure 3. Appearance and computer 3D model of the developed PLAZER 50-W plasmatron for plasma-arc spraying: *a* — appearance; *b* — appearance as an assembly with the cathode unit and fastening to the manipulator; *c* — 3D model of gas-discharge chamber

increase the effectiveness of heating of consumable wire-anode; higher velocity of plasma jet outflow and greater extent of argon plasma zone at plasma jet compression by accompanying gas, the optimal effect of this being manifested at its lower flow rates (to 30 m^3/h).

Note that owing to its small overall dimensions (height dimension), the plasmatron can be used for spraying inner surfaces of more than 70 mm diameter and for spheroidization of current-carrying wires in atomization chambers (including small-sized ones).

INVESTIGATION OF GRANULOMETRIC COMPOSITION AND MICROSTRUCTURE OF COATINGS PRODUCED IN THE DEVELOPED PLASMATRON

Comparative studies were performed of granulometric composition of atomization products (spherical granules) at the following technological parameters of plasmatron of the previous modification and the developed one (Table 1).

Analysis of granulometric composition of atomization products (Figure 4) showed that at atomization with serial PLAZER 30-W plasmatron the main powder fraction (90 % of the total weight) is 63–250 μm particle size, and for PLAZER 50-W plasmatron it is 63–160 μm in the absence of 250–315 μm fraction, while the proportion of 160–200 μm fraction does not exceed 2 wt.% (for serial plasmatron this parameter is 20 %).

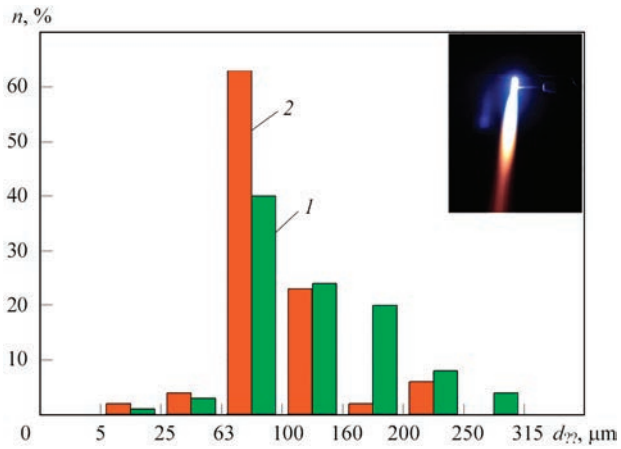

Figure 4. Size distribution of granules produced using the developed PLAZER 50-W plasmatron (*1*) and PLAZER 30-W plasmatron of previous modification (*2*)

The average size of spraying particles was calculated in accordance with the obtained data on size distribution of granules, produced with the use of serial PLAZER 30-W and developed PLAZER 50-W plasmatrons (Figure 4). These calculations showed that the developed design of the plasmatron gas-discharge chamber promotes lowering of this parameter from 134 to 99 μm, which, in its turn, should promote production of a more homogeneous, finely-dispersed lamellar structure of the coating.

These mode parameters were used to spray a coating from current-carrying compact wire from stainless steel of AISI 304 grade (d = 1.6 mm). Figure 5 gives a comparison of microstructure of coatings, sprayed in the serial and developed plasmatrons at the same atomization modes.

Microstructural analysis of the coating, sprayed in the developed plasmatron showed that in this case the coating is more homogeneous, with porosity close to 1 %. The coating structure has almost no round spherical unmelted particles, the lamelle thickness was reduced from 25 to 15 μm.

Studying the shape of dispersed phase particles showed that, on the whole, the granules are of a regular spherical shape (Figure 6), sphericity coefficient (S_{sph}) is equal to 0.75–0.85. Here, the proportion of irregularly shaped granules is not more than ~ 2 wt.%. It should be noted, however, that wire atomization and formation of a jet from overheated particles and their further solidification was performed in air and in water, where the processes of intensive chemical interaction of the wire material with oxygen, nitrogen

Table 1. Parameters of the mode of plasma-arc spraying of current-carrying AISI 304 wire of 1.6 mm diameter

Plasmatron model	Current, A	Arc voltage, V	Argon flow rate, l/min	Air flow rate, m^3/h	Cathode–anode distance, mm	Wire feed rate, m/min
PLAZER 30-W	235	80	50	48	10	10.0
PLAZER 50-W	–»–	85	–»–	30	–»–	10.5

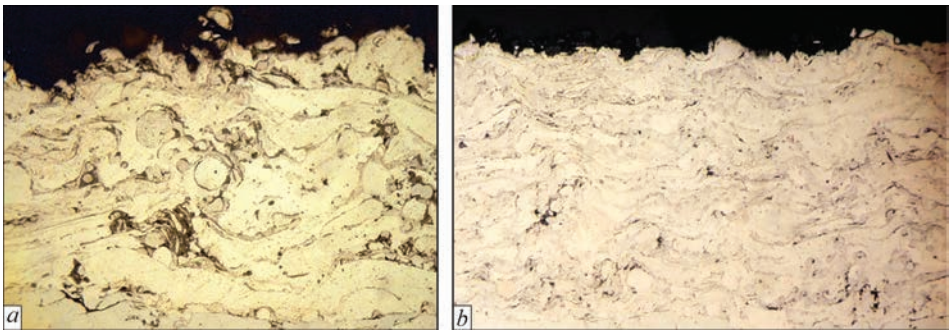

Figure 5. Microstructure of coating from AISI 304 stainless wire, sprayed with serial PLAZER 30-W plasmatron (*a*) and with developed PLAZER 50-W plasmatron (*b*)

and hydrogen are in place, which may lead to deterioration of the powder sphericity parameters. In work [17] it is reported that wire plasma-arc atomization in chambers with inert atmosphere allows producing powder, the sphericity coefficient of which may reach almost 0.90. Therefore, increase of particle sphericity parameters can be achieved due to creation of an inert atmosphere in the environment where the processes of powder atomization, dispersion and solidification take place.

Analyzing the above, the process of plasma-arc atomization of wire materials using PLAZER 50-W plasmatron can be regarded as an industrial process for producing spherical granules with up to 90 wt.% yield of 20–100 μm fraction, which satisfies the requirements to granulometric composition and sphericity coefficient for such processes of 3D printing as Selective Laser Melting (SLM), Selective Laser Sintering (SLS), Direct Metal Laser Sintering (DMLS), etc. On the whole, in this range of granulometric composition practically all the produced fractions can be used both as materials for the most wide spread 3D printing technologies, and for granule metallurgy. 20–80 μm fraction makes up 48 % of the total powder weight (SLM); 45–106 μm is equal to 64 % (SLS); 45–160 μm — 85 % (DMLS); 106–160 μm — 22 % (hot isostatic pressing (HIP)).

Obtained results were tested at spraying of the inner cylindrical surface (d_{in} = 95 mm) by current-carrying compact 1.6 mm wire of AISI 304 grade (Figure 7).

DEVELOPMENT OF NEW GENERATION INSTALLATION FOR PLASMA-ARC ATOMIZATION OF CURRENT-CARRYING WIRES

Application of the developed higher power plasmatron, which ensures wider technological capabilities of the process of plasma-arc atomization of current-carrying wires (wire spheroidization, producing spherical finely-dispersed granules, coating deposition not only on external, but also on inner surfaces of ≥ 70 mm diameter, etc.), requires intellectualization of processes of real-time control and monitoring of a large number of parameters including increase of the degree of automation of the technological process of plasma-arc atomization. A specialized system of unit control was developed for this purpose, which includes measuring, starting and control and signal instrumentation, use of a touch panel, programmable logic controller (PLC) and development of the respective software.

The software covers all the functions of control, adjustment, indication and emergency alarm signalling of the unit operation modes. PLC has the role of executive computing device, which performs correction of atomization process parameters based on the data received from the monitoring system, and corrects the equipment operation algorithms, changing the current, gas flow rate, wire feed rate, etc.

Figure 8, *c* shows the interface windows of the main control system (mobile control panel). They are divided into 5 main windows.

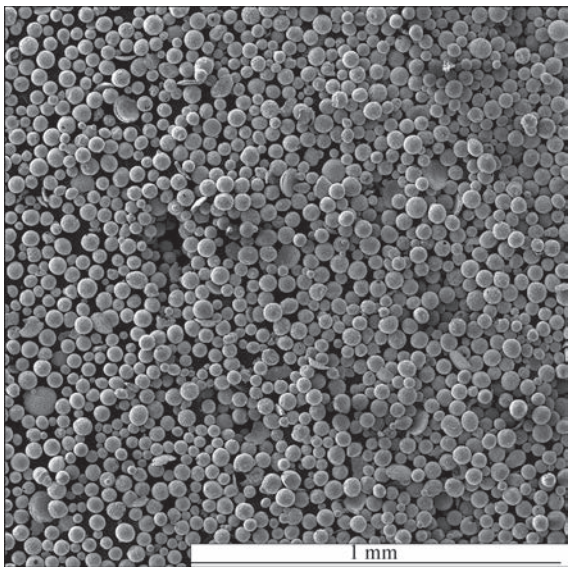

Figure 6. Morphology of granules from AISI 304 stainless steel of 20–100 μm fraction, produced at plasma-arc atomization of 1.6 mm wire

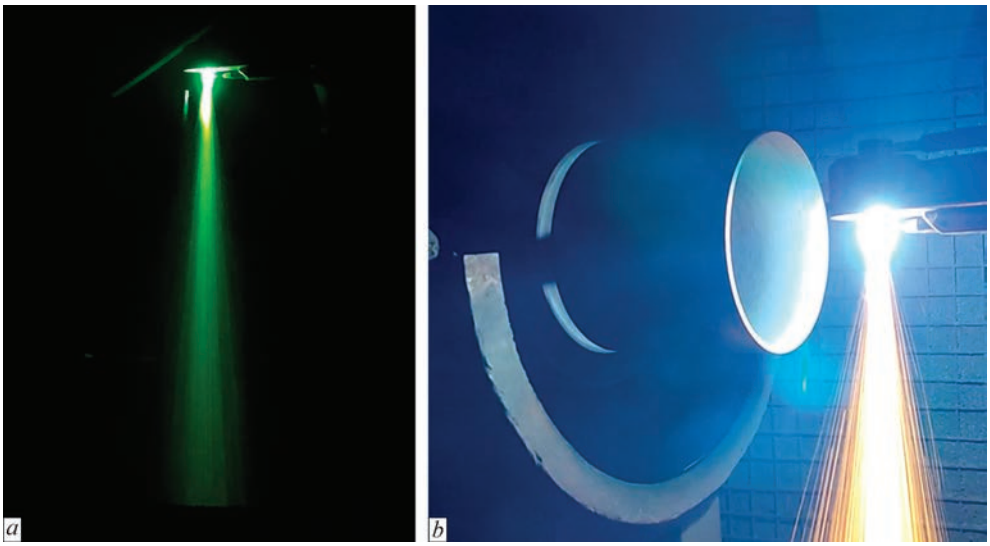

Figure 7. Appearance of two-phase particle-loaded jet (*a*) and process (*b*) of spraying the inner cylindrical surface (d_{in} = 95 mm) with current-carrying compact AISI 304 wire

AUTOMATIC CONTROL WINDOW (AUTO MODE)

Here, the operator assigns the minimum of the main technological parameters, control mode (external start/stop or local), and he can start the equipment. Automated software is fully responsible for controlling the technological process cycle. It runs the process according to pre-defined cyclogram algorithms. Indication and displaying of the main parameters of signal measurement system (current, voltage, gas flow rate and pressure, circuit temperatures, digital status of sensors, valves, etc.) is also given on the left.

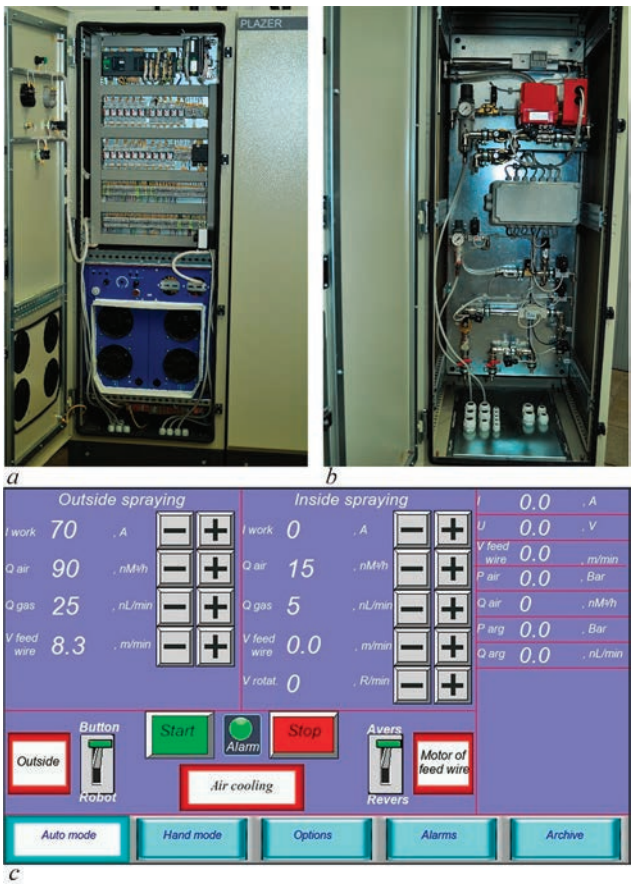

Figure 8. Appearance of the developed control cabinet for the process of plasma-arc spraying of current-carrying wires: *a*, *b* — electric part and gas preparation block, respectively; *c* — interface of the panel of entering the process technological parameters

MANUAL CONTROL MODE (HAND MODE)

This enables flexible control through direct impact of the operator on each assembly of the equipment, controlled by the operator himself. It is recommended to perform manual control only by qualified experts.

EQUIPMENT SETTINGS WINDOW (OPTIONS)

Here, it is possible to assign flexible settings of the equipment, such as signal boundaries, which trigger the emergency monitoring system, as well as starting, ending and transition values of technological parameters, temporary delays, response time during emergency shutdowns and other fine technological adjustments.

ALARM WINDOW (ALARMS)

This window is used for displaying messages in case of emergencies, which based on the last measured data, enable the operator understanding the cause of the emergency shutdown (it can be insufficient gas flow rate, gas pressure, too high or low current/voltage, equipment overheating, etc.). In case of elimination of the cause for the emergency, the technological process can be restarted.

DATA ARCHIVE WINDOW (ARCHIV)

In this window automatic recording and saving of equipment sensor readings will be performed. All the parameters are saved on the flash-card, and they can be exported to a PC for data storage and analysis.

Another distinctive feature of the above equipment is improved ergonomic design and unit control interface, adapted to the processes of plasma-arc spraying of external and inner surfaces and wire spheroidization (Figure 8, *c*). The developed pneumatic-hydraulic diagram (Figure 8, *b*), combined with an upgraded plasmatron design allows using helium and a mixture based on it as plasma forming gas. A possibility of feeding combustible gases into the accompanying gas flow is envisaged, in order to reduce the degree of particle oxidation for a certain range of materials (due to creation of a reducing atmosphere). To improve the process productivity, work on raising the current load in the above-mentioned equipment was performed, in order to increase its energy efficiency (at application of larger wire diameters (2–3 mm)). With this purpose, the thyrisor cooling assembly was upgraded (more powerful fans were selected and installed), which allows increasing the current regulation range from 380 to 500 A.

Production of the described new generation unit (Figure 9) was organized at R&D PLAZER Center Ltd. (Ukraine) under PLAZER 50-PL-W trademark. The above equipment was exported, including to China, to Zibo KNC Petroleum Equipment Co., Ltd, and it is used for protective coating deposition on critical parts of oil production equipment and on pipes of heating surfaces for waste incineration plants with application of compact and flux-cored wires of 1.6–2.4 mm diameter as spraying materials (including those with the core from refractory non-conductive materials).

Specification of PLAZER 50-PL-W installation

Consumed power, kW	Not more than 50
Voltage of 50 Hz three-phase AC mains, V	380^{+19}_{-38}
Open-circuit voltage, V	160
Range of working current adjustment, A	100–500
Range of working voltage adjustment, V	30–100
Longest duty cycle, %	100
Air flow rate at 0.6 MPa pressure, Nm^3/h	15–60
Argon or helium flow rate at 0.1 MPa pressure, Nm^3/h	1–3
Wire feed rate, m/min	2–15
Plasmatron cooling	Water
Plasmatron nozzle and cathode life, h (machine time)	Not less than 100
Water pressure at cooling, MPa	0.3–0.5
Cooling water flow rate, Nm^3/h	0.4–0.6
Diameter of the used wire materials, mm	1.0–2.4
Control type	Automated
Controller type	PLC

CONCLUSIONS

1. A new generation unit for plasma-arc coating deposition and current-carrying wire material atomization was developed. Its features are application of a plasmatron with higher current load and consumable wire heating efficiency, improved weight and dimensional characteristics and intelligent system of automatic control and monitoring of a larger number of technological parameters in real time. Its serial production was organized at R&D PLAZER Center Ltd enterprise (Ukraine).

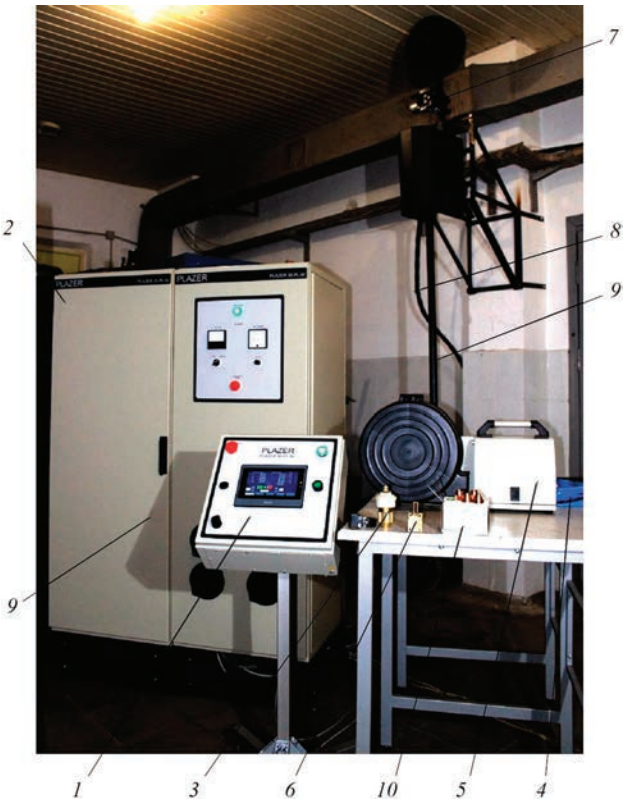

Figure 9. Main components of the unit for coating deposition by plasma-arc spraying of current-carrying wires: *1* — control system with programmable controller and touch panel; *2* — specialized inverter power source; *3* — plasmatron block for spraying of external surfaces with air cooling; *4* — cable-hose pack of the plasmatron for spraying of outer surfaces; *5* — system of fire feed for spraying of external surfaces; *6* — head for spraying of external and inner surfaces with water cooling; *7* — system of wire feed for spraying of inner surfaces; *8* — cable-hose pack of the plasmatron for spraying of inner surfaces; *9* —spare part kit

2. Compared to previous analogs, the developed unit allows: improvement of atomization process productivity from 12 to 16–18 kg/h; using both compact and flux-cored wires of up to 2.4 mm diameter for spraying (including those with a core from refractory non-conductive materials; producing high-quality coatings with less than 1 % porosity; and spheroidized granules with the main finely-dispersed fraction of 20–160 μm.

3. The range of the main parts, on which protective coatings are deposited using the developed unit, includes plungers, rods, pistons of various pumps, rotors, turbine shafts, drill well rods, parts of hydraulic and power equipment, shafts and other parts of ship engines and other ship equipment, parts of chemical equipment, large-sized components of railway equip-

ment (axles, crankshafts, rods and sleeves of locomotive diesel engines) and many other products.

4. Reduction of plasmatron overall dimensions with simultaneous increase of the efficiency of sprayed wire heating in the developed unit promotes expansion of its applications, in particular allows using it both for spraying the external and inner surfaces of more than 70 mm diameter (cylinder blocks, pipe inner surfaces, etc.), and for plasma-arc spheroidization of wires in atomization chambers (including small-sized ones) to produce spherical granules of finely-dispersed fractions with the sphericity coefficient of 0.75–0.85, which meet the requirements to materials for such methods of 3D printing as SLM, SLS, EBM, DMLS and granule metallurgy (HIP).

REFERENCES

1. Yenni, D., McGill, W., Lyle, J. (1961) *Electric arc spraying*. United States, Pat. 2982845.
2. Kudinov, V.V. (1962) Deposition of refractory coatings by arc plasma. *Tekhnologiya Mashinostroeniya,* **21**, 41–45 [in Russian].
3. Kudinov, V.V. (1966) Heating of current-conducting wire by constricted arc. *Svarochn. Proizvodstvo,* **4**, 11–13 [in Russian].
4. Krasnov, A.N. (1965) Plasma spraying of tungsten. *Poroshk. Metallurgiya,* **3**, 1–5 [in Russian].
5. Krasnov, A.N. (1965) Plasma spraying of molybdenum. *Poroshk. Metallurgiya,* **1**, 1–5 [in Russian].
6. Bobrov, G.V., Privezentsev, V.I., Umnova, L.V. (1965) Formation of particles in wire melting in plasma flow. *Poroshk. Metallurgiya,* **1**, 79–86 [in Russian].
7. Petrunichev, V.A., Titkov, V.V. (1977) To mechanism of plasma spraying of wire. *Fizika i Khimiya Obrabotki Materialov,* **1**, 14–16 [in Russian].
8. Zelenin, V.I., Kavunenko, P.M., Tisenkov, V.V. et al. (2009) Application of plasma-arc metallisation for restoration of wheel pairs. *The Paton Welding J.,* **12**, 28–31.
9. Zelenin, V.I., Kavunenko, P.M., Teplyuk, V.M. et al. (2009) Improved technology for restoration of axle necks of wheel pairs of freight-car trucks. *Svarshchik,* **12**, 8–9 [in Russian].
10. Korzhik, V.N., Korob, M.F. (2012) Mechanized line PLAZER 30PL-W for plasma-arc wire spraying of coatings on large-sized parts of «shaft» type. *Svarshchik,* **4**, 13–15 [in Russian].
11. Korzhyk, V.M., Khaskin, V.Yu., Yao Yuhui, Demianov, O.I. et al. (2022) Influence of accompanying compressing air flow on the coating structure and properties in plasma-arc spraying by consumable current-conducting wire. *The Paton Welding J.,* **2**, 3–10. DOI: https://doi.org/10.37434/tpwj2022.02.01
12. Bobzin, K., Cook, D., Kowalsky, K. et al. (2007) Thermal spraying of cylinder bores with the PTWA internal coating system. In: *Proc. of the ASME Inter. Engine Combustion Engine Division Fall 2007 Technical Conf. ICEF07*, 1–8.
13. Sun, P., Fang, Z., Zhang, Y. et al. (2017) Review of the methods for the production of spherical Ti and Ti alloy powder. *JOM*, **69**, 1853–1860. DOI: https://doi.org/10.1007/s11837-017-2513-5
14. Korzhyk, V.M., Strogonov, D.V., Burlachenko, O.M. et al. (2023) Effectiveness of the process of plasma-arc spheroidization of current-conducting titanium wire. *Suchasna Elektrometal.,* **1**, 33–42.
15. Kaplan, M.A., Gorbenko, A.D., Ivannikov, A.Y. et al. (2022) Preparation and investigation of spherical powder made from corrosion-resistant 316L steel with the addition of 0.2 % and 0.5 % Ag. *Materials*, 7887(**15**), 13. DOI: https://doi.org/10.3390/ma15227887
16. Cao, M., Gitzhofer, F., Gravelle, D.V. et al. (1997) A torch nozzle design to improve plasma spraying techniques. In: Plasma Sources Science and Technology. *IOP Publ.*, 8. DOI: https://doi.org/10.1088/0963-0252/6/1/006
17. Kalayda, T.A., Kirsankin, A.A., Ivannikov, A.Y. et al. (2021) The plasma atomization process for the TiAlV powder production. *J. Phys.: Conf. Ser.*, **1942**, 012046. DOI: https://doi.org/10.1088/1742-6596/1942/1/012046

ORCID

V.M. Korzhyk: 0000-0001-9106-8593,
D.V., Strogonov: 0000-0003-4194-764X,
O.M. Burlachenko: 0000-0003-2277-4202,
O.V. Ganushchak: 0000-0003-4392-6682,
O.M. Voitenko: 0000-0003-4946-6517

CONFLICT OF INTEREST

The Authors declare no conflict of interest

CORRESPONDING AUTHOR

V.M. Korzhyk
E.O. Paton Electric Welding Institute of the NASU
11 Kazymyr Malevych Str., 03150, Kyiv, Ukraine.
E-mail: vnkorzhyk@gmail.com

SUGGESTED CITATION

V.M. Korzhyk, D.V., Strogonov, O.M. Burlachenko, O.V. Ganushchak, O.M. Voitenko (2023) New generation unit for plasma-arc deposition of coatings and atomisation of current-carrying wire materials. *The Paton Welding J.*, **10**, 35–42.

JOURNAL HOME PAGE

https://patonpublishinghouse.com/eng/journals/tpwj

Received: 20.06.2023
Accepted: 14.11.2023

DOI: https://doi.org/10.37434/tpwj2023.10.07

NUMERICAL-INSTRUMENTAL METHOD OF THERMOGRAPHIC CONTROL OF THE STATE OF LARGE-SIZED STRUCTURES AND CONSTRUCTIONS

O.S. Milenin, V.Yu. Glukhovskyi, O.A. Velykoivanenko, V.A. Lytvynenko

E.O. Paton Electric Welding Institute of the NASU
11 Kazymyr Malevych Str., 03150, Kyiv, Ukraine

ABSTRACT

A numerical-instrumental approach of thermographic control was developed to improve the efficiency of contactless control of the state of difficult-of-access parts of large-sized structures and constructions. It consists in integrated application of industrial thermal imaging instruments and computational methods of analysis of temperature fields in the studied structures. This allows improving the accuracy of determination of the geometrical features of the defects and reducing the labour consumption of operations of technical diagnostics of the state. Application of the developed approach was demonstrated on typical examples of contactless control of the technical state of industrial chimneys.

KEYWORDS: thermographic control, technical state, flaw detection, industrial chimneys, heat transfer

INTRODUCTION

Diagnostics of the technical state of large-sized structures, buildings and constructions of long-term operation is a mandatory stage of expert analysis of their state and the basis for planning measures of repair and restoration works. One of the main aspects of the study is to detect defects in structures that can affect the integrity and functionality of the corresponding structural components.

To analyse structures of a certain class (residential and non-residential buildings, chimneys, tanks, high-pressure vessels) while detecting geometric anomalies of different types, the methods of passive thermographic control (TC) proved to be efficient, which allow diagnosing the state of buildings in difficult-of-access places avoiding the use of the high-cost equipment and reducing production risks for staff [1, 2]. The essence of this method consists in the fact that the temperature difference inside the examined structure and outside is different, and it causes a certain heating of the outer surface. The actual distribution of surface temperature depends on many factors, in particular, on thermal resistance of a structure, heat conductivity of materials, as well as on the presence of operation defects, i.e. local thinning or cavities in the wall. This can be registered using contactless thermographic methods. The simplicity and availability of this approach caused its widespread use for the assessment of thermal characteristics of buildings, detection of zones of excessive heat losses, air leaks, absence or failure to thermal insulation, moisture sources, etc. [3, 4]. The contactless nature of TC allows it to be widely used to analyze the failure to metal materials, as well as to detect subsurface defects in polymers or composites [5, 6].

However, one of the fundamental disadvantages of this method of technical diagnostics is the low accuracy of quantitative assessment of sizes of detected defects, especially over the thickness of a structure. This means that in case of detection of certain anomalies, in order to prepare the reasonable expert opinion about their admissibility, additional measures are necessary to inspect the corresponding structural element, which, in some way, diminishes the benefits of TC. Therefore, the development of science-intensive approaches to the analysis of the results of measuring temperature fields in terms of quantitative interpretation is relevant.

THE AIM

of the work is the development of a numerical-instrumental method of TC of the state of large-sized structures and constructions on the basis of integrated use of thermal imaging instruments and computational approaches for thermal fields analysis.

RESEARCH PROCEDURE

The instrumental part of the proposed procedure consists in the thermographic measurement of natural (passive thermography) or induced (active thermography) fields on the surface of plane or cylindrical structures. The areas of surface or subsurface defects are characterized by change in the local temperature. In this case, the ratio of temperatures in the area of a defect and in the defect-free area of the structure depends, first of all, on the residual thickness of the wall and the type of a defect. To determine the type (surface, subsurface) and the actual size of discontinuity,

it is necessary to know the dependences of the local temperature on the outer surface of the structure in the area of a defect on the thermophysical properties of the material and the features of the temperature effect. Such dependencies were obtained on the basis of a numerical computation of the temperature field, taking into account the geometric and physical features of the structural state. Validation of mathematical models and tools for their computer implementation was conducted on the basis of appropriate laboratory studies of model structural elements.

Thus, the computation of an uneven temperature field was based on the finite-differential solution of the non-stationary heat conductivity equation [7, 8]:

● in the Cartesian coordinate system (x, y, z) — to describe the heat transfer processes in the plates:

$$\begin{aligned} C\rho(x,y,z,T)\cdot\frac{\partial T(x,y,z,t)}{\partial t} = \\ =\frac{\partial}{\partial x}\left[\lambda(x,y,z)\cdot\frac{\partial T(x,y,z,t)}{\partial x}\right]+ \\ +\frac{\partial}{\partial y}\left[\lambda(x,y,z)\cdot\frac{\partial T(x,y,z,t)}{\partial y}\right]+ \\ +\frac{\partial}{\partial z}\left[\lambda(x,y,z)\cdot\frac{\partial T(x,y,z,t)}{\partial z}\right]. \end{aligned} \quad (1)$$

● in the cylindrical coordinate system (r, β, z) — for the cylindrical structures:

$$\begin{aligned} C\rho(r,\beta,z,T)\cdot\frac{\partial T(r,\beta,z,t)}{\partial t} = \\ =\frac{1}{r}\cdot\frac{\partial}{\partial r}\left[r\cdot\lambda(r,\beta,z)\cdot\frac{\partial T(r,\beta,z,t)}{\partial r}\right]+ \\ +\frac{1}{r^2}\cdot\frac{\partial}{\partial \beta}\left[\lambda(r,\beta,z)\cdot\frac{\partial T(r,\beta,z,t)}{\partial \beta}\right]+ \\ +\frac{\partial}{\partial z}\left[\lambda(r,\beta,z)\cdot\frac{\partial T(r,\beta,z,t)}{\partial z}\right]. \end{aligned} \quad (2)$$

where T is the temperature, °C; λ is the heat conductivity, J/(m³·s·°C); $C\rho$ is the volumetric heat capacity, J/(m³·s·°C).

When setting the problem (1) or (2), the boundary conditions of the second order were used according to the total action of characteristic sources and heat sinks. As the main dissipative processes, convective (in accordance with the Newton–Richman's law) and radiation (according to the Stefan–Boltzman law) mechanisms were considered. The process of heating from one of the surfaces of the examined object was described by the appropriate heat flow. The numerical solution of the heat conductivity equation allowed determining both the stationary temperature distribution as well as the kinetics of temperature field development, which was important during the laboratory validation of the numerical approach.

Table 1. Dependence of thermophysical properties of St3kp (rimmed) steel on temperature [9]

T, °C	Heat conductivity, W/(m·°C)	Heat capacity, J/(kg·°C)
100	55	482
200	54	498
300	50	514
400	45	533
500	39	555
600	34	584
700	30	626

LABORATORY TESTS

The developed approach was validated by comparing the temperature fields measured by a thermal imager (TESTO 876 with resolution capacity of 320×240 pixels) on the test specimens with model surface defects, with the results of numerical computations. As the test specimens, plates of 300×200×10 and 260×125×10 mm of st3 kp (rimmed) steel were used, thermophysical properties of the material, depending on the temperature are given in Table 1. As the model defects, thinning of 160 mm length, 50 mm width at 2 and 6 mm depths and horizontal subsurface delamination (1×61×66 mm at a depth of 8 mm) (Figure 1) were considered. In the framework of laboratory tests, a method of double active thermography was used, for which on one side, the specimens were heated by an infrared source, whose power varied from 1.05 to 0.45 kW, and on the other, temperature fields were measured.

The heating of the mentioned laboratory specimens was carried out at different time intervals to provide a stationary temperature field. Thus, the heating of the plate with thinning (Figure 1, *a*) proceeded during 905 s, thermograms of temperature fields on the specimen surface at different stages (5 and 65 s) are shown in Figure 2. As is seen from the measurement results, the areas of defects of thinning are characterized by a local growth in temperature compared to the periphery from 3 to 22 °C, depending on the depth of defect and the time of heating. In contrast to the defect of thinning of the plate in case of available delamination on the surface of a laboratory specimen, a drop in a local temperature as a result of an increase in thermal resistance of the plate is observed (Figure 3). For the case that was considered in the framework of the laboratory tests (Figure 1, *b*) and heating during 47 s, the amount of a local drop in the surface temperature was about 2 °C. The comparison of experimentally measured temperature distributions with the results of computations (Figure 4) show an error of not more than 15 % both at the stage of heating as well as in a stationary mode. Such a level of accuracy is sufficient

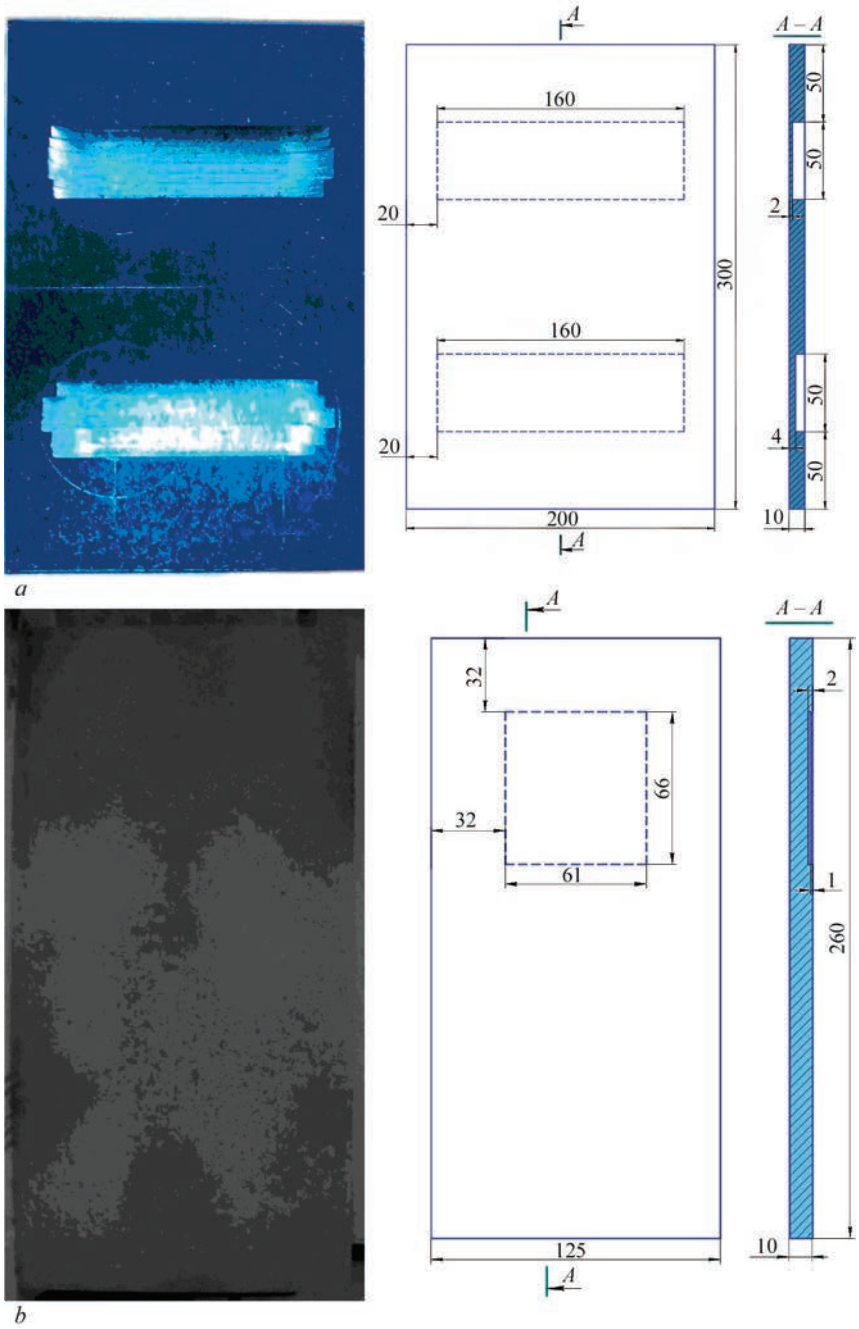

Figure 1. Appearance and schemes of plates with model defects used for laboratory tests: *a* — plate with thinning; *b* — plate with delamination

to solve engineering problems of technical diagnostics and increase the accuracy of quantitative analysis of the corresponding thermograms.

RESULTS AND DISCUSSION

The developed approach was used to increase the efficiency of diagnostics of the technical state of typical industrial chimneys on the example of structures of a reinforced concrete four-layer industrial chimney for the PTV-100 boiler units (height is 120 m, mouth diameter is 4.8 m, wall thickness of the examined area of the chimney is 0.55 m, thickness of the reinforced concrete layer is 0.120 m, brick clamping layer is 0.120 m, heat insulating layer is 0.05 m and brick lining layer is 0.120 m). Thermophysical characteristics of the layers materials are given in Table 2. Based on the results of the numerical computation, the dependences of the maximum temperature in the center of a defect of the local wall thinning from its depth and inner temperature in the chimney at different temperature of flue gases in the chimney T_{out} (Figure 5) was obtained. As is seen from this data, during failure of the inner layer of the brick lining, a rapid growth of temperature on the outer surface of the chimney begins only with the degradation of the next layer, namely thermal insulation, which imposes some restrictions on the use of TC of the technical state of such heterogeneous objects.

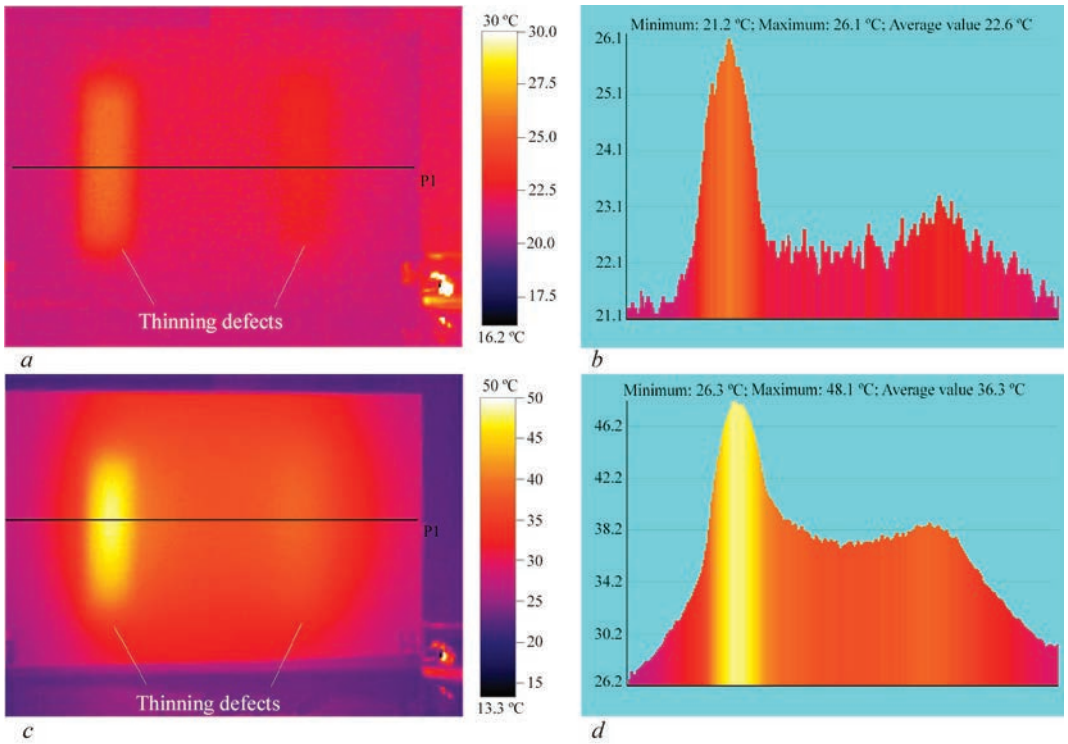

Figure 2. Thermograms of temperature fields on the surface of a plane laboratory specimen with model defects of thinning (*a*, *c*) and temperature distributions along the line P1 (*b*, *d*) at different intervals of time after the start of heating: *a*, *b* — 5 s; *c*, *d* — 65 s

With regard to subsurface delamination defects, Figure 6 shows the calculated dependences of the local temperature on radial size of a volumetric defect (size of cavity opening as a result of material degradation) located in the central insulating layer of the chimney and the temperature of flue gases. As is seen from this data, the recommended TC method is sufficiently sensitive to detect such kind of inner defects which are difficult to detect by other means of non-destructive testing: temperature difference on the surface depending on the size of a defect reaches 0.2 °C, which can be detected, tak-

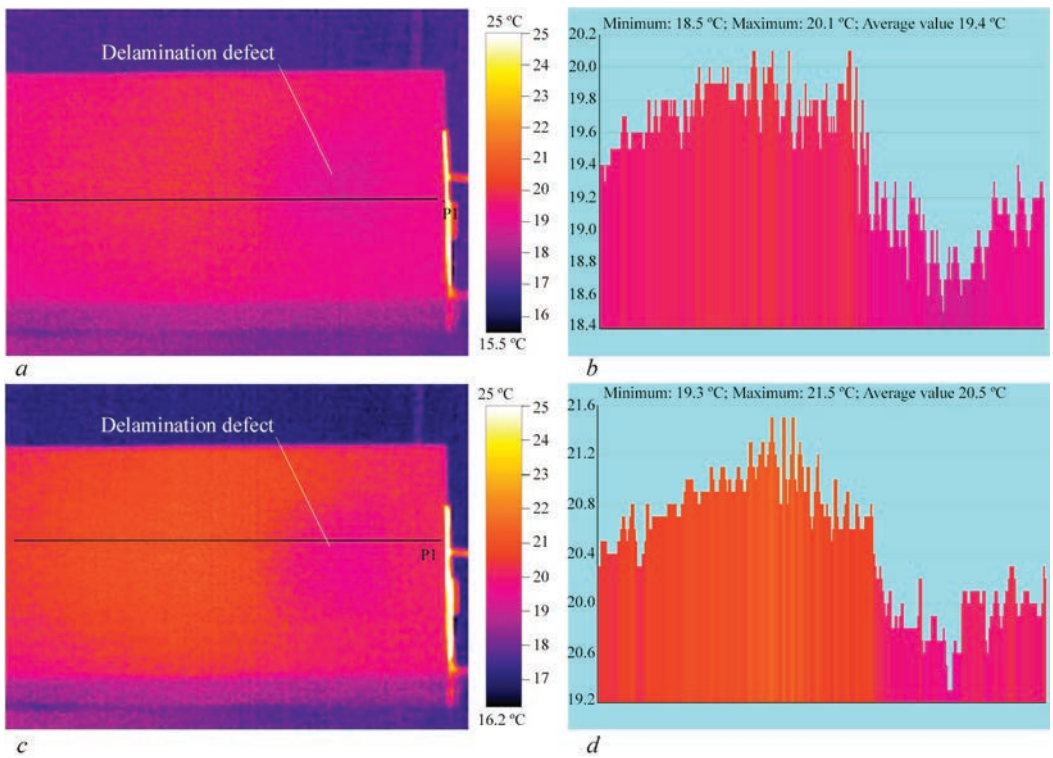

Figure 3. Thermograms of temperature fields on the surface of a plane laboratory specimen with a model delamination defect (*a*, *c*) and temperature distributions along the line P1 (*b*, *d*) at different time intervals after the start of heating: *a*, *b* — 18 s; *c*, *d* — 47 s

Table 2. Thermophysical properties of materials of different layers of industrial chimney for the PTV-100 boiler units in a dry state at atmospheric pressure and temperature of 20–50 °C [10]

Layer description	Material	Heat conductivity, W/(m·°C)	Heat capacity, J/(kg·°C)
Lining	Red solid brick	0.74	860
Thermal insulation	Mineral wool	0.041	920
Clamping	Red solid brick	0.74	860
Ferroconcrete trunk	Reinforced concrete	1.70	840

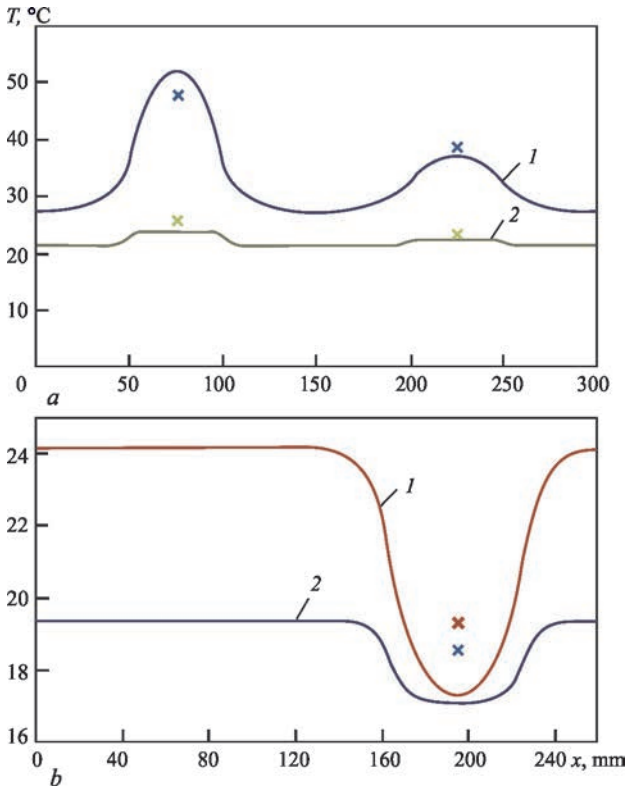

Figure 4. Computational temperature distributions on the surface of a laboratory specimen with thinning (*a*) (*1* — τ = 65 s, *2* — τ = 5 s) and delamination (*b*) (*1* — τ = 47 °C, *2* — τ = 18 °C) through different time intervals of heating (lines) and corresponding values of thermographic measurements (×)

ing into account the accuracy of the instrument at a level of 0.1 °C.

The proposed calculated dependencies allow analyzing the appropriate thermograms more accurately, evaluating the temperature inside the chimney at a certain height (the corresponding dependencies converge to the specific surface temperatures of the defect-free surface area at a size of a defect equal to zero), determining the type and sizes of defects in the process of TC.

CONCLUSIONS

A numerical-instrumental method of thermographic analysis of the technical state of large-sized structures and constructions was developed in order to improve the accuracy of determining the sizes of operational defects. For this purpose, the methods of numerical modelling of the uneven temperature field on the surface of plane or cylindrical testing objects with instru-

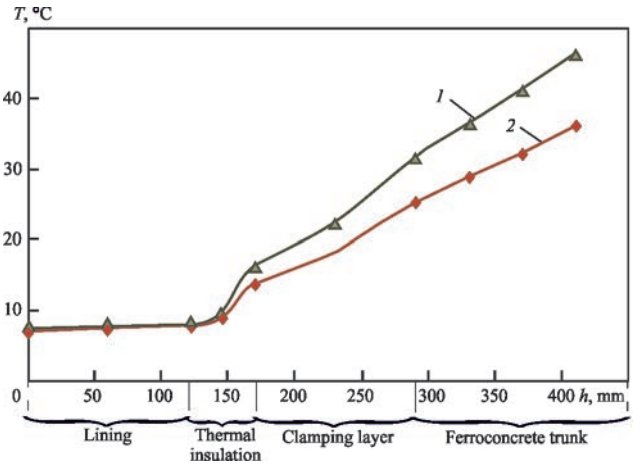

Figure 5. Calculated dependences of the local temperature maximum on the depth of thinning of the industrial four-layer chimney with a diameter of 5870 mm at different temperatures of flue gases: T_{out}: *1* — 130; *2* — 100 °C

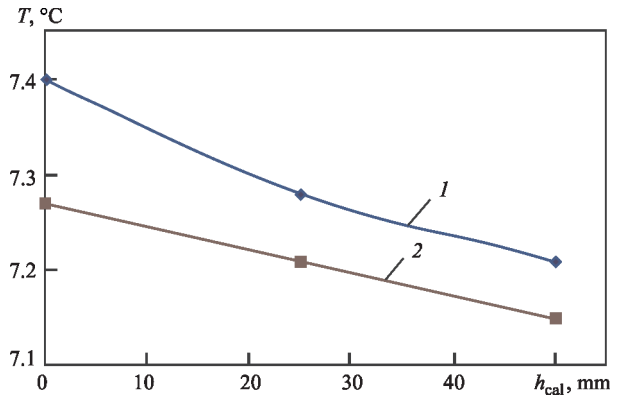

Figure 6. Calculated dependences of the local temperature minimum on the size of degradation (delamination) of the insulating layer of the industrial chimney with a diameter of 5870 mm at different temperatures of flue gases T_{out}: *1* — 130; *2* — 100 °C

mental approaches of the thermographic analysis of infrared radiation were combined.

To validate the developed method, laboratory tests on the steel plates with such model defects as local thinning and inner delamination were performed. According to the results of computations and thermographic measurement of the surface temperature of the defective specimen, an error of the developed approach of not higher than 15 % was shown.

On the example of the structure of a ferroconcrete four-layer industrial chimney for the PTV-100 boiler units of 120 m height and with the mouth diameter of 4.8 m based on the numerical computation results, the

dependencies of the maximum temperature in the center of a defect of the local wall thinning on its depth as well as the local temperature on the radial size of a volumetric delamination defect located in the central cross-section of the chimney wall were obtained. The proposed calculated dependencies based on the analysis of the corresponding thermograms allow evaluating the temperature inside the chimney at a certain height, determining the type and sizes of defects with a high accuracy.

REFERENCES

1. Fox, M., Coley, D., Goodhew, S., P. de Wilde (2014) Thermography methodologies for detecting energy related building defects. *Renewable and Sustainable Energy Reviews*, **40**, 296–310. DOI: https://doi.org/10.1016/j.rser.2014.07.188
2. DSTU B EN 13187:2011: *Thermal performance of buildings — Qualitative detection of thermal irregularities in building envelopes – Infrared method*.
3. Kylili, A., Fokaides, P.A., Christou, P., Kalogirou, S.A. (2014) Infrared thermography (IRT) applications for building diagnostics: A review. *Applied Energy*, **134**, 531–549. DOI: https://doi.org/10.1016/j.apenergy2014.08.005
4. Miguel, M., Chong, A., Biljecki, F., Miller, C. (2022) Infrared thermography in the built environment: A multi-scale review. *Renewable and Sustainable Energy Reviews*, **165**, 112540. DOI: https://doi.org/10.1016/j.rser.2022.112540
5. Wu, Z., Qin, S., Zhang, P., Pan, Z. (2023) Damage evolution in braided composite tubes under axial compression studied by combining infrared thermography and X-ray computed tomography. *Composite Structures*, **307**, 116634. DOI: https://doi.org/10.1016/j.compstruct.2022.116634
6. Xie, H., Fang, H., Li, X. et al. (2021) Low-velocity impact damage detection and characterization in composite sandwich panels using infrared thermography. *Composite Structures*, **269**, 114008. DOI: https://doi.org/10.1016/j.compstruct.2021.114008
7. Karkhin, V.A. (2019) *Thermal processes in welding*. Singapore, Springer Singapore.
8. Akhonin, S.V., Milenin, A.S., Pikulin, A.N. (2005) Modeling of processes of evaporation of alloying elements in EBSM of cylindrical ingots produced from Ti-base alloys. *Advances in Electrometallurgy*, **1**, 21–25.
9. (1991) *Physical quantities*: Handbook. Eds by I.S. Grigoriev, E.Z. Mejlikhov. Moscow, Energoatomizdat [in Russian].
10. https://eco-obogrev.com/ua/a233242-spravka-plotnost-teploprovodnost.html

ORCID

O.S. Milenin: 0000-0002-9465-7710,
V.Yu. Glukhovskyi: 0000-0002-1969-495X,
V.A. Lytvynenko: 0000-0003-3680-2198

CONFLICT OF INTEREST

The Authors declare no conflict of interest

CORRESPONDING AUTHOR

O.S. Milenin
E.O. Paton Electric Welding Institute of the NASU
11 Kazymyr Malevych Str., 03150, Kyiv, Ukraine.
E-mail: asmilenin@ukr.net

SUGGESTED CITATION

O.S. Milenin, V.Yu. Glukhovskyi, O.A. Velykoivanenko, V.A. Lytvynenko (2023) Numerical-instrumental method of thermographic control of the state of large-sized structures and constructions. *The Paton Welding J.*, **10**, 43–48.

JOURNAL HOME PAGE

https://patonpublishinghouse.com/eng/journals/tpwj

Received: 03.04.2023
Accepted: 14.11.2023